

CHARACTERIZATION OF A LASER
WELDED DP780 STEEL

MICROSTRUCTURE AND MECHANICAL PROPERTIES
OF THE FUSION AND HEAT-AFFECTED ZONES OF A
LASER WELDED DP780 STEEL

By: HEATHER SMITH, B. Eng

A Thesis

Submitted to the School of Graduate Studies

in Partial Fulfilment of the Requirements

for the Degree

Master of Applied Science

McMaster University

© Copyright by Heather Smith, February, 2015

Master of Applied Science (2015)
(Materials Science & Engineering)

McMaster University
Hamilton, Ontario, Canada

TITLE: Microstructure and Mechanical Properties of the
 Fusion and Heat-Affected Zones of a Laser Welded
 DP780 Steel

AUTHOR: Heather Smith, B. Eng. (McMaster University)

SUPERVISOR: Dr. J.R. McDermid

NUMBER OF PAGES: xv, 102

Abstract

Bead-on-plate laser welds were made on an industrially produced DP780 steel to determine the effect of normalized welding heat input on the microstructure and mechanical properties within the weld fusion zone (FZ) and heat affected zone (HAZ) with reference to the base material (BM) mechanical properties. Normalized welding heat input was calculated using an established model from the literature utilizing measurements from the weld cross-section microstructures along with known materials properties. Microhardness profiles and optical microscopy were employed to evaluate materials properties and microstructural changes across the various microstructural zones of each weld. The mechanical properties of the welds were evaluated globally through standard ASTM tensile specimens as well as through a series of specialized mechanical testing sample geometries which examined the properties of individual microstructural zones. These specialized sample geometries included non-standard uniaxial and plain strain tension where effective stress and effective strains were used to compare the mechanical properties across samples.

It was determined that there was a good correlation between ASTM standard samples and the specialized sample geometries employed in this study and that the UTS and YS values obtained in both cases were comparable. Sigmoidal decay behaviour was observed in the UTS and YS with increasing heat

input for both the FZ and HAZ of all welds. It was found that welds with heat inputs greater than 60 J/mm^2 had both a UTS and YS which were significantly depressed in the FZ and HAZ when compared to the base material values. Conversely, welds with heat inputs below 36.3 J/mm^2 were found to have a UTS and YS in both the FZ and HAZ microstructural zones which were above the values determined for the BM. When global weld properties were tested, it was found that welds with a heat input greater than 60.0 J/mm^2 failed within the HAZ while welds with heat inputs below 36.3 J/mm^2 failed within the BM. It has been shown that there is a significant correlation between the heat inputs of laser welded DP steels and both the mechanical properties and microstructural features of the various microstructural zones as well as the location of failure during weld tensile testing. It has also been demonstrated that the mechanical properties of weld microstructural zones can be qualitatively evaluated using specialized tensile testing geometries.

Acknowledgments

I would like to start by thanking my supervisor Dr. Joe McDermid for his continuous guidance and support throughout this research project. I would like to thank Mike Bruhis for training me on the ARAMIS system and mechanical testing as well as his help with designing and acquiring the specialized testing geometry samples used in this project. As well Connie Barrie is thanked for her help with equipment training, metallography and general guidance and support. I would also like to thank Dr. Joey Kish, for providing positive feedback throughout the research project.

Thanks to my Centre for Automotive Materials and Corrosion (CAMC) group members for listening to countless presentation of this work and providing feedback. Special thanks to Dr. Elliot Biro at ArcelorMittal for his feedback, and many conversations about this work. The members of the Centre for Advanced Materials and Joining (CAMJ) and Dr. Norman Zhou at the University of Waterloo are thanked for allowing me to share my work and receive feedback at their group meetings, in particular, thanks to Daniel Westerbaan and Dulal Saha for the welding of my samples.

The staff at the Canadian Centre for Electron Microscopy (CCEM), especially Glynis de Silveira and Chris Butcher are acknowledged for their help in

both electron and optical microscopy. I would also like to thank Doug Culley and Ed McCaffery for their help and support in the MSE labs.

I would like to acknowledge the funding of Natural Science and Engineering Research Council (NSERC), US Steel Canada, and the Steel Research Centre (SRC) as well as ArcelorMittal for the provision of materials.

Last but not least, I would like to thank my family and friends for always loving, supporting and encouraging me.

Table of Contents

Abstract	iii
Acknowledgments.....	v
Table of Contents	vii
List of Tables	x
List of Figures	xi
List of Abbreviations and Symbols.....	xiv
CHAPTER 1 Introduction	1
1.1 Background and Motivation	1
1.2 Thesis Outline.....	2
CHAPTER 2 Literature Review	5
2.1 Dual Phase Steels	5
2.1.1 Definition of DP Steels	5
2.1.2 Mechanical Properties	6
2.2 Laser Welding.....	9
2.2.1 Heat Input.....	10
2.3 Martensite.....	12
2.3.1 Structure and Formation	12
2.3.2 Martensite Tempering	14
2.4 Bainite	18
2.4.1 Structure	18
2.4.2 Formation.....	19
2.5 Strain Measurement by Digital Image Correlation (DIC)	21
2.6 Effect of Welding on DP Steels – Fusion Zone	22
2.7 Effect of Welding on DP Steels - HAZ	23
2.7.1 Softening Kinetics.....	24
2.7.2 Bulk Mechanical Properties.....	30
CHAPTER 3 Research Objectives	33

CHAPTER 4 Experimental Methods.....	35
4.1 Materials.....	35
4.2 Welding Conditions	36
4.3 Weldment Characterization	37
4.3.1 Microscopy	37
4.3.2 Heat Input.....	37
4.3.3 Microhardness Profiles.....	38
4.4 Mechanical Testing.....	39
4.4.1 Effective Stress- Effective Strain Calculation	42
CHAPTER 5 Results	45
5.1 Microhardness Profiles.....	45
5.1.1 Diode Welds.....	45
5.1.2 Fibre Welds.....	49
5.2 Weldment Microstructures	54
5.2.1 Diode Welds.....	54
5.2.2 Fibre Welds.....	58
5.3 Mechanical Testing.....	60
5.3.1 Base Material	60
5.3.2 Across Weld Tensile Testing.....	62
5.3.3 Specialized Geometries - Diode Welds.....	65
5.3.4 Specialized Geometries - Fibre Welds.....	70
5.4 Results Summary.....	72
CHAPTER 6 Discussion	75
6.1 Heat Input Normalization.....	75
6.2 Cooling Rates and the Fusion Zone.....	78
6.3 Thermal Activation of HAZ Martensite Tempering.....	81
6.4 Weld Failure Localization.....	85
6.5 Summary	86
CHAPTER 7 Conclusions and Future Work	89
7.1 Conclusions.....	89
7.2 Future Work.....	90

References	91
APPENDIX A Plane Strain Criteria.....	97
APPENDIX B Microstructure	98
APPENDIX C Strain Maps	99
APPENDIX D Heat Input Calculations.....	101

List of Tables

Table 4.1: Chemical Composition of DP780 Steel.....	35
Table 4.2: Laser Parameters for Welding of DP780.....	36
Table 5.1: Sample nomenclature.	45
Table 5.2: Summary of diode weld hardness measurements.....	46
Table 5.3: Summary of fibre weld hardness measurements.	50
Table 5.4: Summary of fibre weld mechanical properties.....	71
Table 6.1: Heat input and time constants for all welding conditions.	75
Table A.1: Plane strain criteria for mechanical testing samples.....	97
Table D.1: Materials properties used in Equation (1) and(2).	101
Table D.2: Average HAZ and FZ radii measured from weld cross-sections.	102

List of Figures

Figure 2.1: Computed equilibrium phase diagram for a Fe-1 wt% Mn-C alloy [3].	6
Figure 2.2: Total elongation versus tensile strength bubble plot for various steels in use in the automotive industry [6].	7
Figure 2.3: Tensile strength and flow stress at $\epsilon=0.002$ (yield strength) plotted against fraction martensite for several DP steels [3].	8
Figure 2.4: Tensile strength versus fraction martensite for a 1.5 wt% Mn DP steel [1].	8
Figure 2.5: Laser welding schematic for a butt weld [8].	9
Figure 2.6 Weld cross section showing the measured values for the heat input calculation.[13]	12
Figure 2.7: Example microstructures of (a) lath martensite in a 0.02% C and 2% Mn steel and (b) plate martensite in a 1.2% C steel [17].	13
Figure 2.8 Temperature profiles of the isothermal and non-isothermal tempering used in [20].	15
Figure 2.9: Schematic of the differences between isothermal and non-isothermal tempering [20].	16
Figure 2.10: Schematic illustrations of various bainite morphologies defined by Reynolds et al. [24]. (a) Nodular bainite, (b) Columnar bainite, (c) Upper bainite, (d) Lower bainite, (e) Grain boundary allotromorphic bainite, (f) Inverse bainite.	19
Figure 2.11: DIC system setup [36].	21
Figure 2.12: Schematic illustration of a reference square subset before deformation and a target (or deformed) subset after deformation [36].	22
Figure 2.13: CCT curve for DP780 steel with cooling curves superimposed[37].	23
Figure 2.14: Comparison of HAZ softening kinetics, phi versus time constant of all experimental steels examined by Biro et al. [4].	25
Figure 2.15: DP780 data from Biro et al. [5] (a) hardness plotted versus tempering time and (b) transformed data to phi (fraction of completed softening) versus tempering time.	26
Figure 2.16: Validation of the softening model (a) comparison of measured hardness and the hardness predicted by the JMAK model and (b) comparison of the measure HAZ softening and the HAZ softening predicted by the JMAK model [5].	28
Figure 2.17: Logarithmic transformation of M220 softening data from [38].	29
Figure 2.18: Representative stress-strain curves for DP980, BM, diode laser welds, single pass fibre laser welds, and multiple fibre laser welds from Xu et al. [41].	31
Figure 2.19: Comparison of LDH of parent material with tailor welded blanks (TWB) of different material combinations from Panda et al. [46].	32

Figure 4.1: Base material microstructure; dark regions represent martensite while the light regions are the ferrite matrix.....	36
Figure 4.2: Cross section of a weld showing the boundaries for heat input calculations.	38
Figure 4.3: Geometry of miniature tensile mechanical testing sample (all dimensions in mm).....	40
Figure 4.4: Geometry of a plane strain sample for mechanical testing of diode weld microstructural zones (all dimensions in mm).	41
Figure 4.5: Geometry of plane strain sample for mechanical testing of fibre weld microstructural zones (all dimensions in mm).....	42
Figure 5.1: Typical microhardness profile of a 4 kW (D) 0.8 weld, where BM is the base material, HAZ is the heat-affected zone and FZ is the fusion zone.....	46
Figure 5.2: Typical microhardness profile of a 4 kW (D) 1.0 weld.....	47
Figure 5.3: Typical microhardness profile of a 4 kW (D) 1.2 weld.....	48
Figure 5.4: Composite plot of microhardness profiles for high heat input diode welds.....	49
Figure 5.5: Typical hardness profile for a 4kW (F) 2 weld.	50
Figure 5.6: Typical hardness profile of a 4kW (F) 4 weld.....	51
Figure 5.7: Typical microhardness profile of a 6 kW (F) 2 weld.....	52
Figure 5.8: Typical microhardness profile of a 6 kW (F) 4 weld.....	53
Figure 5.9: Composite plot of microhardness profiles for low heat input fibre welds.....	53
Figure 5.10: 4 kW, 0.8 m/min diode weld HAZ microstructure.....	55
Figure 5.11: FZ microstructure of (a) 4kW (D) 0.8 weld (b) 4kW (D) 1.0 weld and (c) 4kW (D) 1.2 weld.....	56
Figure 5.12: CCT curve for DP780 steel with cooling curves superimposed [37]..	57
Figure 5.13: HAZ microstructures of (a) 4 kW (F) 2 weld (b) 4 kW (F) 4 weld (c) 6 kW (F) 2 weld and (d) 6 kW (F) 4 weld.....	58
Figure 5.14: FZ microstructures of (a) 4 kW (F) 2 weld (b) 4 kW (F) 4 weld (c) 6kW (F) 2 weld and (d) 6kW (F) 4 weld.	59
Figure 5.15: Base material effective stress - effective strain curves as a function of sample geometry and strain path.....	61
Figure 5.16: Yield strength and UTS measured from all BM testing geometries in both the rolling (RD) and transverse (TD) directions.	62
Figure 5.17: Strain map and strain versus section length plot for a 4kW (D) 0.8 weld.	63
Figure 5.18: Strain map and strain versus section length plot for a 4kW (F) 2 weld.	64
Figure 5.19: Strain map and strain versus section length plot for a 6kW (F) 4 weld.	65

Figure 5.20: Effective stress - effective strain curves for a 4kW (D) 0.8 weld.	66
Figure 5.21: Effective stress - effective strain curves for a 4kW (D) 1.0 weld.	67
Figure 5.22: Effective stress - effective strain curves for a 4kW (D) 1.2 weld.	68
Figure 5.23: Comparison of mechanical properties for the diode weld fusion zones versus the base material (BM).	69
Figure 5.24: Comparison of mechanical properties for the diode weld heat-affected zones versus the BM.	70
Figure 5.25: Effective stress – effective strain curves for a 4 kW (F) 2 and a 4 kW (F) 4 weld.	71
Figure 5.26: Effective stress - effective strain curves for a 6 kW (F) 2 and a 6 kW (F) 4 weld.	72
Figure 6.1: Delta hardness (difference in hardness from the BM to the minimum HAZ value) versus heat input.	77
Figure 6.2: HAZ minimum hardness versus time constant for present study and data from Biro et al. [4].	77
Figure 6.3: HAZ softening versus time constant for present study and data from Biro et al. [4].	78
Figure 6.4: Stress versus heat input for the diode weld fusion zones.	79
Figure 6.5: Stress versus heat input for fibre weld fusion zones.	79
Figure 6.6: Stress versus heat input for all experimental weld fusion zones.	81
Figure 6.7: Stress versus heat input for the diode weld heat-affected zones.	82
Figure 6.8: Stress versus heat input for fibre weld heat-affected zones.	82
Figure 6.9: Stress versus heat input for all experimental weld heat-affected zones.	84
Figure 6.10: Yield strength versus heat input for all HAZ showing the failure location of across weld samples.	86
Figure B.1: 4 kW, 1.0 m/min diode weld HAZ microstructure.	98
Figure B.2: 4 kW, 1.2 m/min diode weld HAZ microstructure.	98
Figure C.1: Strain map and strain versus section length plot for 1.0 m/min diode weld.	99
Figure C.2: Strain map and strain versus section length plot for a 4kW (F) 4 weld.	99
Figure C.3: Strain map and strain versus section length plot for 1.2 m/min diode weld.	100
Figure D.1: Weld cross-section, showing the weld centreline, fusion zone boundary and AC1 isotherm.	101

List of Abbreviations and Symbols

a	Thermal diffusivity ($\lambda/\rho c$)
AHSS	Advanced High Strength Steel
BCC	Body Centred Cubic
BCT	Body Centred Tetragonal
BM	Base Material
c	Specific heat capacity (J/kg/K)
CCT	Continuous Cooling and Transformation
d	Sheet thickness (mm)
DIC	Digital Image Correlation
DP	Dual Phase
FZ	Fusion Zone
HAZ	Heat-Affected Zone
JMAK	Johnson-Mehl-Avrami-Kolmogorov
LDH	Limiting Dome Height
N	Number of samples
Q_{net}	Net laser power (W)
r_{Ac1}	Ac1 isotherm position (m)
RD	Rolling Direction
r_{m}	Melting isotherm position (m)
s	Standard deviation
t	Time (s)
T_0	Ambient temperature (K)
T_{Ac1}	Ac1 temperature (K)
TEM	Transmission Electron Microscopy

T_m	Melting temperature (K)
$T_{N-1,95\%}$	Value of student t-distribution
TD	Transverse Direction
TTT	Time Temperature Transformation
UTS	Ultimate Tensile Strength
v	Welding speed (mm/s)
\bar{x}	Sample mean
YS	Yield Strength
ϵ_{eff}	Effective strain
ϵ_{eng}	Engineering strain
ϵ_{true}	True Strain
λ	Thermal conductivity (W/m/K)
μ	True value of measurement
ρ	Density (kg/m ³)
σ_{eff}	Effective stress
σ_{eng}	Engineering stress
σ_{true}	True stress
τ	Time constant (s)

CHAPTER 1 **Introduction**

1.1 Background and Motivation

The ongoing need to increase vehicle fuel efficiency, driven by both legislation and consumer demand, has led to investigating means to decrease the weight of vehicles while maintaining or improving safety. One way of accomplishing this is through the use of advanced high strength steels (AHSS). Dual phase (DP) steels are currently the most widely employed AHSS by automakers. DP steels exhibit an excellent strength/ductility balance and high work hardening rate as a result of a composite microstructure which includes ferrite, martensite and (sometimes) bainite. In order to employ any material in industry, it is important to consider the welding of said material and how its properties are affected by joining. A popular joining method for dual phase steels in the automotive industry is laser welding; however, due to the thermal instability of martensite, the microstructure and, therefore, the mechanical properties of the material when welded are deleteriously affected.

One of the main ways that the microstructure of dual phase steels is negatively impacted during welding is through softening of the heat affected zone, which results in lower mechanical properties and an unpredictable failure location for the welds. This occurs through the tempering of the martensite phase within the dual phase microstructure. In order to properly understand the effects on the

microstructure and in turn the mechanical properties it is important to study the underlying mechanisms to the softening behavior, determine actual normalized heat input to welds, study the decomposition products and finally characterize the kinetics of the softening behavior relative to the changes in the mechanical properties of each microstructural zone.

1.2 Thesis Outline

Chapter 2 of this thesis will be a survey of the literature, as it pertains to the present study. The fundamentals of DP steels, martensite and bainite will be discussed, including production routes and mechanisms of both bainite and martensite formation. Martensite tempering will also be discussed in the context of both as-quenched, fully hard martensite as well as within a DP steel. The fundamentals of laser welding including method of calculating heat input used in this work are also reviewed. The applications of digital image correlation (DIC) to the measurement of strain will be examined. Finally, the current literature on the effects of laser welding on the microstructure of both the fusion and heat-affected zones of DP steels will be analyzed including the current gaps in knowledge. Chapter 3 outlines the research objectives of the present study. In Chapter 4 an overview of the experimental methods employed in this study will be presented. The techniques used included optical microscopy, microhardness profiling as well as a variety of mechanical testing geometries. The results of the characterization and mechanical testing experiments are summarized in Chapter 5

and discussion of these results and how they fit within the context of the literature are presented in Chapter 6. Finally the major conclusions drawn from the results of this study along with the suggested future work are presented in Chapter 7.

CHAPTER 2 Literature Review

2.1 Dual Phase Steels

2.1.1 Definition of DP Steels

Dual phase (DP) steels are amongst the class of advanced high strength steels (AHSS) which are being used in significant quantities in the automotive industry for the light weighting of vehicles [1]. DP steels consist of a ferrite matrix with varying volume fractions of martensite, lower bainite or bainitic ferrite and retained austenite as second phases. Contrary to what the name would suggest, DP steels often consist of more than two phases [1], [2]. The steel examined in the present work, however, consists of a ferritic matrix with a second phase of martensite.

The dual phase microstructure is generally obtained through thermo-mechanical treatments. Continuous annealing, batch annealing and hot rolling processes can be used to obtain the DP microstructure [2]. For example hot and cold rolling can be used on as-cast structures followed by annealing to obtain the desired ferrite/pearlite grain size. Finally, the alloy can be heat treated at a temperature in the intercritical $\alpha + \gamma$ phase field (shaded region of Figure 2.1) for this specific chemistry, or just above the AC3 temperature for approximately 1-2 minutes followed by rapid cooling to obtain a mixed ferrite/martensite

microstructure [2], [3]. The specific time and temperature selected will control the amount of martensite found in the final microstructure of the alloy.

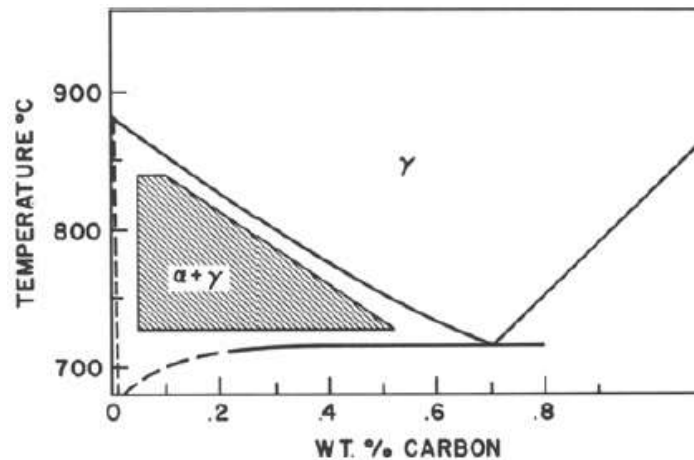


Figure 2.1: Computed equilibrium phase diagram for a Fe-1 wt% Mn-C alloy [3].

The current conventional industrial route for producing dual phase steels involves casting, hot rolling and pickling followed by cold rolling. Subsequently the steels are intercritically annealed; per the shaded area in Figure 2.1, and rapidly cooled to obtain the desired volume fraction of the martensite phase. Some steels are also continuously galvanized in order to coat them with zinc for corrosion protection, following a thermal cycle similar to that described above to obtain the desired microstructure. [4], [5].

2.1.2 Mechanical Properties

In Figure 2.2 below, the mechanical properties of several types of advanced high strength steels (AHSS) are compared to low strength steels as well as other

high strength steels [6]. Improving the tensile strength of materials while maintaining or improving the total elongation is very important for automotive applications as these materials need to be strong in structural components but also need to be able to absorb energy to maintain crashworthiness [6].

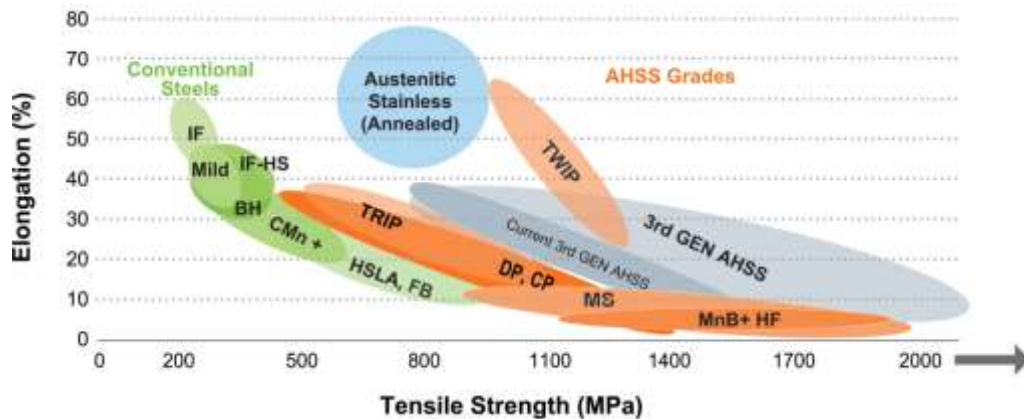


Figure 2.2: Total elongation versus tensile strength bubble plot for various steels in use in the automotive industry [6].

The excellent mechanical properties of DP steels can be attributed to the mixing of a ductile ferrite phase with the stronger more brittle martensite phase to achieve properties taking advantage of the best of both phases [1], [3] The mechanical properties of DP steels have been shown to be dependent on both the grain size of the ferrite and the volume fraction of martensite within the microstructure, with the latter roughly obeying a rule of mixtures formalism [1], [3], [7]. It has been reported that the composition and hardness of the martensite phase within the microstructure does not significantly affect the overall mechanical properties of the material [3]. The relationship of yield strength (YS) and ultimate tensile strength (UTS) with martensite fraction for several DP steels

is seen in Figure 2.3 and UTS versus martensite fraction for a 1.5 % Mn DP steel is seen in Figure 2.4.

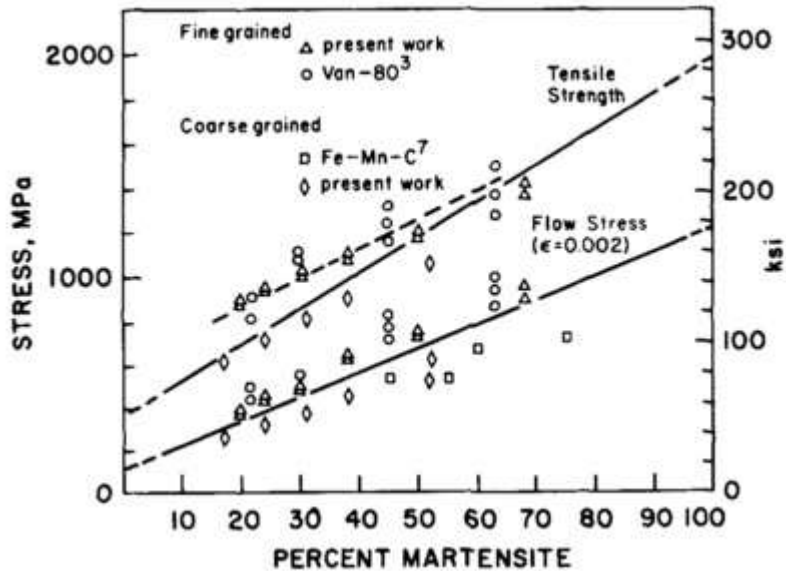


Figure 2.3: Tensile strength and flow stress at $\epsilon=0.002$ (yield strength) plotted against fraction martensite for several DP steels [3].

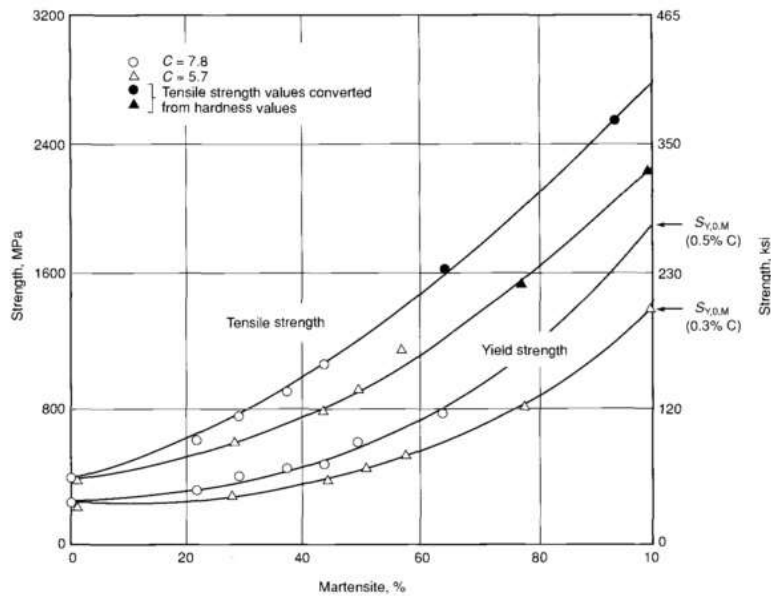


Figure 2.4: Tensile strength versus fraction martensite for a 1.5 wt% Mn DP steel [1].

2.2 Laser Welding

The ability to join materials together is important for manufacturing, particularly in the automotive industry. Many methods exist to join materials which can be broken into physical and metallurgical joints; however, metallurgical joining is generally preferred as it results in the formation of chemical bonds and an overall stronger joint. One type of metallurgical joining is laser welding, which was first used in the 1970's. Figure 2.5 shows a general schematic of the laser welding set up for a butt weld [8]. Laser welding has many advantages including its high power density ($\sim 10^6$ W/cm²), which results in smaller weld fusion zones (FZ) and smaller heat affected zones (HAZ) as well as high joint efficiency. Welding speeds can also be much higher and the precision and ability to automate is much better with laser welding over other types of fusion joining. It is also a very diverse process which can be used on a variety of materials and can be combined with other processes to form more effective hybrid joining methods. [9], [10]

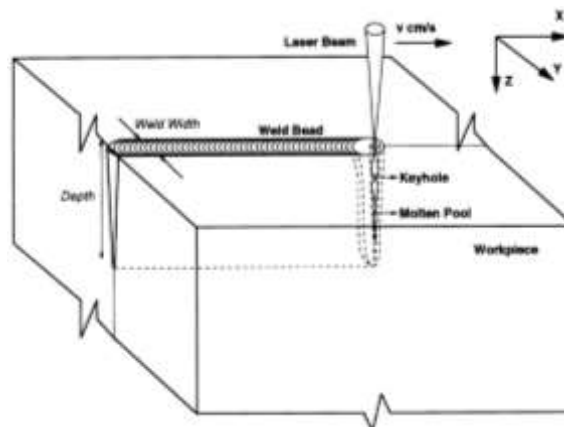


Figure 2.5: Laser welding schematic for a butt weld [8].

Laser welding is performed in either conduction or keyhole welding mode. In conduction mode the laser beam is the heat source which melts the work pieces locally and allows them to join upon solidification, however the energy density is not sufficient to cause boiling and no keyhole is formed. While in keyhole mode, the power density is such that evaporation can occur and a small stable hole is developed within the molten pool, known as the keyhole. The keyhole allows for a very high percentage of the beam energy to be absorbed by the material and thus increases the efficiency and the depth of penetration of the weld [9]. A wide variety of laser types are used in laser welding including CO₂, Nd:YAG, diode and fibre; this work will focus on diode and fibre welds.

2.2.1 Heat Input

There are several methods of calculating the heat input to a weld; however, the direct measurement of this parameter is quite difficult. A variety of numerical models and analytical solutions have been proposed to estimate parameters and calculate weld heat input [11–13]. One such model was developed by Xia et al. [13] and is based on the Rosenthal formulation for a fast moving power source on a thin plate as discussed by Ashby and Easterling and Ion et al., respectively [14], [15].

The temperature profile in the HAZ can be described by equation (2.1), where T_0 is the ambient temperature, Q_{net} is the net laser power, v is the welding

speed, d is the sheet thickness, ρ is the density of the steel, c is the specific heat capacity of the steel, λ is thermal conductivity, a is the thermal diffusivity, t is time, and r is the distance from the weld centreline in the transverse direction [13]. The peak temperature within the heat-affected zone (HAZ) of the weld was calculated by Ashby and Easterling [14] using equation (2.2). By rearranging equation (2.2) for Q_{net}/vd and knowing that the peak temperature within the HAZ is the AC_1 as well as the temperature at the edge of the fusion zone being the melting temperature, equation (2.3) was obtained. This allows for the use of measurements from the microstructure of weld cross sections and known material temperatures (r_{AC1} and r_m are the isotherm positions which correspond to the AC_1 and melting temperatures respectively.) [13]. Figure 2.6 shows the location of these isotherms for a real weld cross-section.

$$T - T_0 = \frac{Q_{net}/(vd)}{\rho c (4\pi a t)^{1/2}} \exp\left(-\frac{r^2}{4at}\right) \quad (2.1)$$

$$T_p - T_0 = \frac{Q_{net}/vd}{\rho c r (2\pi e)^{1/2}} \quad (2.2)$$

$$\frac{Q_{net}}{vd} = \frac{\rho c (r_{AC1} - r_m) (2\pi e)^{1/2}}{\left(\frac{1}{T_{AC1} - T_0} - \frac{1}{T_m - T_0}\right)} \quad (2.3)$$

$$\tau = \frac{1}{4\pi e \lambda \rho c} \frac{[Q_{net}/(vd)]^2}{(T_{AC1} - T_0)^2} \quad (2.4)$$

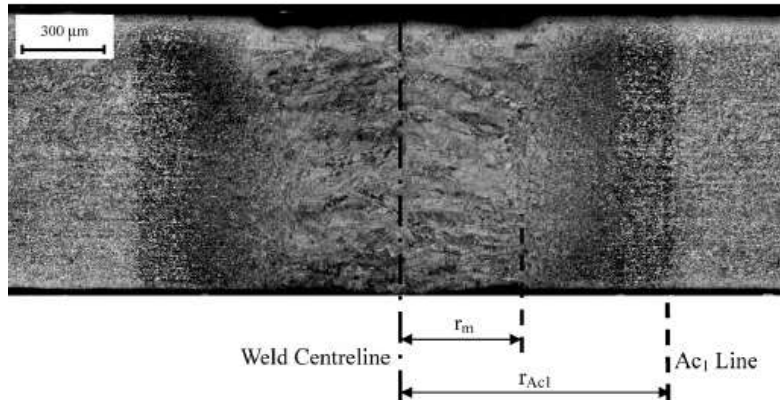


Figure 2.6 Weld cross section showing the measured values for the heat input calculation.[13]

A second parameter, τ or the time constant, is determined by taking the time derivative of equation (2.3), which results in equation (2.4). This time constant represents the tempering time of each weld. Thus, a higher τ means the material in the HAZ experienced temperatures sufficient to temper for longer times [13]. Both of these parameters will be used in this work to compare welds made using different lasers, laser powers and welding speeds.

2.3 Martensite

2.3.1 Structure and Formation

Martensite is a hard microstructural constituent found in quenched carbon steels [16]. For plain carbon steels containing less than 0.4 wt%C, martensite is produced through a diffusionless process whereby the parent fcc austenite (γ) transforms to bct martensite (α') during rapid cooling through a defined shear

with an orientation relationship between the parent austenite and martensite phases defined by the so-called Kurdjumov-Sachs relationship such that [16]:

$$\begin{aligned} (111)_\gamma &\parallel (011)_{\alpha'} \\ [10\bar{1}] &\parallel [\bar{1}1\bar{1}]_{\alpha'} \end{aligned} \quad (2.5)$$

Lath martensite is the most common structural form of martensite and is typical of low and medium carbon martensites while higher carbon steels generally exhibit plate like martensite [17]. An example of both lath and plate martensites are seen in Figure 2.7.

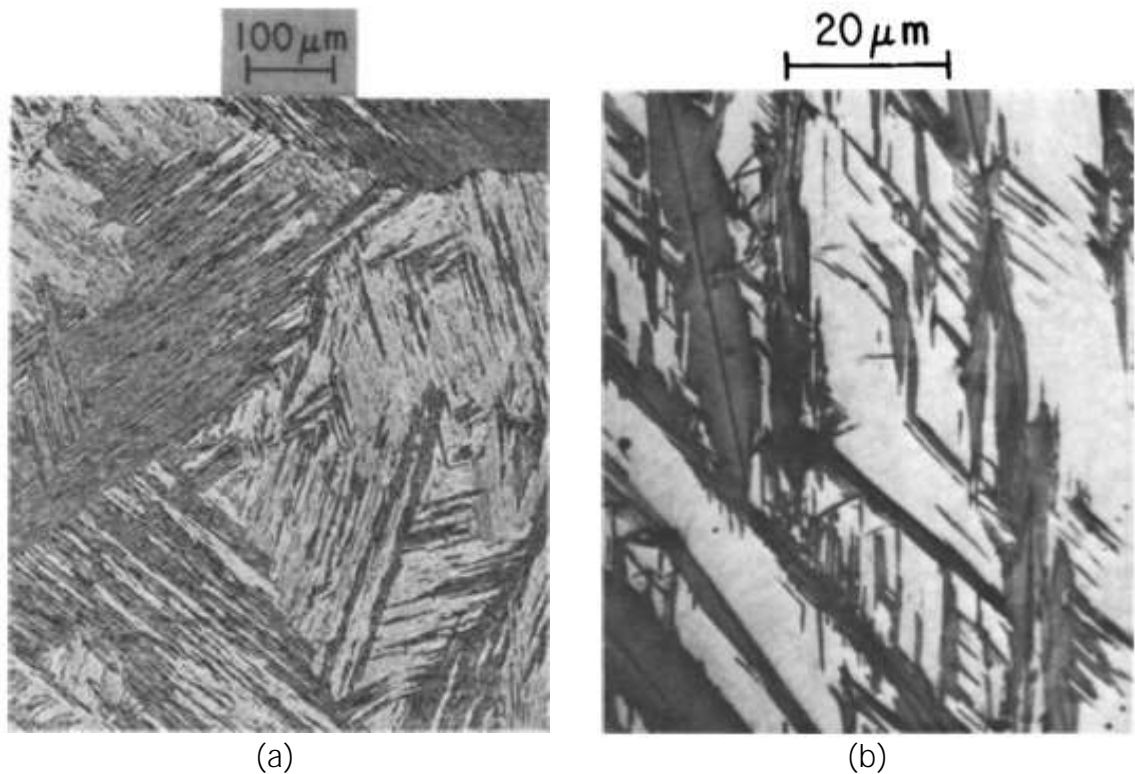


Figure 2.7: Example microstructures of (a) lath martensite in a 0.02% C and 2% Mn steel and (b) plate martensite in a 1.2% C steel [17].

2.3.2 Martensite Tempering

Martensite tempering is one of the most common heat treatments used on steels and is generally carried out in the range of 150 – 700°C. The basic process involves the rejection of carbon from the highly supersaturated martensite solid solution, which ultimately forms a fine dispersion of carbides in a ferrite matrix. There are four overlapping stages of martensite tempering for plain carbon steels. Stage 1 occurs up to 250°C, stage 2 between 200 and 300°C, stage 3 between 200 and 350°C and finally stage 4 above 350°C. In medium and high carbon steels the martensite present is not stable at room temperature, this instability increases up to 250°C [17]–[19].

During stage 1 hexagonal close packed epsilon carbide is precipitated into the martensite structure. Lower carbon steels do not precipitate epsilon carbides and in all cases the martensite remains tetragonal at the end of stage 1. In the second stage of tempering, any retained austenite in the material is decomposed. Some evidence indicates that the austenite is decomposed into bainite, ferrite and cementite. The third stage of tempering results in the loss of tetragonality of the martensite and the appearance of cementite as a Widmanstätten distribution of plates. At the end of this stage, what is left is essentially ferrite that is not supersaturated with carbon and particles of cementite which have undergone Oswald ripening. The fourth stage of martensite tempering can be characterized by the coarsening and spheroidizing of the cementite particles as well as the

recrystallization of the ferrite grains which results in a more equiaxed grain structure of the ferrite matrix. [17]–[19]

The process as outlined above is primarily for plain carbon steels which are fully martensitic and the introduction of alloying elements as well as having multiple phases present can change the progression of the tempering process [18], [19]. The dual phase microstructure of the steels in question also plays a role in the way that the martensite tempers. Work has been done by Baltazar et al. [20] on both the isothermal and non-isothermal tempering of martensite in dual phase steels. To compare the differences in isothermal and non-isothermal tempering of the martensite in dual phase steels, heating to 923 K for varying holding times as well as non-isothermal holding in the form of resistance spot welding was performed. The temperature profiles of the two procedures used are seen below in Figure 2.8.

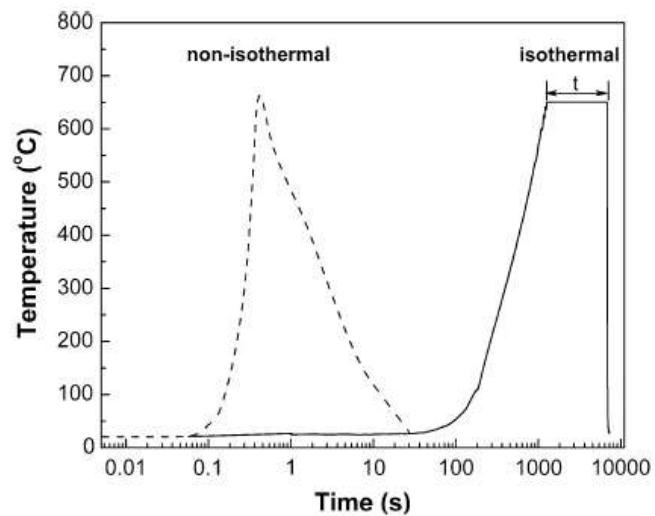


Figure 2.8 Temperature profiles of the isothermal and non-isothermal tempering used in [20].

The DP steels which were tempered isothermally were found to have undergone complete recovery and the cementite particles observed had coarsened. On the other hand, non-isothermally tempered samples demonstrated only partial recovery and very fine cementite particles were observed with different morphologies depending on if they were inter- or intra-lath. A schematic demonstrating the differences in the isothermal and non-isothermal tempering of the martensite islands is seen in Figure 2.9. The authors determined that the fine cementite structure of the non-isothermally tempered steels was due to the higher heating rate, which delayed cementite precipitation and provided insufficient time for significant carbon diffusion [20]. Together these factors retarded the third stage of tempering, i.e. cementite coarsening and spheroidization [20].

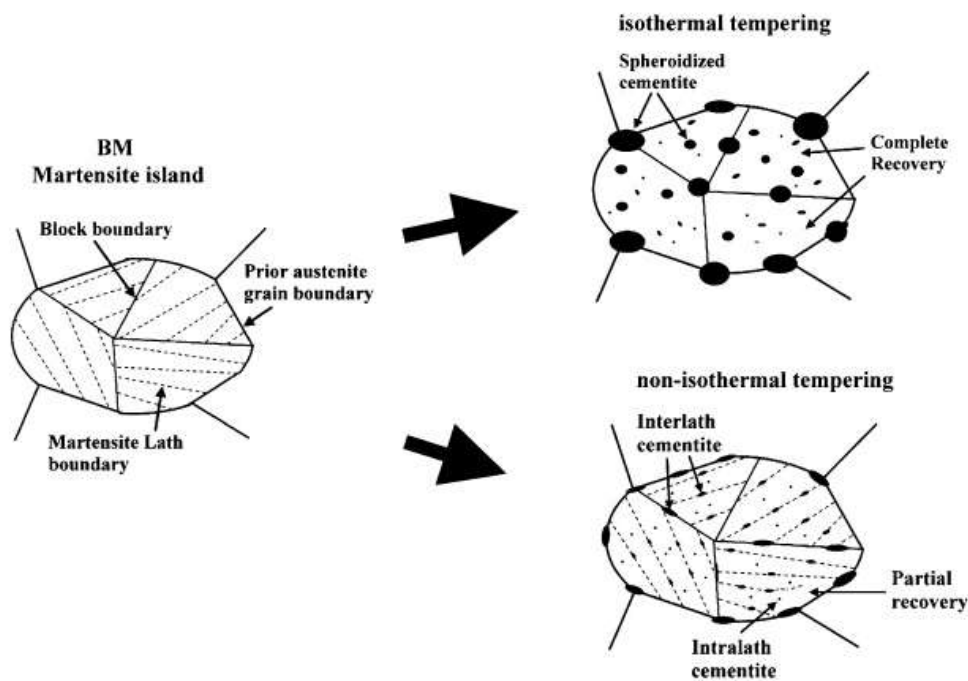


Figure 2.9: Schematic of the differences between isothermal and non-isothermal tempering [20].

Waterschoot et al. [21] also studied the tempering of the martensitic phase within DP steels. The DP steel studied contained 0.08 wt% C and had 12 vol% martensite. They also examined a carbon enriched martensite with 0.72 wt% C and 88 vol% martensite, representative of the martensite phase seen in the DP steel [21]. They found that the DP steel exhibited the same five stages of tempering as did the quenched martensitic steel. The first stage involved the redistribution of carbon atoms at temperatures below 120 °C. The activation energy associated with the first stage was found to be 98.9 -100.6 kJ/mol and corresponded to the activation energy for the bulk diffusion of carbon [21]. The second stage consisted of the precipitation of η - or ϵ -carbides in the temperature range of 120 – 200°C and had an activation energy of 121.6 – 123.8 kJ/mol, which suggests that the rate was controlled by the diffusion of iron. The third stage was observed in the temperature range of 200 – 300°C and comprised Hägg-carbide precipitation. Stage four occurred in the range of 250 – 350°C and involved the decomposition of retained austenite. Finally, all transition carbides were transformed into cementite in the temperature range of 290 – 390C. [21]

The tempering of martensite is an important phenomenon which has a significant effect on the mechanical behavior of the final product. It has been shown in the literature that the martensite phase within DP steels responds in a similar manner to tempering as do quenched martensitic steels [21]. Isothermal and non-isothermal tempering, however can result in differing morphology of the

final tempered structure [20]. It has been shown in the literature that complete recovery and coarsening of the cementite particles has not been observed in non-isothermal tempering which results in a less severe degradation of mechanical properties as compared to isothermally tempered samples [20].

2.4 Bainite

2.4.1 Structure

There are several definitions and understandings of the microstructure referred to as bainite. According to Aaronson et al. [22] there are three definitions of bainite. The first is a general description and describes bainite as the product of the competitive mechanism of eutectoid decomposition [22], [23]. The second is an overall reaction kinetics definition which considers that bainite has a separate C curve on the TTT diagram which lies below the pearlite curve but above the martensite transformation temperatures [16], [22]–[24]. The third is the surface relief definition and advocates that the ferrite plates result in a relief effect on a polished surface [22], [24]. In medium- and high-carbon steels the microstructure consists of a mixture of ferrite and cementite, similar to pearlite, however in bainite the two phases are in non-lamellar arrays [16]. In high- and medium-carbon steels two separate morphologies of bainite have been identified which occur in two temperature ranges; upper bainite and lower bainite [16]. In low-carbon steels there are six recognized morphologies of bainite by

Reynolds et al. [24], the most common of which are upper and lower bainite.

Schematics of the six morphologies are seen in Figure 2.10.

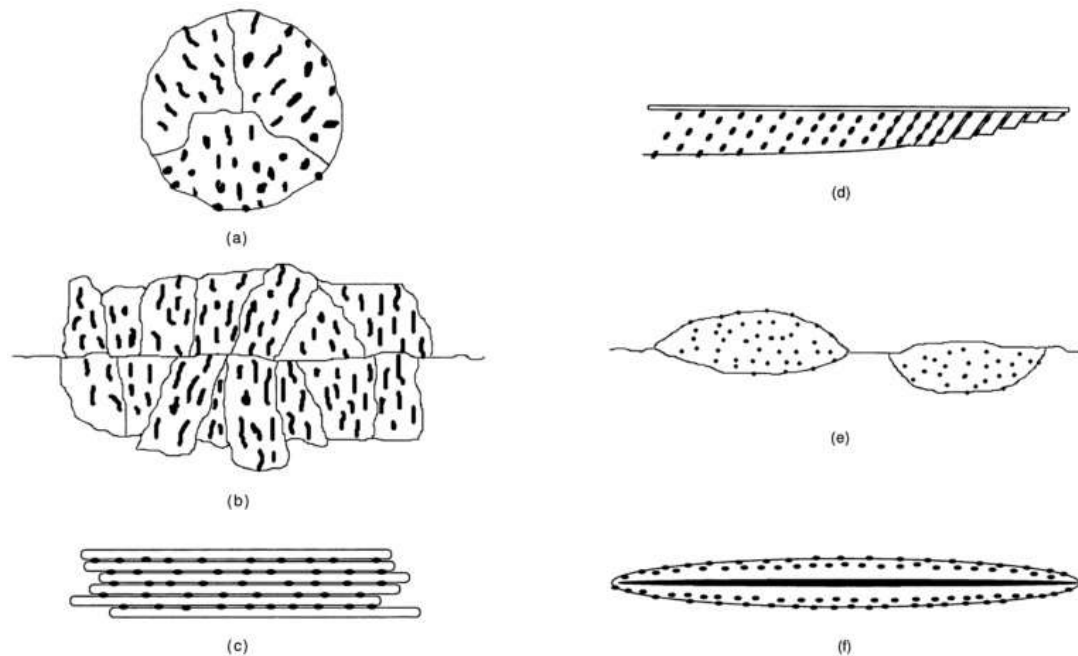


Figure 2.10: Schematic illustrations of various bainite morphologies defined by Reynolds et al. [24]. (a) Nodular bainite, (b) Columnar bainite, (c) Upper bainite, (d) Lower bainite, (e) Grain boundary allotromorphic bainite, (f) Inverse bainite.

2.4.2 Formation

Due to the non-lamellar distribution of cementite within the bainite structure, carbon diffusion is required at some point during the formation of bainite, however the relatively low temperatures at which the transformation occurs restricts iron diffusion [16]. As such, two distinct theories on the formation of ferrite within bainite are prevalent in the literature [16], [25]. The displacive or shear mechanism, supported by Bhadeshia, Edmonds, and Christian [26]–[29] states that bainitic ferrite grows as discrete martensite sub units, the aggregate of these subunits forms the classic sheaf of bainite [27]. The bainitic

ferrite is said to be nucleated with a super saturation of carbon where this carbon is segregated to the residual austenite immediately upon formation [27]. The reconstructive or diffusional mechanism, supported by Reynolds, Spanos, Aaronson, Kinsman, Purdy and Hillert [24], [30]–[34] states that the bainitic ferrite grows as ledges where there is short-range iron atom rearrangement at the ferrite-austenite interfaces of the ledges [16]. The shear growth mechanism allows for phase transformation despite the absence of significant thermal activations [35]. This mechanism also results in each atom from the parent matrix having a predestined site within the product phase and requires glide to accomplish growth much like the formation of martensite [35]. The diffusional mechanism on the other hand, is essentially an uncoordinated jumping of atoms either towards or away from the advancing interface between phases [35]. This results in the ledges during growth due to the difficulty of inserting substitutional atoms into interstitial sites causing displacement in these areas [35].

A full literature search will show that a large amount of work has been done on the mechanism of the bainite transformation; however, there is still not a single unified theory on the subject. Distinction between the two proposed mechanisms is difficult and will require significant further work to determine which is responsible for the formation of bainite in steels.

2.5 Strain Measurement by Digital Image Correlation (DIC)

In order to measure strain in very small mechanical testing specimen as well as to calculate local strain maps using standard tensile specimens it is necessary to use a digital image correlation (DIC) system. The system used in this work was the ARAMIS system. The configuration of the system setup can be seen in Figure 2.11. A pattern of random dots was applied to each sample using spray paint and images were taken at 1 second intervals during the test. The pattern of random dots deforms with the material during the test and allows for the calculation of strain within the sample [36].

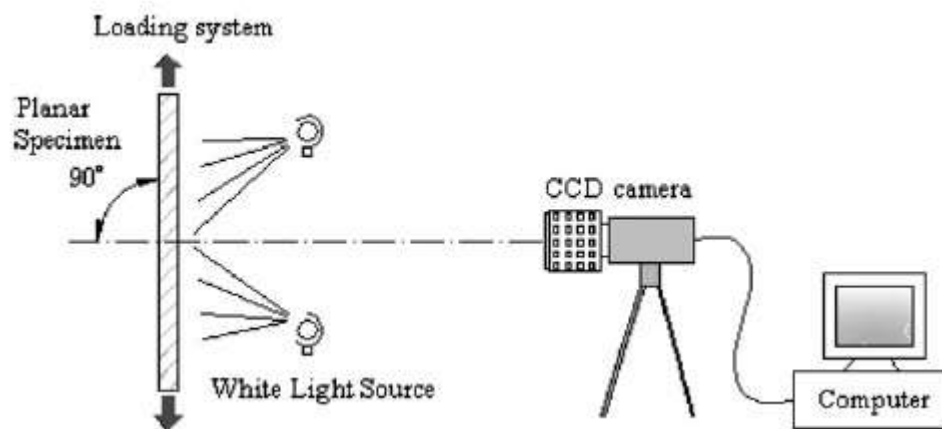


Figure 2.11: DIC system setup [36].

To calculate the strain in the sample, a virtual grid is placed over the region of interest and the deformation vectors at each point are calculated. Figure 2.12 shows a schematic of the displacement vector for a single pixel in the virtual grid [36]. Each of the pixels are tracked through the deformation process and pixels from each image are matched to the pixel they are closest to in the

previous image to calculate the local strain which results in the development of a strain map for the sample at each time step during deformation [36].

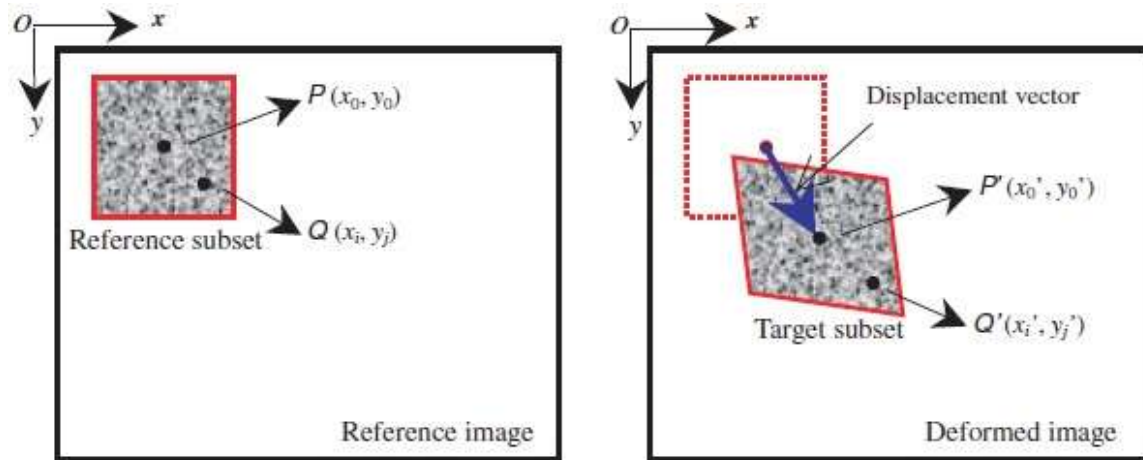


Figure 2.12: Schematic illustration of a reference square subset before deformation and a target (or deformed) subset after deformation [36].

2.6 Effect of Welding on DP Steels – Fusion Zone

The local melting of the work piece during welding means that the microstructure of the fusion zone of laser welded DP steels is formed upon the solidification of the molten weld pool. As such, the final microstructure can be predicted by continuous cooling transformation (CCT) curves as well as the relevant phase diagram for the steel chemistry [16]. An experimentally measured CCT curve for the steel examined in the present study is presented in Figure 2.13 [37]. From this curve, it can be seen that, depending on the local cooling rate within the fusion zone, ferrite, bainite or martensite can be obtained. Figure 2.13 shows that when cooling rates are above 100 °C/s martensite with a small volume fraction of ferrite is produced, while cooling rates between 10 and 100 °C/s will

allow for the formation of ferrite and martensite, and finally if cooling rates are below 10 °C/s bainitic ferrite is able to form alongside the ferrite.

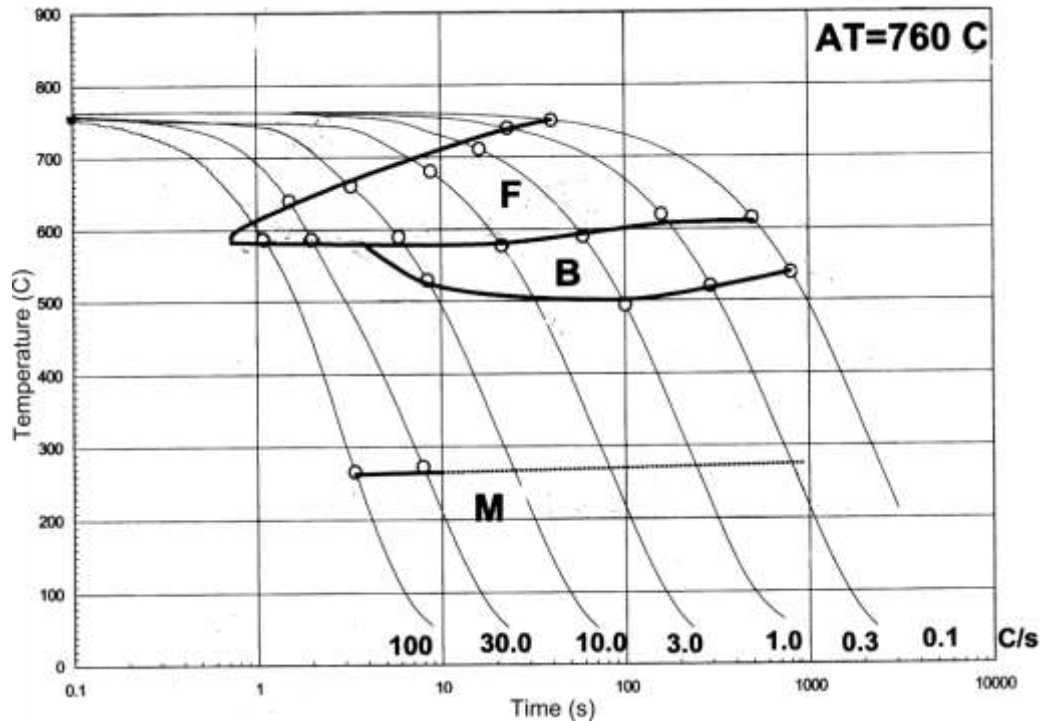


Figure 2.13: CCT curve for DP780 steel with cooling curves superimposed[37].

2.7 Effect of Welding on DP Steels - HAZ

Tempering of the martensite within the HAZ of the weld has been shown to cause a depression of the hardness (and strength) of this microstructural zone which is known as HAZ softening [4], [5], [13], [20], [38]. The current research on this phenomenon is discussed in section 2.7.1 below. As well, the bulk mechanical properties including tensile and fatigue strength of laser welded DP steels have been studied using a variety of DP steels and welding conditions [39]–[43]. The formability of laser welded DP steels has also been investigated [44]–[46]. Both

the bulk mechanical properties and the formability of laser welded DP steels are further discussed in section 2.7.2 of this chapter.

2.7.1 Softening Kinetics

The kinetics of the softening process have been studied by a number of researchers [4], [5], [13], [21], [38]. As mentioned in section 2.2.1, Xia et al. developed a method of normalizing the heat input of welds which allows for the comparison of welds made under varied conditions [44]. This technique has been used by several authors to investigate the kinetics of the HAZ softening process. The study by Biro et al. [4] employed a parameter, ϕ (per equation (2.6)), which represents the normalized hardness change arising from martensite tempering, where the parameter is zero when the material is in its as received state and is equal to one when the material has been fully tempered; this parameter was also used by Mittemeijer et al. [47]. This parameter is calculated per equation (2.6), where H_{Base} is the hardness of the base material, H_{min} is the minimum hardness value for a given material in the fully tempered state and H is the hardness of the evaluated sample [4]. They found that when the ϕ parameter was plotted against the time constant (see section 2.2.1), sigmoidal behaviour was observed as can be seen in Figure 2.14 [4]. This behaviour was then fitted to the Avrami equation [48]–[50] of transformation (equation (2.7)), where k is a fitting parameter representing the activation energy, t is the tempering time, and n is a fitting parameter related to the rate of transformation [4].

$$\phi = \frac{H_{Base} - H}{H_{Base} - H_{min}} \quad (2.6)$$

$$\phi = 1 - \exp(-kt^n) \quad (2.7)$$

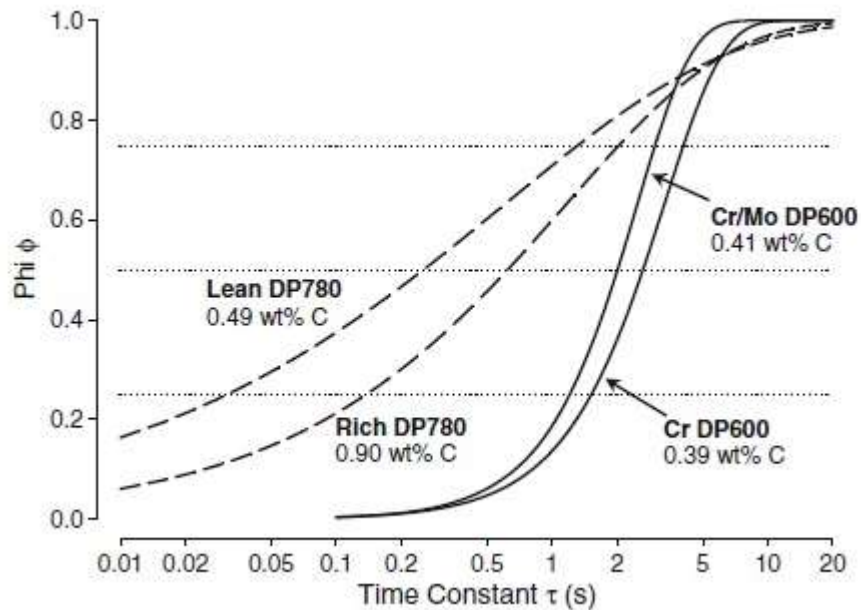


Figure 2.14: Comparison of HAZ softening kinetics, phi versus time constant of all experimental steels examined by Biro et al. [4].

Biro et al. also found that the n-parameter fitted to each of the curves was much lower than what would be predicted by Avrami for pure particle nucleation and growth [4]. Instead the values calculated for the DP780 steels used (approximately 0.5) were representative of the martensite decomposing as a receding front [4]. The DP600 steels had n parameters of 1.6 and 1.7 suggesting that there was less autotempering of the martensite and, therefore, the decomposition of the martensite occurred as both a receding front and nucleation of new cementite particles which increased the n parameter [4].

In another study, Biro et al. [5] examined the short time tempering of DP steels using a Gleeble in order to predict the softening behaviour of the HAZ of welds made in these materials. Four DP and three fully martensitic steels were examined by tempering for times ranging from 0.2 s to 10 s, which is representative of the times which the sub-critical HAZ is at elevated temperature during welding [5]. The model used previously [4], was used to model the kinetics with the Johnson-Mehl-Avrami-Kolomogorov (JMAK) equation. The k fitting parameter in equation (2.7) was modeled using equation (2.8), where k_0 is a fitting parameter, Q is the activation energy for softening, R is the universal gas constant and T is the absolute temperature [5].

$$k = k_0 \exp\left(\frac{-Q}{RT}\right) \quad (2.8)$$

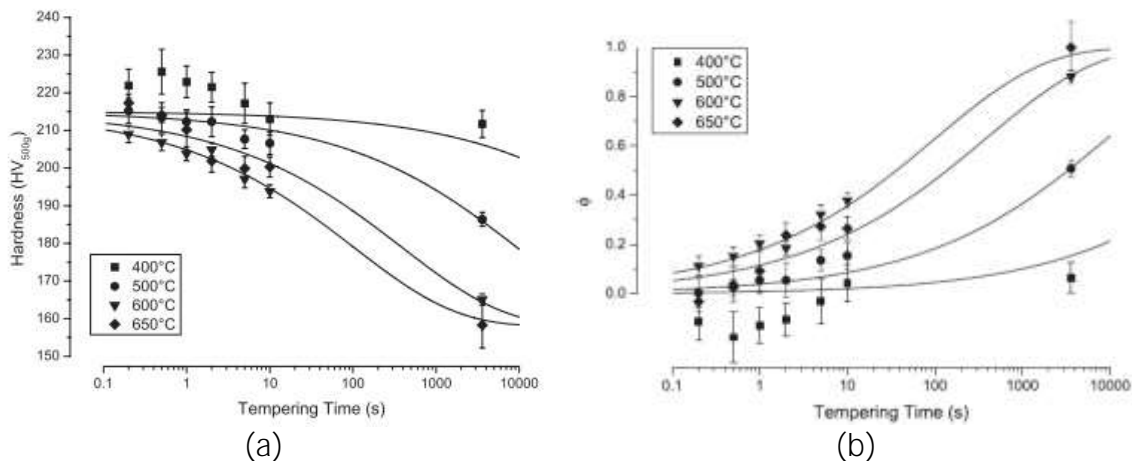


Figure 2.15: DP780 data from Biro et al. [5] (a) hardness plotted versus tempering time and (b) transformed data to phi (fraction of completed softening) versus tempering time.

Figure 2.15(a) shows the hardness data for the DP780 steel examined plotted against the tempering time. It is seen that at a given tempering

temperature the hardness decreased sigmoidally with tempering time and that the hardness decreased with increasing temperature [5]. The transformed data is seen in Figure 2.15(b), where the phi parameter versus tempering time shows the classic JMAK form. Using equation (2.8) Q , k_0 and n values were calculated for all experimental steels, the values fitted for activation energy (Q) and n were significantly different from typical values associated with martensite tempering using the JMAK equation [5]. The activation energies reported for the seven experimental steels were between 28.3 – 62.8 kJ/mol [5]; generally the literature reports higher values for the activation energies (176.1 – 203 kJ/mol) [21], [51]–[53] for stage three tempering although in these studies the activation energy was measured in a more direct way through dilatometry as opposed to through the hardness measurements used in the work of Biro et al. [5]. Other researchers who measured the activation energy of this process in a similar manner (through hardness measurements) report values which were more similar, 33.5 – 209 kJ/mol [54], [55]. As with the previously mentioned work [4], the fitted values of n also did not correspond with classic JMAK values for spherical particles. In order to validate this model using the JMAK equation, hardness values measured from actual weld heat-affected zone were compared with the values predicted using the model in Figure 2.16(a) and then the HAZ softening was calculated in both cases and the measured and predicted values compared as shown in Figure 2.16(b). It is seen that both the absolute hardness values and HAZ softening

values were accurately predicted through short hold time isothermal tempering experiments.

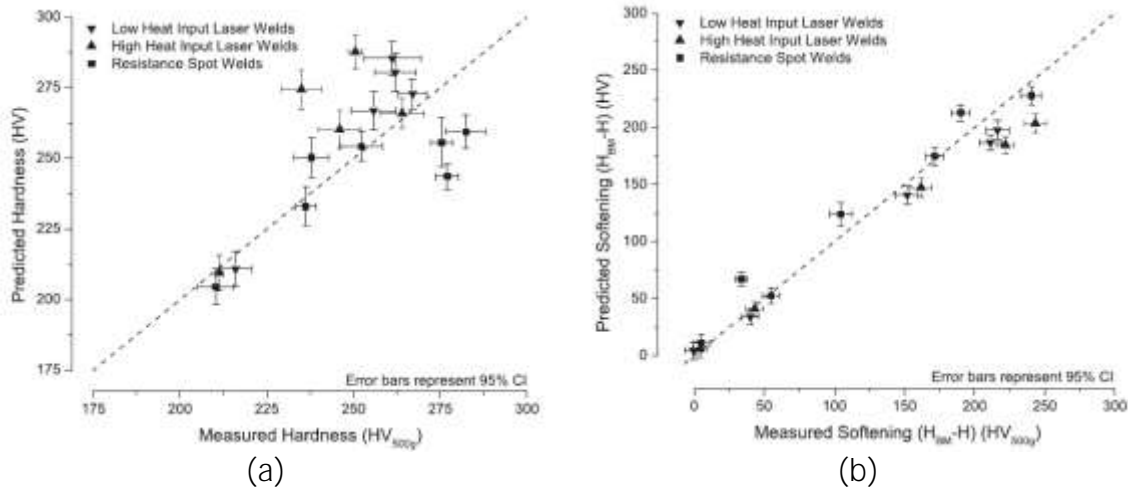


Figure 2.16: Validation of the softening model (a) comparison of measured hardness and the hardness predicted by the JMAK model and (b) comparison of the measure HAZ softening and the HAZ softening predicted by the JMAK model [5].

Due to the discrepancies between the values of Q and n which were calculated by Biro et al. [5] and the typical values reported for stage III martensite tempering, a logarithmic transformation of the softening data was performed [38]. This transformation allowed the n and k values to be determined directly from the plot (Figure 2.17) as the slope and the y-intercept, respectively. From Figure 2.17, two distinct stages of HAZ softening are visible [38]. The n and Q values for stage I softening were found to be 0.659 and 113 kJ/mol respectively [38]. These values are in good agreement with the accepted values of n and k for carbon diffusion in ferrite from the literature of 0.67 and 80 – 122 kJ/mol, which is the dominant process in the initial stages of martensite tempering. Thus, the stage I softening was determined to be equivalent to stage

3 of martensite tempering [38]. For stage II softening, the n and k values were calculated to be 0.108 and 35 kJ/mol, respectively, and are representative of the carbide growth phase of HAZ softening [38].

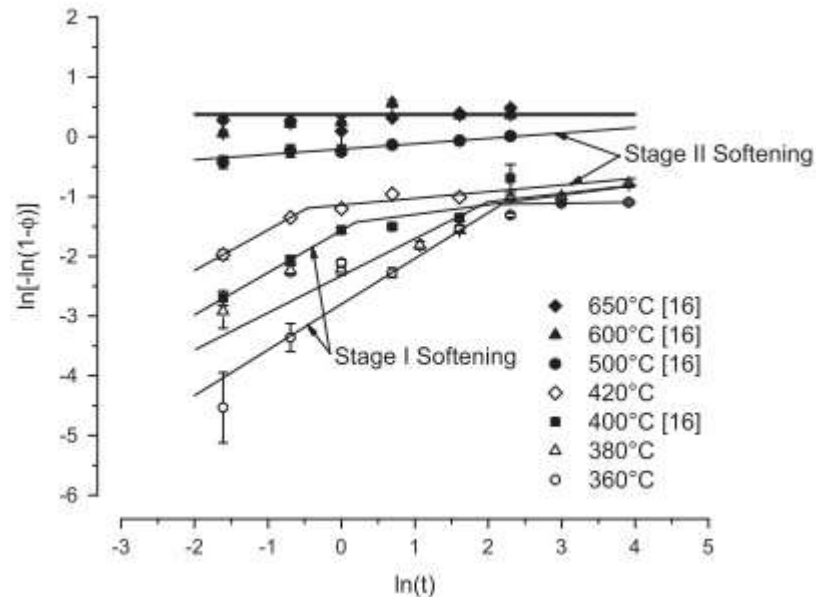


Figure 2.17: Logarithmic transformation of M220 softening data from [38].

Overall the kinetics of HAZ softening have been found in the literature to be sigmoidal and well modelled by the JMAK equation [4], [5], [13], [38]. It has been shown that short time isothermal tempering experiments can accurately predict the absolute hardness and softening of DP and martensitic steel weld heat-affected zones using the JMAK equation [4, 5]. Finally, two stages of HAZ softening were found through the logarithmic transformation of the softening data which correspond to carbide nucleation and growth respectively [38].

2.7.2 Bulk Mechanical Properties

The mechanical properties of laser welds are generally evaluated by pulling the weld in tension using an ASTM standard sample with the weld centred in the gauge and the weld centreline perpendicular to the tensile direction. Stress – strain curves are often calculated, however, there are multiple materials within the gauge making standard stress calculations inaccurate. The failure location is also documented and generally, if the weld fails within the base material, weld design can be done based on BM mechanical properties; however, this is not always the case. A variety of bulk mechanical property investigations on laser welded DP steels can be found in the literature including, tensile, fatigue and forming studies [39]–[43], [45], [46], [56]–[59].

A number of studies have shown that the tensile properties of DP steels are negatively impacted by welding. UTS, YS and uniform elongation have been shown to decrease in welded samples as compared with the BM, the type of laser used, and thus the heat input to the welded sample has also been shown to have an affect [39]–[41], [43], [56].

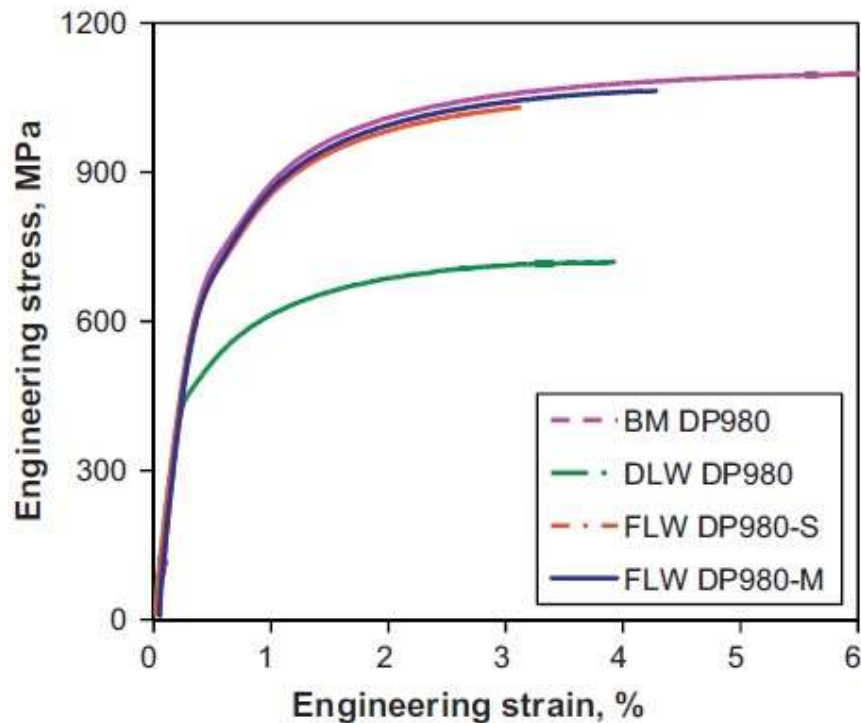


Figure 2.18: Representative stress-strain curves for DP980, BM, diode laser welds, single pass fibre laser welds, and multiple fibre laser welds from Xu et al. [41].

Figure 2.18 from Xu et al. shows the effect of fibre laser and diode laser welding on a DP980 steel. It is seen that the diode welding process had a much more significant impact on the mechanical properties of the joint [41]. In all cases, however there was a depression of the UTS, YS and uniform elongation of the welded joint as compared to the base material [41].

The effects of laser welding on the formability of DP steels has also been studied, through limiting dome height (LDH) testing [44]–[46], [58]. Figure 2.19 shows the LDH measured for both BM and welded materials from which it is seen that the LDH of welded DP steels is generally lower than the LDH of the corresponding BM.

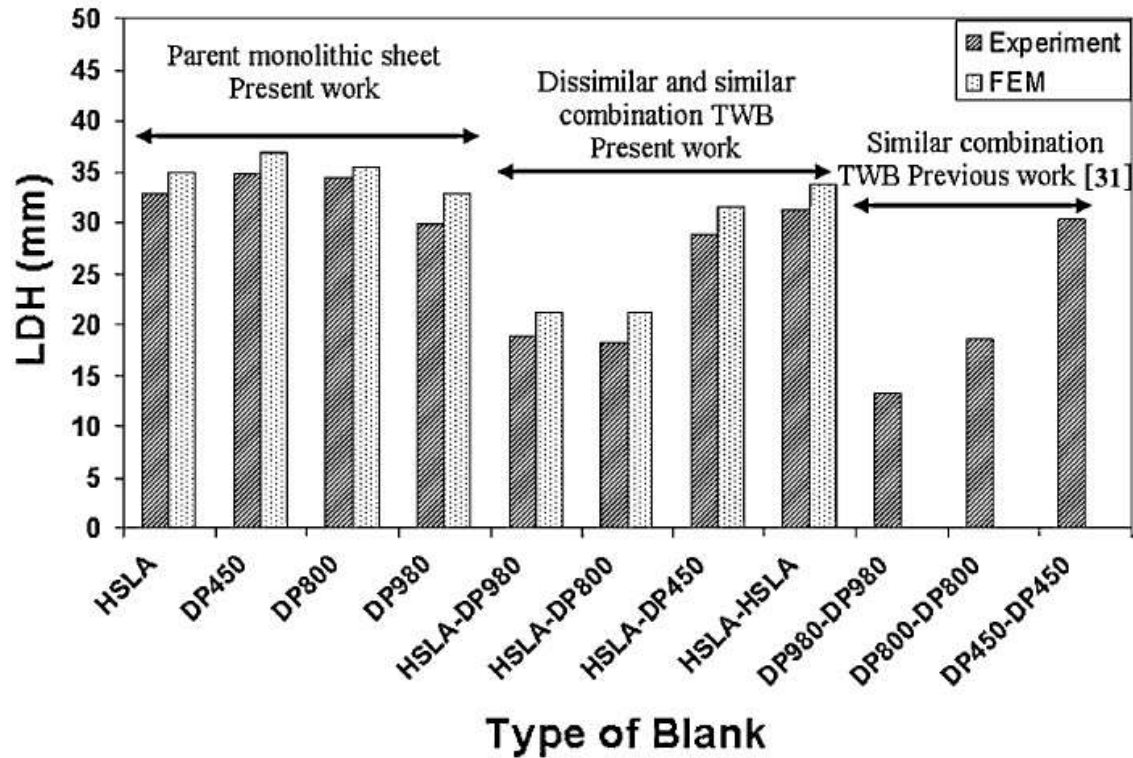


Figure 2.19: Comparison of LDH of parent material with tailor welded blanks (TWB) of different material combinations from Panda et al. [46].

Overall, mechanical testing of welded DP steels has been limited to bulk property evaluation by means of uniaxial tensile, fatigue and LDH testing and the mechanical properties of individual weld zones have not been widely investigated in the literature [60]. This is an area of importance as we continue to drive down vehicle weight for increased fuel efficiency as passenger safety is still of extreme importance. As such, the ability to model the properties of welds through finite element simulations and to fully understand the behaviour of each component of the weld (microstructural zones) becomes key to predicting weld failure locations and the strengths and performance of structural components. This fundamental understanding of mechanical behaviour is currently lacking in the literature.

CHAPTER 3 **Research Objectives**

It has been shown in the previous chapter that there has been substantial research into the effects of laser welding on DP steels; this work tends to focus on the kinetics of the tempering process which causes the HAZ softening as well as examining the bulk properties of welded samples. There is, however, a lack of understanding and data on the mechanical properties of each of the individual microstructural zones of laser welded DP steels. To this end, the objectives of the present study are to examine laser welds made in DP 780 steel by studying the microstructure and mechanical properties of the welded steel sheet. Specifically, the research objectives of this study are:

1. Characterization of the microstructure across welds made with varying heat input in a DP780 steel.
2. Determine the mechanical properties of the microstructural zones of each weld through the development and testing of non-standard testing geometries.
3. Compare the mechanical properties of each weld with respect to heat input.
4. Determine the location of failure in welds with varied heat input

CHAPTER 4 **Experimental Methods**

4.1 Materials

This study employed an industrially produced 1.5 mm thick dual phase steel (DP780) produced by ArcelorMittal (Dofasco), whose chemistry is given in Table 4.1. Mechanical tests and characterization were carried out on the as-received cold rolled steel sheet.

Table 4.1: Chemical Composition of DP780 Steel

	C	Mn	P	S	Si	Al	Ti
wt %	0.100	1.75	0.014	0.005	0.310	0.050	0.003

The microstructure of the as-received materials was characterized using optical microscopy following standard metallographic preparation and etching using 2% nital. Samples were observed both parallel and perpendicular to the rolling direction. The base material microstructure is pictured in Figure 4.1, where it can be seen that the as-received microstructure consisted of martensite islands within a ferritic matrix.

The Vickers hardness of the as-received material was measured using both a 200 g and 500 g load. The Vickers hardness of the base materials was measured as $252 \pm 6.2 \text{ gf}/\mu\text{m}^2$ and $236 \pm 4.0 \text{ gf}/\mu\text{m}^2$ at 200 g and 500 g loads respectively. Details concerning the microhardness measurement procedure are provided below.

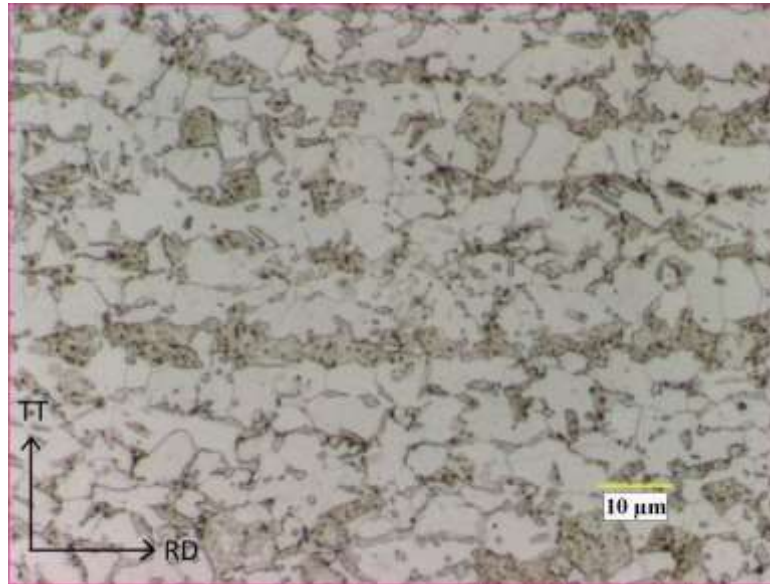


Figure 4.1: Base material microstructure; dark regions represent martensite while the light regions are the ferrite matrix.

4.2 Welding Conditions

Bead-on-plate welds were made in the DP780 steel using two different laser systems with varied laser power and welding speed. The various lasers and welding parameters used are given in Table 4.2. All welds were fully penetrating and the welding direction was parallel to the rolling direction of the sheet steel in all cases.

Table 4.2: Laser Parameters for Welding of DP780.

	Diode Laser Welds	Fibre Laser Welds
Power(W)	4000	4000, 6000
Shielding gas	Argon	Argon
Focal length (mm)	80	200
Beam Size (mm)	0.9 x 12	0.6
Welding Speeds (m/min)	0.8, 1.0, 1.2	2, 4

4.3 Weldment Characterization

Optical microscopy was employed to qualitatively evaluate the changes in microstructure across the welded joints. To compare the joints, normalized heat input was calculated for each of the weldments. Microhardness profiles were also used to determine quantitatively the changes in the properties across each of the welds. Finally, various mechanical testing geometries were employed to determine the stress-strain behaviour of each weldment microstructural zone.

4.3.1 Microscopy

Transverse cross-sections of each weldment were prepared using standard metallographic procedures and etched using 2% nital. A Nikon Eclipse LV100 optical microscope was used to observe the samples.

4.3.2 Heat Input

In order to compare welds made with different lasers and power levels, a normalized heat input for each weld was calculated. The heat input was calculated using the method developed by Xia et al. [13] based on the Rosenthal equation. This method is described in more detail in Section 2.2.1. The distance from the centerline to the edge of the fusion zone and to the Ac1 isotherm were measured as is seen in Figure 4.2 and these values were used in equation (4.1) [13] to calculate the normalized heat input $\left(\frac{Q_{net}}{vd}\right)$ of each weldment, where ρ is the

density of steel (7860 kg/m^3), c is the specific heat capacity of steel (680 J/kg/K), T_0 is the initial temperature, about 293 K , and r_{AC1} and r_m are the isotherm positions corresponding to the T_{AC1} and T_m (melting temperature) respectively. The time constant (τ) of each weld was then calculated using equation (4.2) [13], where λ is the steel thermal conductivity ($30 \text{ W/m}\cdot\text{K}$).

$$\frac{Q_{net}}{vd} = \frac{\rho c (\pi r_{AC1} - r_m) (2\pi e)^{1/2}}{\left(\frac{1}{T_{AC1} - T_0} - \frac{1}{T_m - T_0} \right)} \quad (4.1)$$

$$\tau = \frac{1}{4\pi e \lambda \rho c} \left[\frac{Q_{net}}{vd} \right]^2 (T_{AC1} - T_0)^2 \quad (4.2)$$

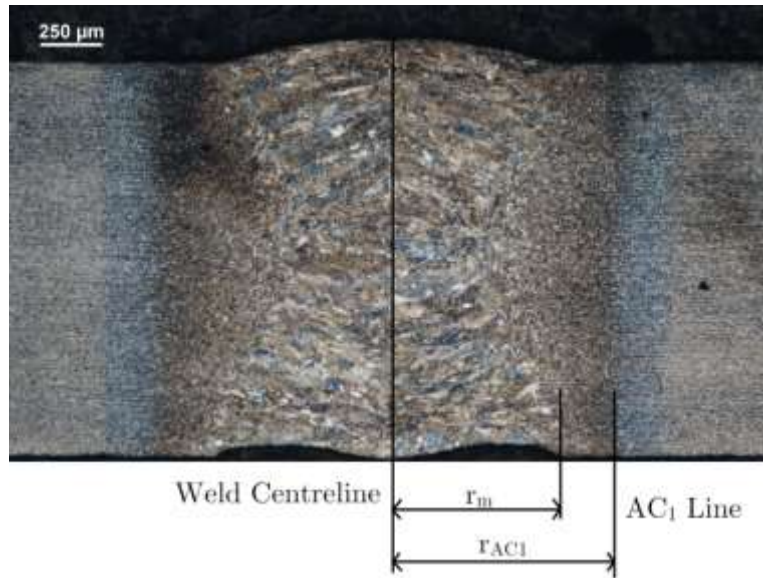


Figure 4.2: Cross section of a weld showing the boundaries for heat input calculations.

4.3.3 Microhardness Profiles

Microhardness was measured across each of the weldments using a Clemex CMT.HD microhardness tester. A 200 g and 500 g load, with a 10 s dwell time,

were used for the fibre and diode welds respectively and indents were placed at least 2.5 diameters from one another to ensure that the strain fields from neighbouring indents did not affect the measurement[61]. In order to achieve adequate spacing as well as adequate spacial resolution, indents were staggered vertically in the region near the weld bead for the fibre welds. This vertical staggering allowed for the resolution of the very small softened region in the fibre welds. Each profile presented is an average of three measurements and the error bars shown represent the 95% confidence interval of the mean reading, defined as:

$$\mu = \bar{x} \pm t_{N-1,95\%} \frac{s}{\sqrt{N}} \quad (4.3)$$

where μ is the true value of the measurement, \bar{x} and s are the sample mean and standard deviation, respectively, $t_{N-1,95\%}$ the value of the student t-distribution at degrees of freedom $N-1$ evaluated at the 95% level (i.e. 0.95) and N the number of samples.

4.4 Mechanical Testing

To test the mechanical properties of the base material, ASTM E8 [62] standard sub size tensile samples were used to determine stress-strain curves in both the rolling and transverse directions. ASTM standard sub-size samples were also pulled for each welding condition, with the weld centred vertically within the gauge and the tensile direction perpendicular to the welding direction. Each of the across weld tests were repeated twice. All samples were pulled using an

Instron 5566 tensile frame in combination with an ARAMIS DIC system to calculate strain. Unless otherwise noted, a constant cross-head speed of 1 mm/min was used.

To test the mechanical properties of the smaller weld microstructural zones of the diode welds, miniature tensile samples were designed such that the entire gauge consisted of only fusion zone or heat-affected zone material. The dimensions and general design of these specimens are shown in Figure 4.3.

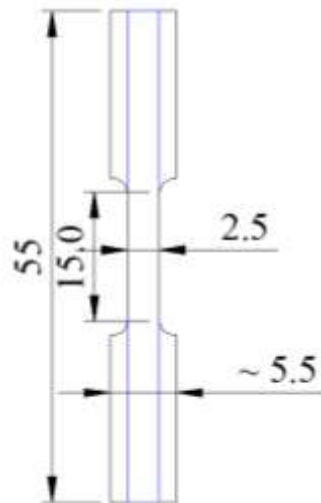


Figure 4.3: Geometry of miniature tensile mechanical testing sample (all dimensions in mm).

To test the mechanical properties of the diode weld zones in the transverse direction as well as the fibre weld microstructural zones, which were too small for the miniature tensile specimens, a plane strain specimen geometry was used. The dimensions and general design of the specimens for the diode welds are shown in Figure 4.4. The region between the notches in these samples consisted entirely of fusion or heat-affected zone material.

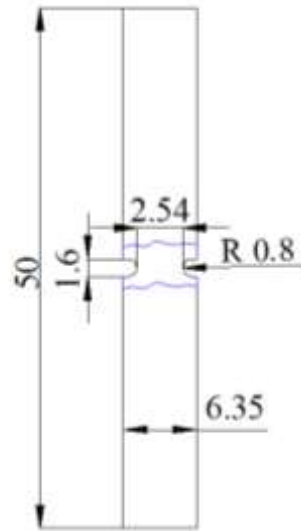


Figure 4.4: Geometry of a plane strain sample for mechanical testing of diode weld microstructural zones (all dimensions in mm).

The size of the fibre welds did not allow for the fabrication of miniature tensile specimens or the plane strain specimens shown in Figure 4.3 and Figure 4.4, respectively. Instead a much smaller notch and gauge section were used to ensure that fracture localization was within the desired microstructural region. The dimensions and design of these specimens are seen in Figure 4.5. A constant cross head speed of 0.5 mm/min was used in these cases in order to capture the stress-strain curve for the smaller sample geometry.

For each testing geometry, six samples were pulled per welding condition for both the heat-affected zone and the fusion zone. For yield strength and ultimate tensile strength, a 95% confidence interval was used for error calculations per equation (4.3).

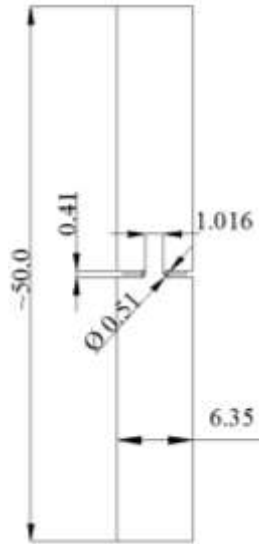


Figure 4.5: Geometry of plane strain sample for mechanical testing of fibre weld microstructural zones (all dimensions in mm).

4.4.1 Effective Stress- Effective Strain Calculation

In order to directly compare the mechanical testing results irrespective of the sample geometry and strain path, effective stress and effective strain were used throughout this study. For the ASTM standard and miniature uniaxial tensile samples the effective stress and effective strain were equal to the true stress and true strain based on the Von Mises criterion. The Von Mises equation for effective stress (σ_{eff}) is given in equation (4.4) [63], where for uniaxial tension $\sigma_2 = \sigma_3 = 0$ [63] and the effective stress is simply the true stress in the tensile (σ_1) direction.

$$\sigma_{eff} = \sqrt{\frac{1}{2}[(\sigma_1 - \sigma_2)^2 + (\sigma_2 - \sigma_3)^2 + (\sigma_3 - \sigma_1)^2]} \quad (4.4)$$

The equation used to calculate true stress from engineering stress in the case of uniaxial tension is shown in equation (4.5) [63].

$$\sigma_{true} = \sigma_{eng} (1 + \epsilon_{eng}) \quad (4.5)$$

The Von Mises equation for effective strain is shown in equation (4.6) [63]. Using equation (4.7) (conservation of volume) and knowing that for uniaxial tension $\epsilon_2 = \epsilon_3$ for an isotropic material [63] we can determine that the effective strain is simply the true strain in the tensile direction in the case of uniaxial tension.

$$\epsilon_{eff} = \sqrt{\frac{2}{3}(\epsilon_1^2 + \epsilon_2^2 + \epsilon_3^2)} \quad (4.6)$$

$$\epsilon_1 + \epsilon_2 + \epsilon_3 = 0 \quad (4.7)$$

The notched specimens, however, follow a different strain path. According to Wagoner and Chenot [64], if $|\epsilon_2/\epsilon_1|$ is less than 0.2 then the region is considered to be in plane strain. Performing these calculations for each of the notched specimens showed that samples were in plane strain (see APPENDIX A). Using the Von Mises equation for effective strain in equation (4.6) and equation (4.7) where for plane strain, $\epsilon_2 = 0$ [63] it is found that the effective strain for the plane strain geometry is given by equation (4.8).

$$\epsilon_{eff} = \frac{2}{\sqrt{3}} \epsilon_1 \quad (4.8)$$

To calculate the effective stress for the plane strain samples equation(4.4), the Von Mises effective stress, is once again employed. For plane strain we assume that $\sigma_3 = 0$ [63] and if we let the ratio $\frac{\sigma_2}{\sigma_1} = \alpha$ and the ratio $\frac{\varepsilon_2}{\varepsilon_1} = \beta = 0$ (ref), we can express the effective stress as equation (4.9). From flow rules [63] we can also write equation(4.10), which gives $\alpha = \frac{1}{2}$ and, thus, the effective stress is given by equation(4.11).

$$\sigma_{eff} = \sqrt{\frac{1}{2}[\alpha^2 + 1 + (1-\alpha)^2]} \sigma_1 \quad (4.9)$$

$$\frac{\varepsilon_2}{\varepsilon_1} = \frac{2\alpha - 1}{2 - \alpha} = \beta \quad (4.10)$$

$$\sigma_{eff} = \frac{\sqrt{3}}{2} \sigma_1 \quad (4.11)$$

CHAPTER 5 Results

The results of the present study are presented in the following chapter. The first part of the chapter will examine the variations in microhardness across each of the weldments and discuss the various microstructural regions which were observed. In the next section, the microstructures of each of these zones will be presented through optical micrographs. Finally, the mechanical behaviour of the base material, overall weldments and the individual microstructural zones will be presented. The nomenclature for each sample presented in the subsequent text are summarize in Table 5.1.

Table 5.1: Sample nomenclature.

Weld Name	Laser	Power (kW)	Speed (m/min)
4kW (D) 0.8	Diode	4	0.8
4kW (D) 1.0	Diode	4	1.0
4kW (D) 1.2	Diode	4	1.2
4kW (F) 2.0	Fibre	4	2.0
4kW (F) 4.0	Fibre	4	4.0
6kW (F) 2.0	Fibre	6	2.0
6kW (F) 4.0	Fibre	6	4.0

5.1 Microhardness Profiles

5.1.1 Diode Welds

A typical hardness profile for a 4kW (D) 0.8 weld is given in Figure 5.1. It is seen that the hardness in the fusion zone (FZ) was elevated compared to that of the base material (as reported in Section 4.1 and Figure 5.1). The hardness

was also non-uniform across the fusion zone. A softened region was observed in the region adjacent to the fusion zone (FZ); this is known as the sub-critical heat-affected zone (referred to as heat-affected zone or HAZ in the subsequent text). The average value for the hardness of the FZ was found to be $257 \text{ gf}/\mu\text{m}^2$ and the minimum hardness observed in the HAZ was found to be $184 \text{ gf}/\mu\text{m}^2$ (see Table 5.2).

Table 5.2: Summary of diode weld hardness measurements.

Welding Speed (m/min)	Average FZ Hardness	Minimum HAZ Hardness	HAZ Softening versus BM
0.8	257 ± 4.0	184 ± 1.4	64.4 ± 2.4
1.0	280 ± 6.4	185 ± 2.1	61.5 ± 4.1
1.2	298 ± 5.7	192 ± 1.2	54.5 ± 2.7

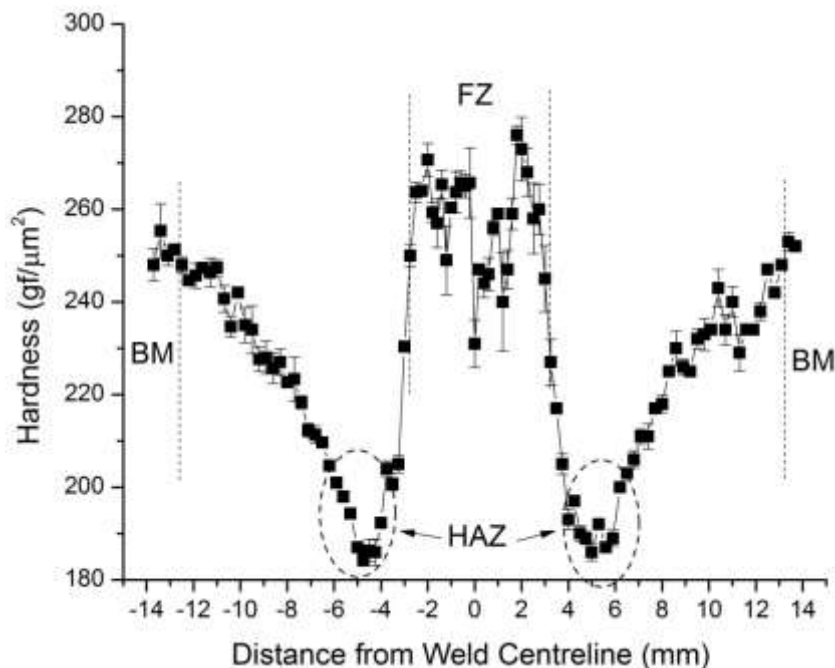


Figure 5.1: Typical microhardness profile of a 4 kW (D) 0.8 weld, where BM is the base material, HAZ is the heat-affected zone and FZ is the fusion zone.

A typical hardness profile for a 4kW (D) 1.0 weld is presented in Figure 5.2. The softened HAZ was observed adjacent to the fusion zone. It can also be seen that the hardness of the FZ was elevated compared to the base material (as reported in Section 4.1 and Figure 5.2) and that there was a more pronounced variation in the hardness across the FZ. In this case, the average FZ hardness value was found to be $280 \text{ gf}/\mu\text{m}^2$ while the minimum hardness of the HAZ was found to be $185 \text{ gf}/\mu\text{m}^2$ (see Table 5.2).

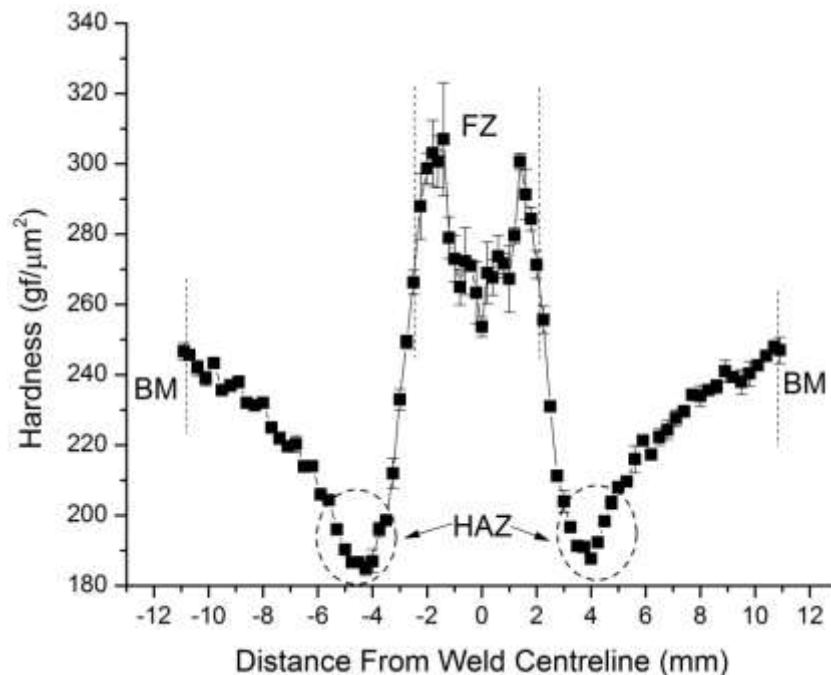


Figure 5.2: Typical microhardness profile of a 4 kW (D) 1.0 weld.

Finally, a typical hardness profile of a 4 kW (D) 1.2 weld is presented in Figure 5.3. A further elevated hardness compared to the base material (average value of $298 \text{ gf}/\mu\text{m}^2$, see Table 5.2) with very pronounced hardness variations was observed in the FZ of this weld. This likely indicates a larger volume fraction of

martensite and increased strength in this microstructural zone of the weld. Softening of the HAZ was again observed, although to a lesser extent than with the other two diode welds (minimum hardness value of $192 \text{ gf}/\mu\text{m}^2$, see Table 5.2).

In all cases, an important similarity of the hardness profiles was the large range in hardness values obtained across the width of the welds. This indicates that there was a significant contrast in microstructure and, very likely, mechanical properties, across each of the diode welds.

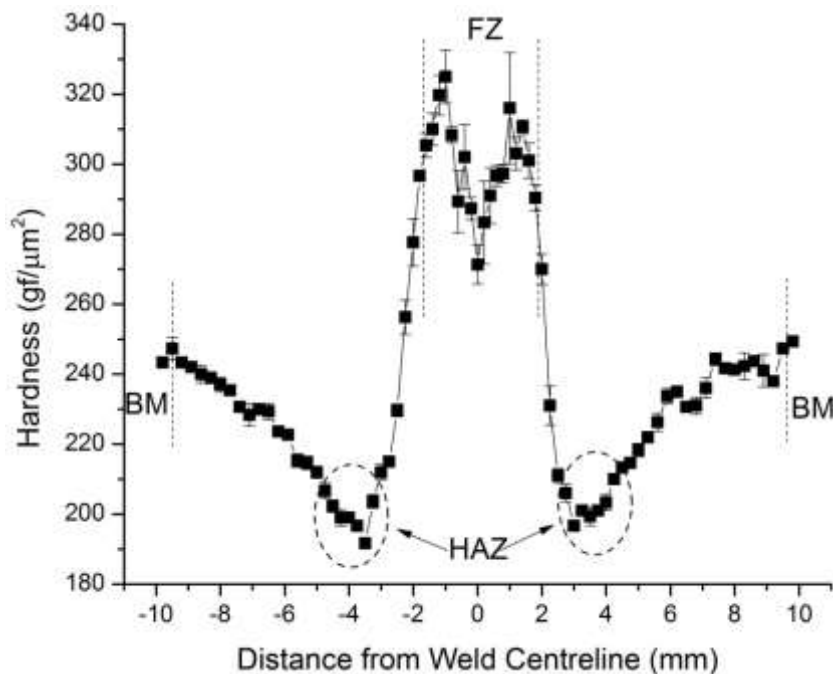


Figure 5.3: Typical microhardness profile of a 4 kW (D) 1.2 weld.

Figure 5.4 shows the hardness profiles of the three diode welds superimposed. From this plot it can be seen that FZ hardness increased with increasing welding speed (i.e. decreasing weld heat input) and also that the

widths of both the fusion and heat-affected zones decreased with increasing welding speed. There was no significant difference in the HAZ softening (difference between base material and minimum HAZ hardness) between the 4kW (D) 0.8 and 4kW (D) 1.0 welds and only a small decrease in the HAZ softening versus the BM for the 4kW (D) 1.2 weld. This hardness decrease is not likely to result in a visible difference in microstructure using optical microscopy.

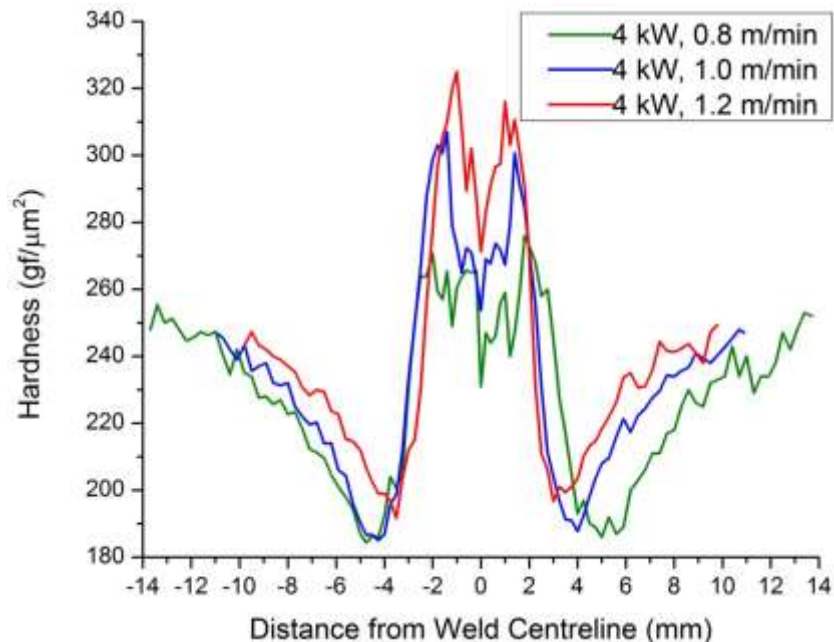


Figure 5.4: Composite plot of microhardness profiles for high heat input diode welds.

5.1.2 Fibre Welds

A typical hardness profile for a 4kW (F) 2 weld is given in Figure 5.5. The softened HAZ was observed adjacent to the fusion zone as with the diode welds; however the contrast in mechanical properties between the BM and the HAZ was not as severe as was observed in the diode welds. The minimum

hardness observed in the HAZ was found to be $199.3 \text{ gf}/\mu\text{m}^2$ (see Table 5.3). It is also seen that the hardness of the FZ ($351.8 \text{ gf}/\mu\text{m}^2$) was further elevated relative to the base material, as compared to the diode welds (see Table 5.2 and Table 5.3). This suggests a larger volume fraction of martensite in the FZ as compared to the diode welds and will likely result in elevated strength as well.

Table 5.3: Summary of fibre weld hardness measurements.

Laser Power (kW)	Welding Speed (m/min)	Average FZ Hardness	Minimum HAZ Hardness	HAZ Softening versus BM
4	2	351.8 ± 7.5	199.3 ± 1.3	50.2 ± 4.1
4	4	388.4 ± 5.4	209 ± 3.1	32.8 ± 6.4
6	2	381.8 ± 4.3	205.7 ± 0.3	41.7 ± 2.7
6	4	397.1 ± 3.9	212 ± 4.5	28.2 ± 7.0

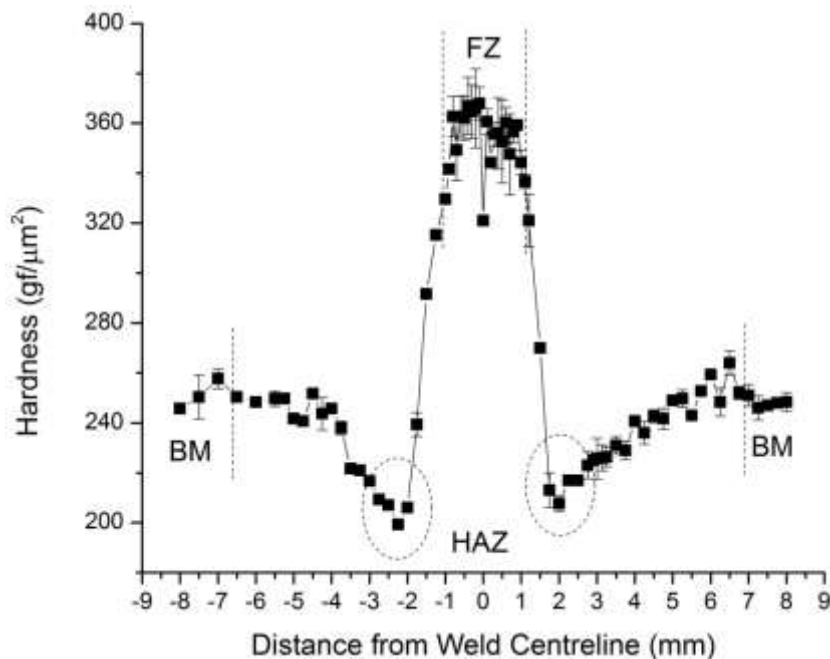


Figure 5.5: Typical hardness profile for a 4kW (F) 2 weld.

Figure 5.6 shows a typical hardness profile for a 4kW (F) 4 weld. It can be seen that the FZ hardness was more uniform and also further elevated (388.4 gf/ μm^2 , see Table 5.3) as compared with the 4kW (F) 2 weld.

A typical hardness profile of a 6kW (F) 2 weld is given in Figure 5.7. It can be seen that the hardness across the FZ was uniform and that the softened HAZ region was once again present. The uniformity, as well as the average hardness value of the FZ (381.8 \pm 4.3, see Table 5.3) suggests that the microstructure was predominately martensite.

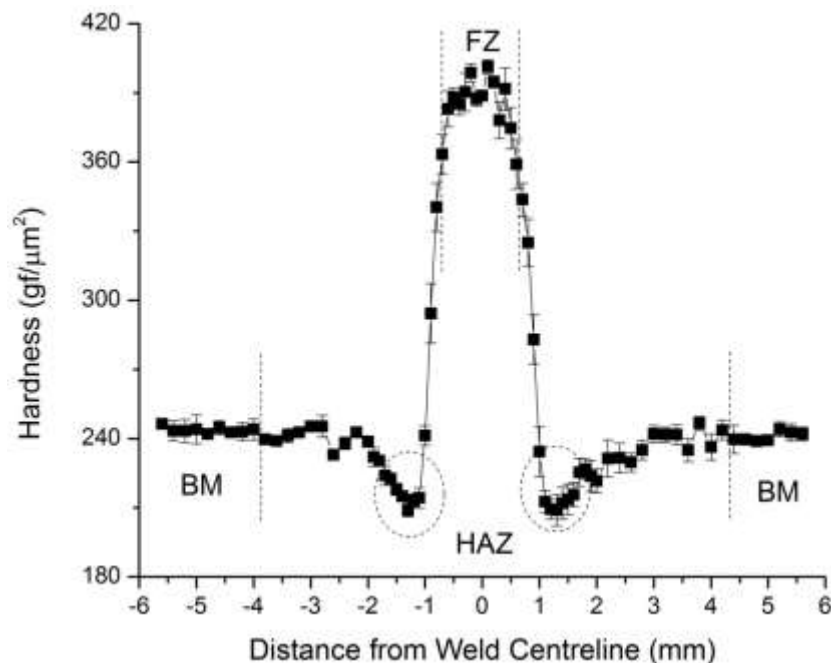


Figure 5.6: Typical hardness profile of a 4kW (F) 4 weld.

Finally, a typical hardness profile for a 6kW (F) 4 weld is presented in Figure 5.8, where a less pronounced softened HAZ region and a quite uniform FZ were observed. The average hardness value of the FZ was 397.1 \pm 3.9 (see Table

5.3), which suggests that the microstructure was predominately martensite and will likely result in the highest strength of all weld FZ.

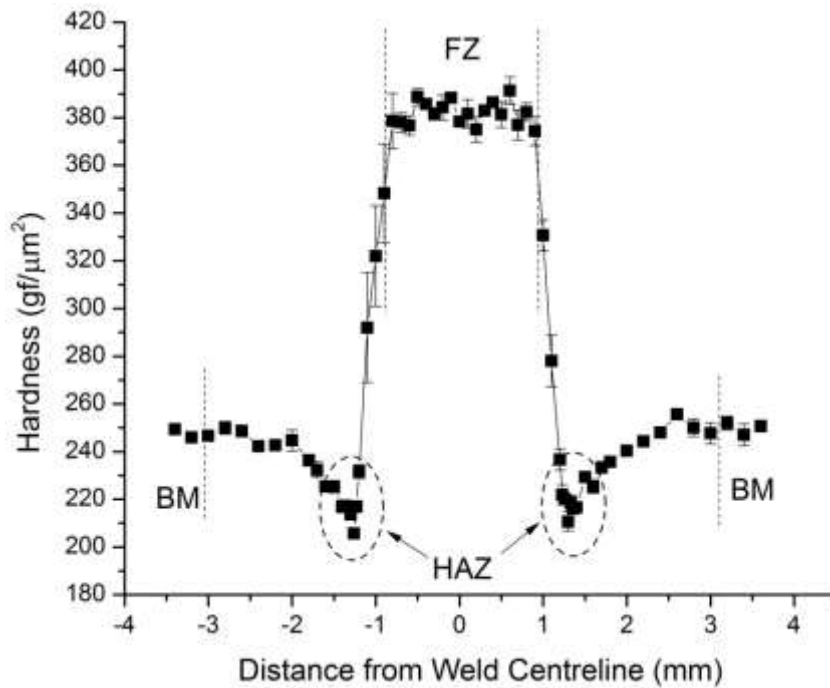


Figure 5.7: Typical microhardness profile of a 6 kW (F) 2 weld.

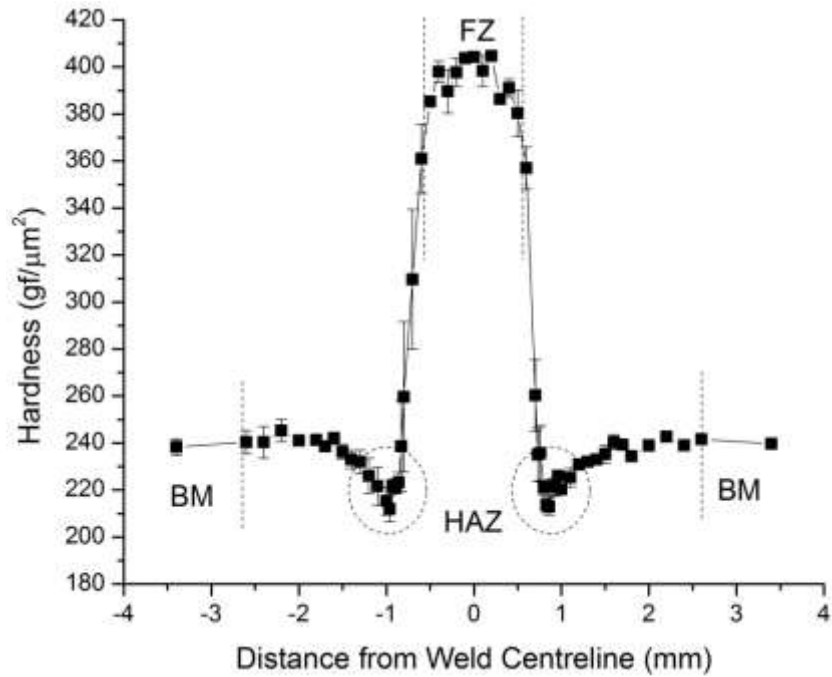


Figure 5.8: Typical microhardness profile of a 6 kW (F) 4 weld.

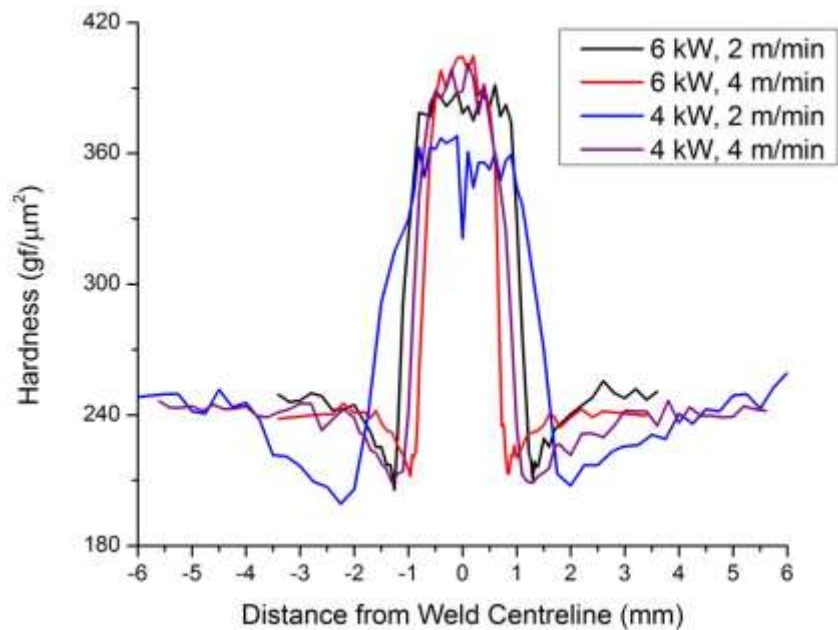


Figure 5.9: Composite plot of microhardness profiles for low heat input fibre welds.

Figure 5.9 shows the hardness profiles of the four fibre welds superimposed. All welds showed a relatively uniform hardness across the FZ which suggests that the microstructures of these zones were predominately martensite with little to no bainitic ferrite. This was expected as with the lower heat input, as compared to the diode welds, the cooling rate within the FZ was higher, which translates to a lower volume fraction of bainitic ferrite per CCT curve behaviour. It can be seen that the hardness and width of the FZ varied with welding speed and power (see Table 5.3). It is also seen that the minimum hardness of each weld varied depending on laser power and welding speed; however this difference in the tempered martensite may still not be visible at the length scales available through optical microscopy. The trend with welding speed was not well defined as the laser power was also varied, the trends for these welds will be further discussed in the next chapter with respect to the heat input of each weld.

5.2 Weldment Microstructures

5.2.1 Diode Welds

Micrographs from the diode weld fusion and heat-affected zones are presented below. The microstructures of the heat-affected zones of for each of the diode welds were indistinguishable from one another at the length scales available to optical microscopy; this was to be expected as comparable hardness values

were reported for the welding speeds listed in Table 5.2. As such, the microstructure of the 4 kW (D) 0.8 weld is presented in Figure 5.10 as being typical of all diode welds (see APPENDIX A for other weld microstructures). It can be seen that the formerly island martensitic microstructure of the base material (see Figure 4.1) was no longer present in the HAZ of the diode welds and instead tempered martensite within a ferritic matrix was observed.

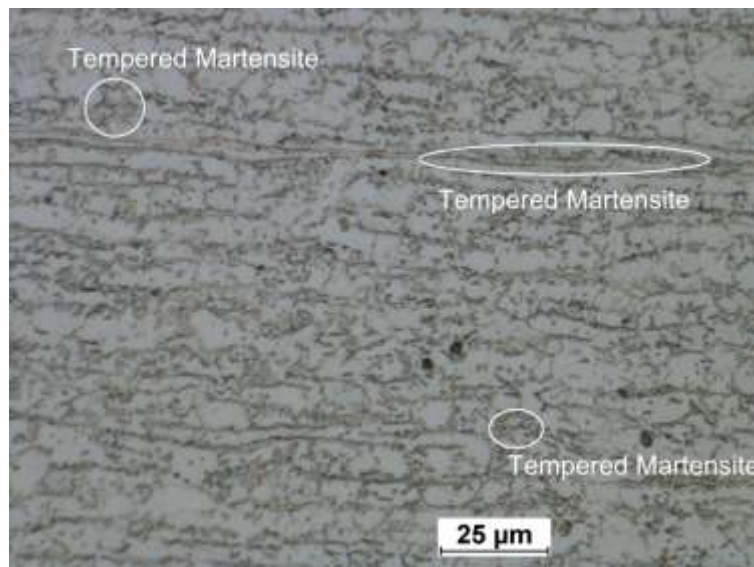


Figure 5.10: 4 kW, 0.8 m/min diode weld HAZ microstructure.

While each of the diode welds fusion zones present microstructures which were significantly different from the base material, there were differences which can account for the variations in hardness observed as a function of welding speed in Table 5.2. The FZ microstructure of a 4 kW (D) 0.8 weld is shown in Figure 5.11(a), where martensite as well as bainitic ferrite can be observed. The variety of microstructural features observed within the fusion zone can explain the variations in hardness observed across this weld's fusion zone.

A similar microstructure was observed in the fusion zone of a 4 kW (D) 1.0 weld (Figure 5.11(b); however, there appeared to be more martensite and less bainite than in the 4kW (D) 0.8 weld (see Figure 5.11(a)). This increase in martensite content is consistent with the observed increase in average hardness value across the fusion zone, reported in Table 5.2. This is also to be expected as the higher welding speed of the 4kW (D) 1.0 weld (lower heat input) resulted in higher cooling rates in the FZ as well; this translates to a lower volume fraction of bainitic ferrite per CCT curve behaviour (see Figure 5.12).

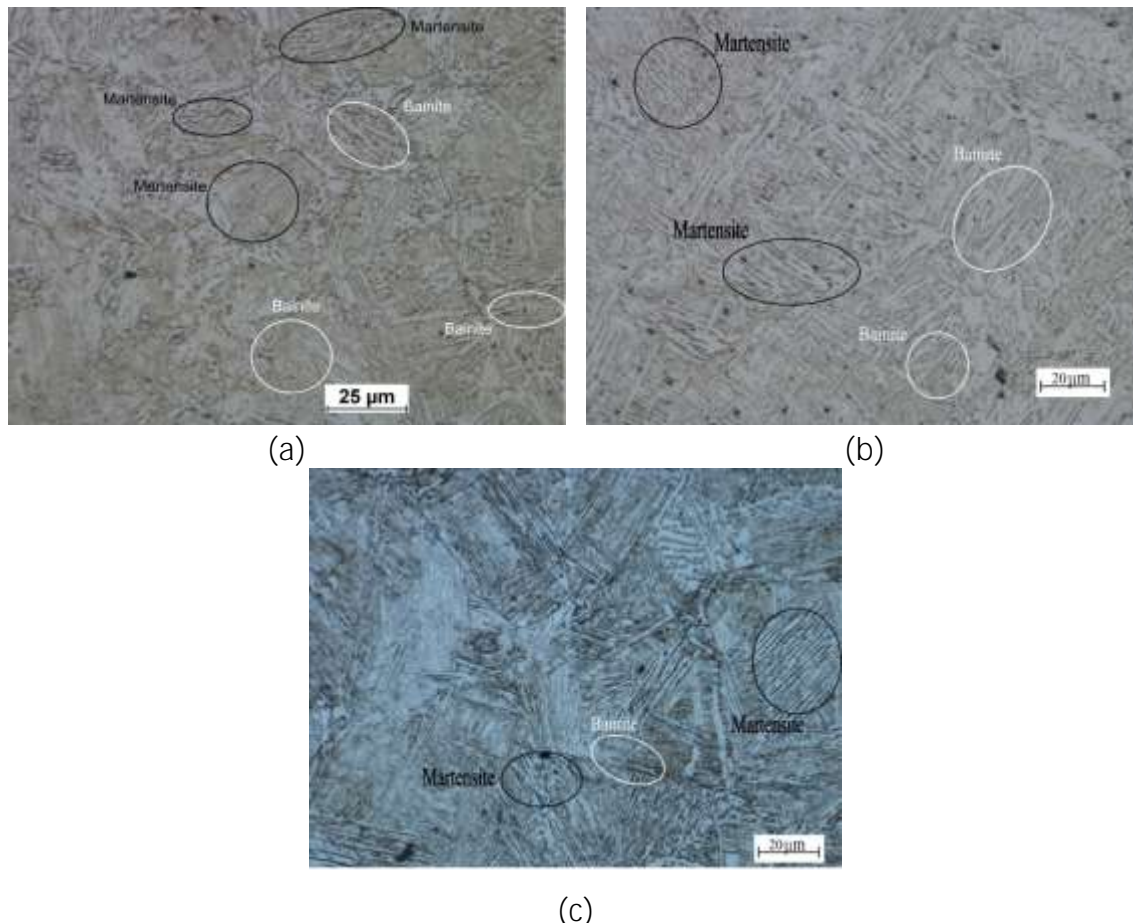


Figure 5.11: FZ microstructure of (a) 4kW (D) 0.8 weld (b) 4kW (D) 1.0 weld and (c) 4kW (D) 1.2 weld.

Finally, the microstructure of a 4 kW (D) 1.2 weld FZ is presented in Figure 5.11(c). Significantly more martensite was observed in this microstructure versus the 4 kW (D) 0.8 and 4 kW (D) 1.0 welds; however a small fraction of bainitic ferrite was still present. This is again consistent with the increased welding speed (decreased heat input) resulting in a higher cooling rate within the FZ and thus only a small amount of bainitic ferrite was produced. The microstructures observed in these diode welds was not consistent with the microstructures predicted by the CCT curves in Figure 5.12.

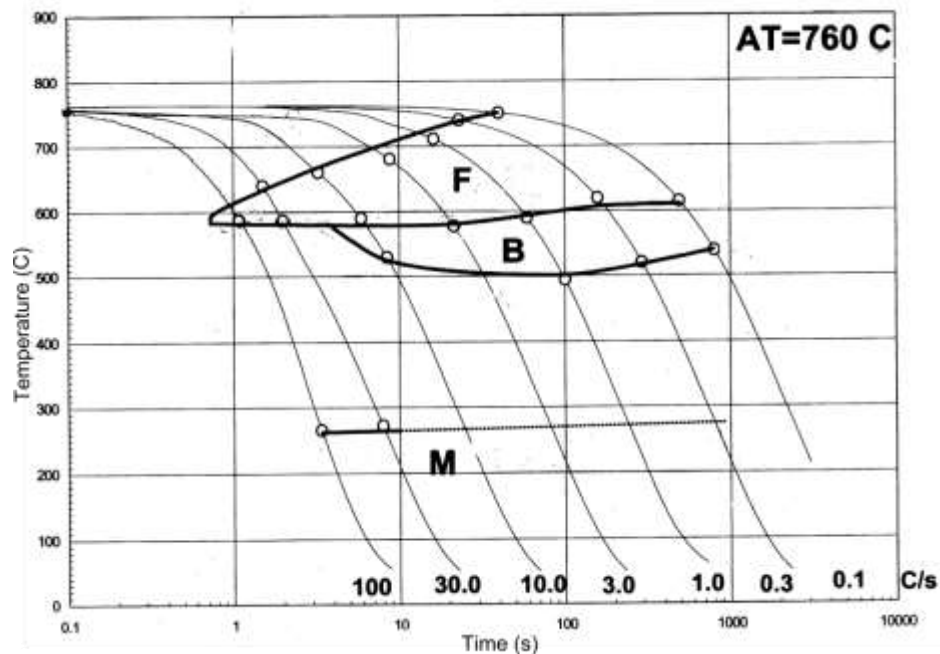


Figure 5.12: CCT curve for DP780 steel with cooling curves superimposed [37].

5.2.2 Fibre Welds

The microstructures of all fibre weld heat-affected zones are presented in Figure 5.13. Tempered martensite was observed in all cases; however there tended to be more untempered martensite with increasing weld speed for a given laser power. This is consistent with the hardness values reported in Table 5.3 and with the variations in widths of the HAZ microstructural zone as seen in Figure 5.5 - Figure 5.8.

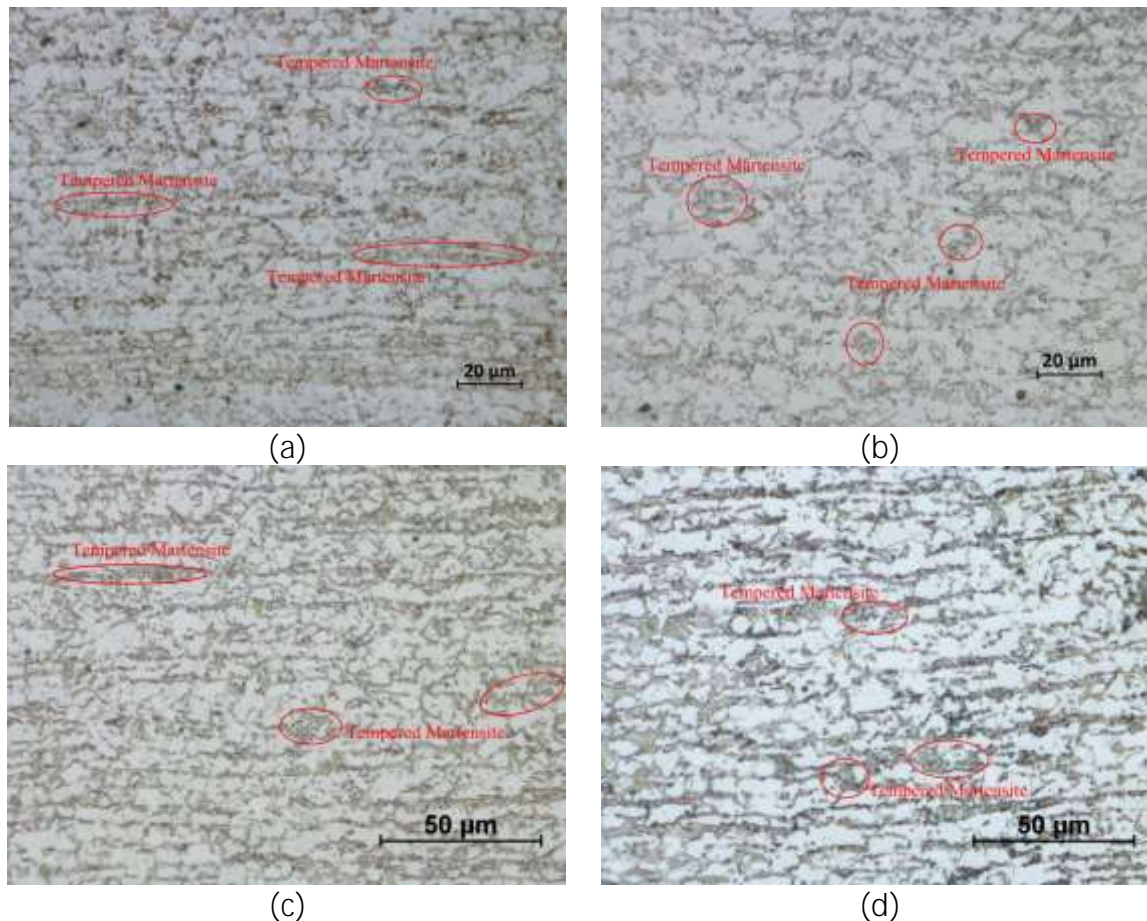


Figure 5.13: HAZ microstructures of (a) 4 kW (F) 2 weld (b) 4 kW (F) 4 weld (c) 6 kW (F) 2 weld and (d) 6 kW (F) 4 weld.

The microstructures of all fibre weld FZ are presented in Figure 5.14. All weld FZ consisted of a martensitic structure with no significant bainitic ferrite being observed. This was likely due to the increased cooling rates of these welds as compared to the diode welds, which resulted in reduced bainitic ferrite transformation per the CCT curve behavior (see Figure 5.12).

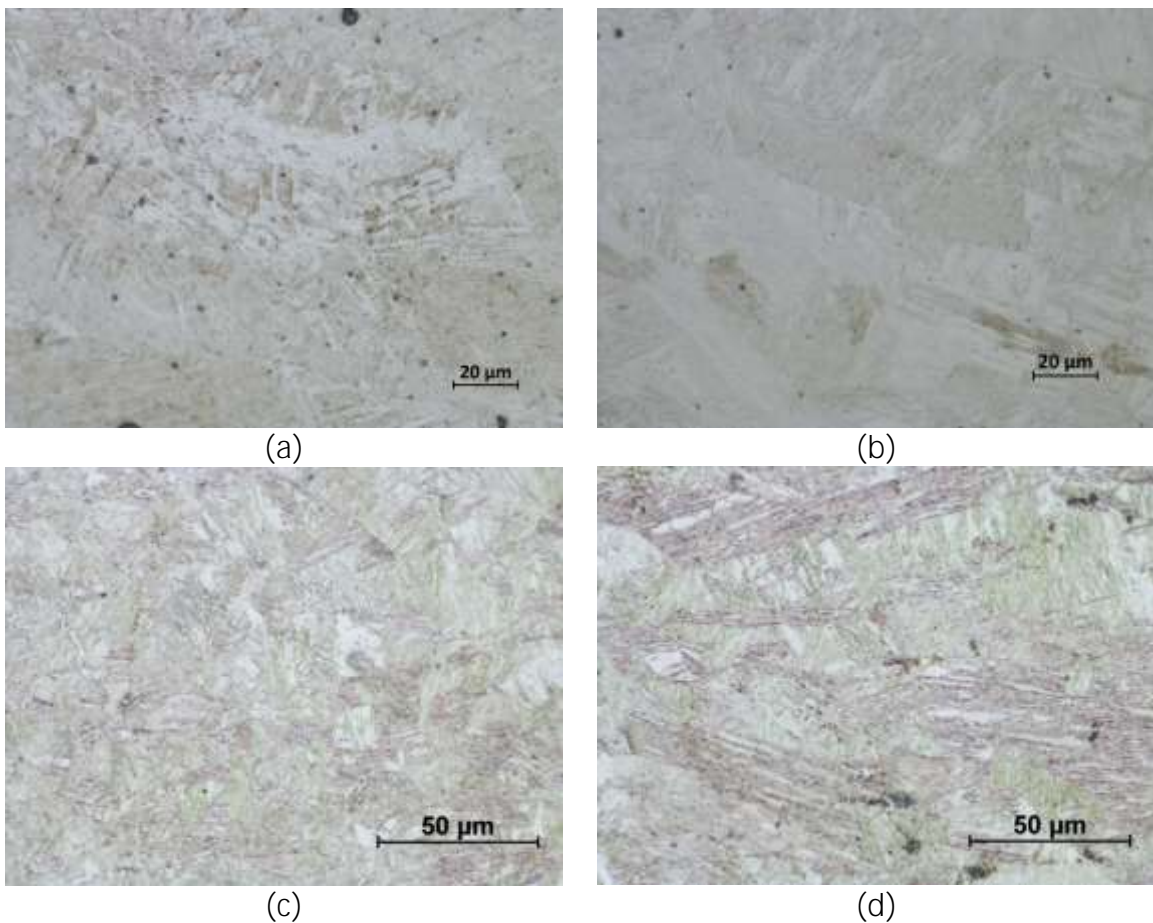


Figure 5.14: FZ microstructures of (a) 4 kW (F) 2 weld (b) 4 kW (F) 4 weld (c) 6kW (F) 2 weld and (d) 6kW (F) 4 weld.

5.3 Mechanical Testing

5.3.1 Base Material

The effective stress – effective strain tensile curves for the base material for all testing geometries described in CHAPTER 4 (see Figure 4.3, Figure 4.4, and Figure 4.5) are shown in Figure 5.15. Triplicates of each test geometry were performed and representative curves are presented. It can be seen that the miniature tensile and ASTM standard sub-size samples produced effective stress – effective strain curves which were insignificantly different from one another. The plane strain curves were also comparable to the ASTM curves; however, slight differences in yield strength and elongation were observed. The differences in elongation were due to the well-established effect of differences in strain path [63]. For example, it is well known that the failure strains in plane strain are lower than those for uniaxial tension when forming reasonable isotropic metallic materials.

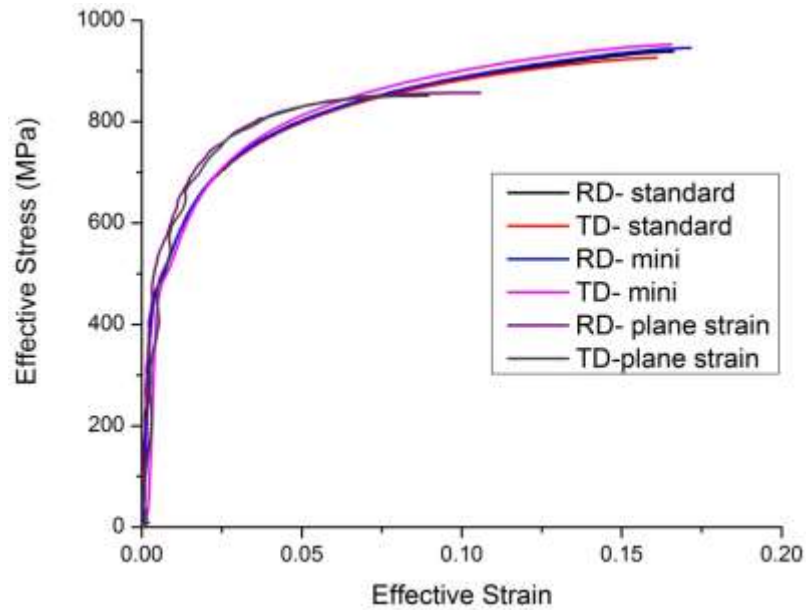


Figure 5.15: Base material effective stress - effective strain curves as a function of sample geometry and strain path.

The yield strength and UTS measured for each of the testing geometries are plotted in Figure 5.16. From this figure, it can be seen that both the yield strength and UTS were insignificantly different across all three testing geometries. There were no significant differences observed between the yield strength and the UTS in the rolling and transverse direction (RD and TD respectively), indicating that the base material exhibited isotropic behaviour.

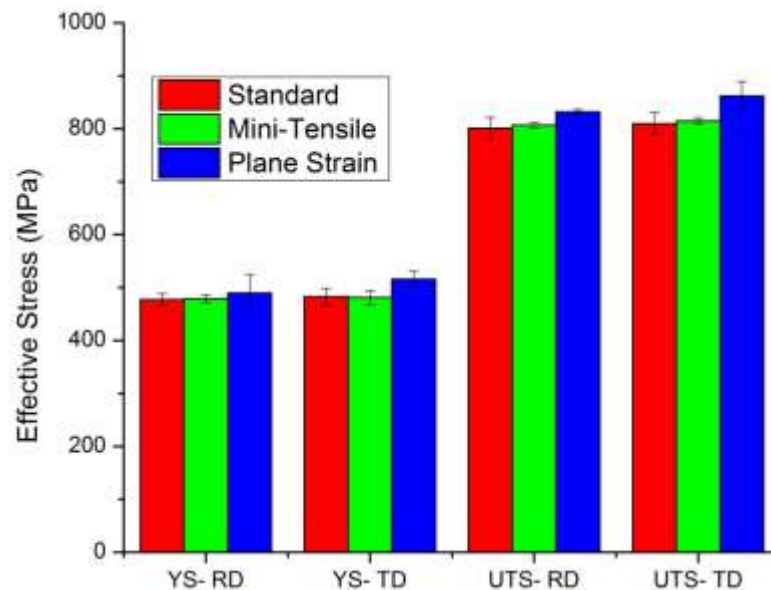


Figure 5.16: Yield strength and UTS measured from all BM testing geometries in both the rolling (RD) and transverse (TD) directions.

5.3.2 Across Weld Tensile Testing

The results of the ASTM standard samples pulled with the weld bead centered in the gauge and the welding direction perpendicular to the tensile direction are presented in the following section. Strain maps immediately before fracture as well as a plot of section length versus strain for the 4 kW (D) 0.8 weld are shown in Figure 5.17. These plots are representative of all of the diode welds; the strain maps of the 4kW (D) 1.0 and 4kW (D) 1.2 welds can be seen in APPENDIX C. For all strain maps presented, red indicates regions of high strain while dark blue are regions of low strain. Figure 5.17 shows that two necks formed (the red/orange and green region), which grew until one neck prevailed. The fatal neck was located in the orange/red region of Figure 5.17. For all experimental diode weld speeds, these necks, and ultimately the location of

failure, were within the HAZ. This is consistent with the relatively low hardness values versus the other microstructural zones observed (see Figure 5.4). It can also be seen that the strain was very low within the fusion zone in all cases, consistent with the high hardness values observed in this microstructural zone (see Figure 5.4).

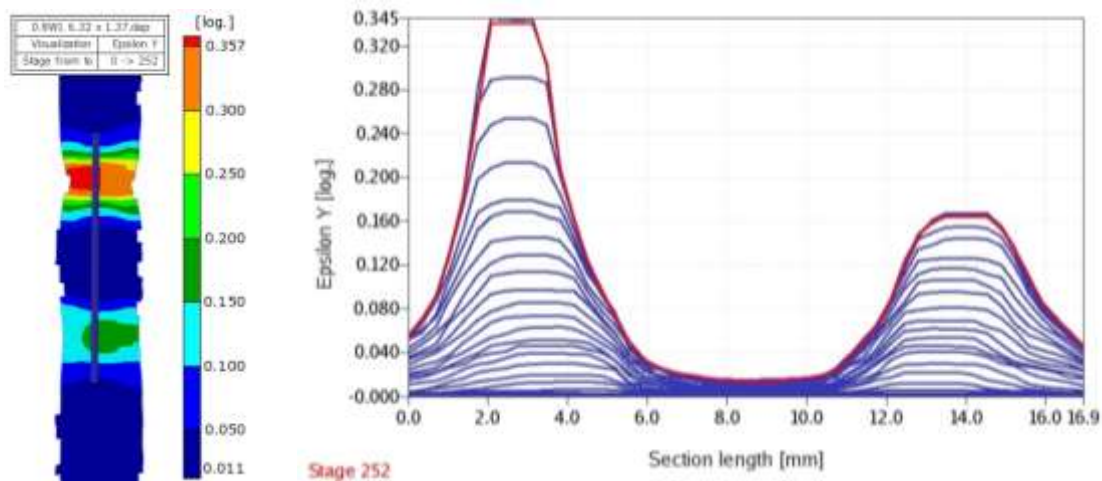


Figure 5.17: Strain map and strain versus section length plot for a 4kW (D) 0.8 weld.

Strain maps immediately before fracture as well as a plot of section length versus strain for the 4 kW (F) 2 weld are shown in Figure 5.18. A similar phenomenon as with the diode welds was observed for the 4 kW (D) 0.8 weld, where two necks form (red and green regions) and grew with ultimately one neck (red region) being the location of fracture. In this case, the necks and fracture location occurred within the BM just adjacent to the HAZ. This behaviour was also observed for the 4 kW (F) 4 and 6 kW (F) 2 welds (see APPENDIX C). The fracture localization within the BM was likely due to a less significant mechanical property contrast across the BM and the HAZ (see Table 5.3).

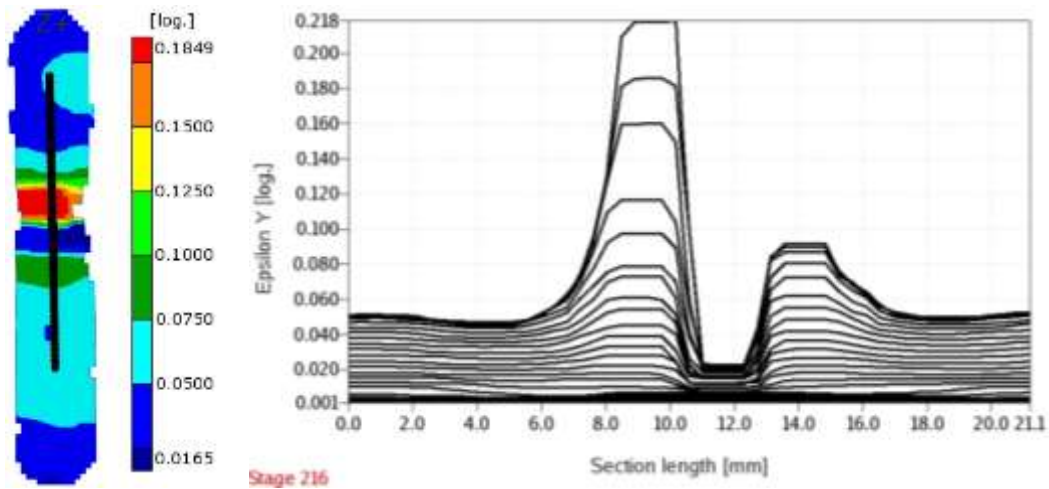


Figure 5.18: Strain map and strain versus section length plot for a 4kW (F) 2 weld.

Strain maps immediately before fracture as well as a plot of section length versus strain for the 6 kW (F) 4 weld are shown in Figure 5.19. In this case, a single neck was formed and the location of fracture was well within the BM, not the HAZ. This is likely because the width of the softened HAZ region was very small as compared to the other microstructural zones and the contrast in mechanical properties was not as severe as with the other welds (see Table 5.3). The reduced area and less significant difference between the BM and HAZ properties did not constrain the HAZ as severely from the BM side which ultimately resulted in fracture of the BM.

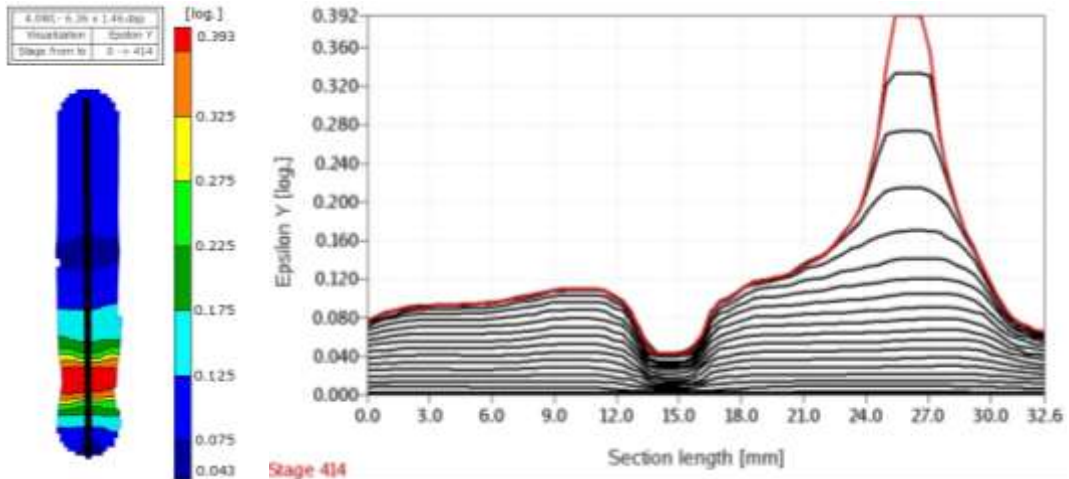


Figure 5.19: Strain map and strain versus section length plot for a 6kW (F) 4 weld.

5.3.3 Specialized Geometries - Diode Welds

For each of the specialized geometries, five tensile samples were tested; in each case a representative effective stress – effective strain curve is shown. The effective stress – effective strain curves for a 4 kW (D) 0.8 weld for all testing geometries are presented in Figure 5.20. It can be seen that the yield strength and UTS for both the heat-affected and fusion zones were depressed compared to the base material values (see Figure 5.15 and Figure 5.16). The HAZ exhibited lower UTS and yield strength as compared to the FZ; however, the uniform elongation was significantly larger for the HAZ as compared to the FZ.

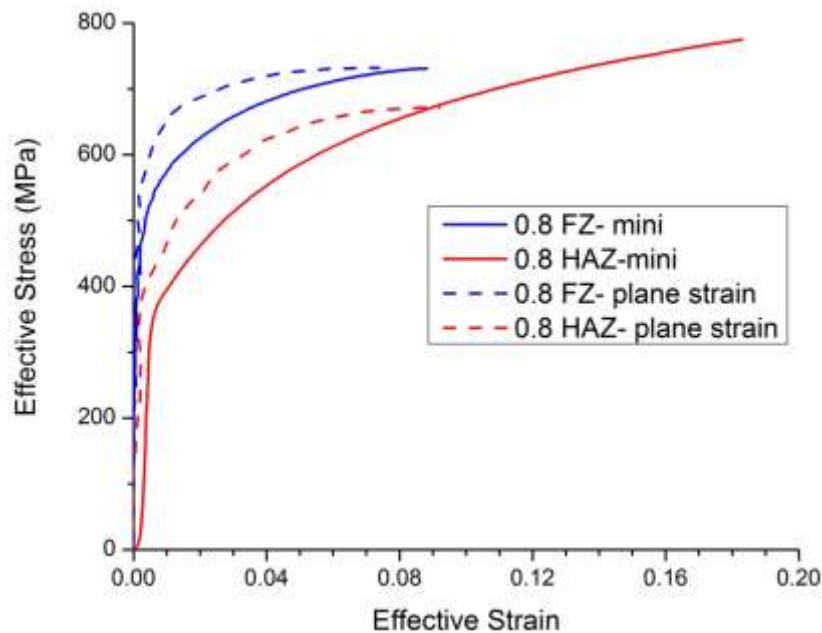


Figure 5.20: Effective stress - effective strain curves for a 4kW (D) 0.8 weld.

The effective stress – effective strain curves for a 4 kW (D) 1.0 weld for all testing geometries are presented in Figure 5.21. It can be seen that the yield strength and UTS for the HAZ were depressed as compared to the base material values (see Figure 5.15 and Figure 5.16). The UTS of the FZ was also observed to be lower than the base material value. The FZ yield strength, however, was elevated as compared to the base material. There was also very good correlation between the curves produced from the miniature tensile samples and the plane strain samples in the case of both the fusion and heat-affected zones.

The effective stress – effective strain curves for a 4 kW (D) 1.2 weld for all testing geometries are presented in Figure 5.22. It can be seen that the UTS for the HAZ was depressed compared to the base material values (see Figure 5.15 and Figure 5.16). The yield strength of the heat-affected zone as well as the UTS

of the fusion zone were, in this case, comparable to that of the base material. It can also be seen that for the fusion zone, the yield strength was further elevated versus the base material.

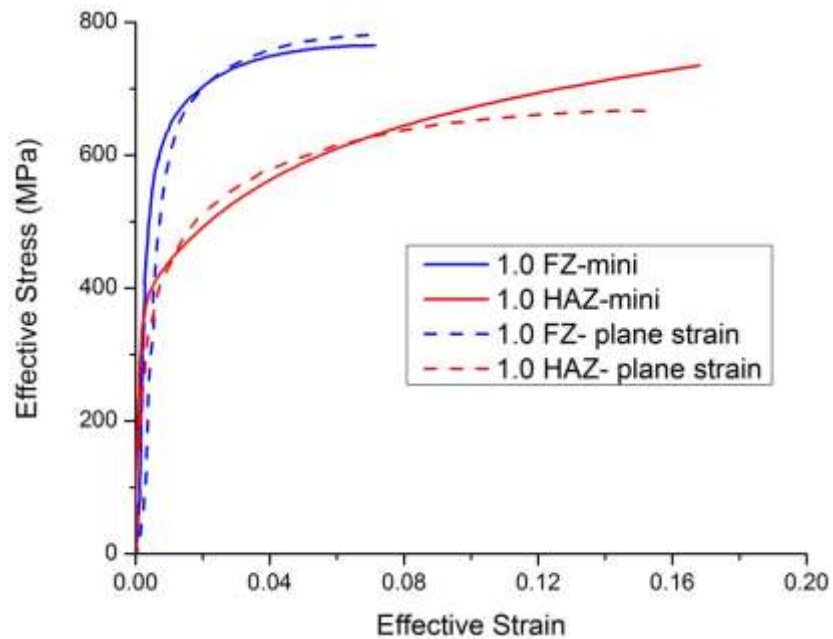


Figure 5.21: Effective stress - effective strain curves for a 4kW (D) 1.0 weld.

The changes in the mechanical properties for each of the weld zones with changing welding speeds is summarized in Figure 5.23 and Figure 5.24 for the fusion zones and heat-affected zones, respectively, with reference data for the base material included. It can be seen that for the FZ, the general trend with increasing welding speed (decreasing heat input) was towards recovery of the UTS relative to that of the base material, while the yield strength continued to increase as compared to the base material. This trend is consistent with the hardness measurements of each of the welds. From Figure 5.4 and Table 5.2 it can be seen that with increasing welding speed (or decreasing heat input) the

fusion zone hardness increased. Figure 5.11, shows that this trend is also consistent with the observed FZ microstructures, where with increasing welding speed (decreasing heat input) the volume fraction of martensite tended to increase. From Figure 5.23, it can also be seen that there was no significant difference between the yield strength or the UTS of the fusion zone at higher welding speeds (lower heat input) which is not consistent with the hardness data in Table 5.2, where there was a significant difference in average hardness across the fusion zones of those two welding conditions. It is also observed in Figure 5.23 that the UTS of the fusion zone was completely recovered to the base material value at the highest welding speeds (lowest heat input).

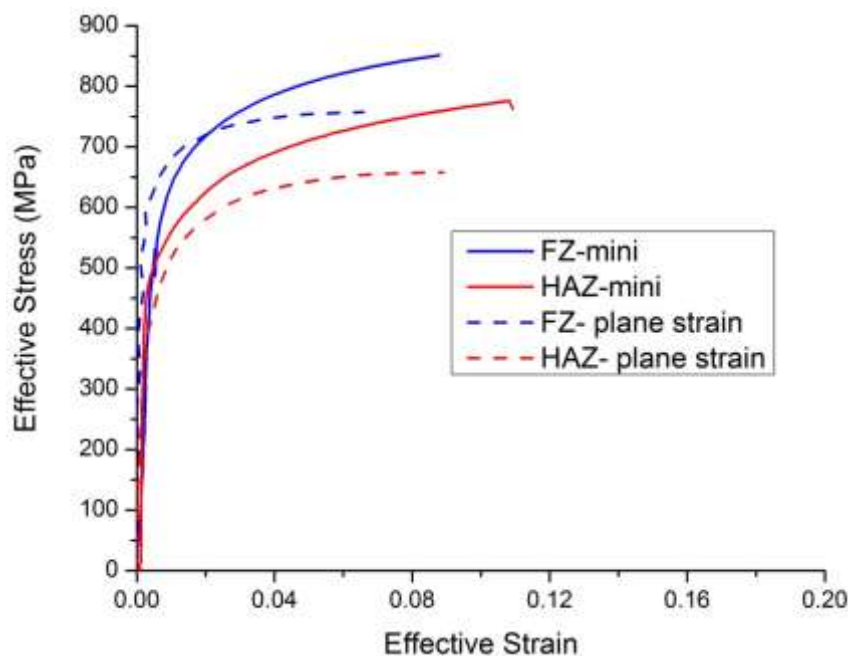


Figure 5.22: Effective stress - effective strain curves for a 4kW (D) 1.2 weld.

For the heat-affected zones, it can be seen that the yield strength tended to recover towards the base material value with increasing welding speed (decreasing heat input) and while the UTS also increased with increasing welding speed, it did not recover to the base material properties in the tested welding conditions. There was also no significant difference observed in Figure 5.24 between the yield strength and the UTS of the HAZ for the lowest two welding speeds (higher heat input). This is consistent with the hardness data reported in Table 5.2, where there was no significant difference in the minimum hardness values for these two welding conditions. It is also observed in Figure 5.24 that the yield strength of the HAZ was completely recovered to the base material value for the highest welding speed (lowest heat input).

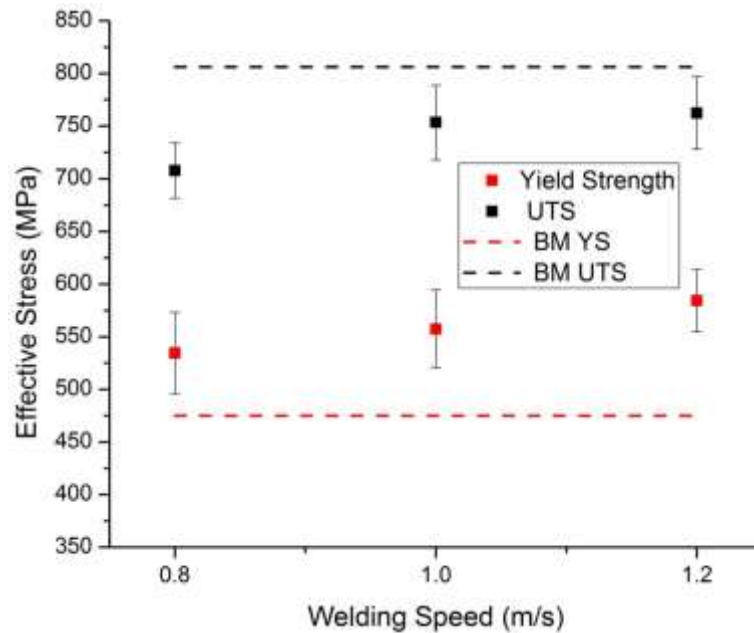


Figure 5.23: Comparison of mechanical properties for the diode weld fusion zones versus the base material (BM).

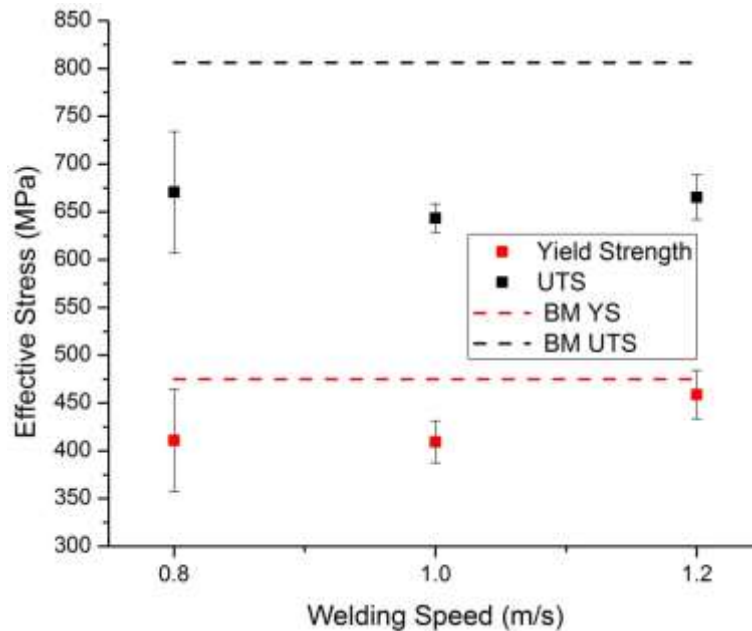


Figure 5.24: Comparison of mechanical properties for the diode weld heat-affected zones versus the BM.

5.3.4 Specialized Geometries - Fibre Welds

The effective stress – effective strain curves for a 4 kW (F) 2 and a 4 kW (F) 4 weld are presented in Figure 5.25. It can be seen that for both welds that the FZ had a higher UTS and yield strength than the HAZ (see Table 5.4 for values.) It is also seen that both the UTS and yield strength for both welds and both microstructural zones were elevated as compared to the base material values (see Figure 5.15 and Figure 5.16.) This was expected for the FZ where both the hardness values (see Table 5.3) and the microstructure (see Figure 5.14) suggest that it was stronger than the base material. The HAZ, however demonstrated a lower hardness value (see Table 5.3) and a tempered martensite microstructure (see Figure 5.13) which would suggest depressed strength compared to the base

material. It can also be seen in Figure 5.25 that the faster welding speed (lower heat input) weld at the same laser power resulted in a high UTS and yield strength.

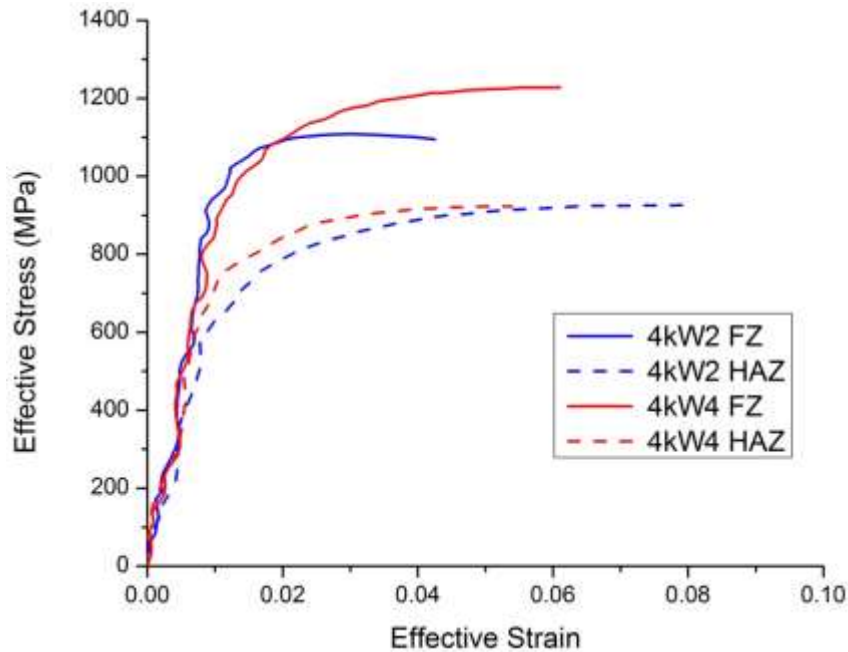


Figure 5.25: Effective stress – effective strain curves for a 4 kW (F) 2 and a 4 kW (F) 4 weld.

Table 5.4: Summary of fibre weld mechanical properties.

		4 kW (F) 2	4 kW (F) 4	6 kW (F) 2	6 kW (F) 4
FZ	UTS (MPa)	1139 ± 119	1247 ± 130	1248 ± 33	1222 ± 21
	YS (MPa)	995 ± 57	995 ± 59	963 ± 38	930 ± 86
HAZ	UTS (MPa)	949 ± 53	925 ± 40	1077 ± 8.6	976 ± 97
	YS (MPa)	678 ± 49	731 ± 20	763 ± 46	669 ± 94

The effective stress – effective strain curves for a 6 kW (F) 2 and 6 kW (F) 4 weld are presented in Figure 5.26. A similar trend to the 4 kW (F) welds was observed in this case with the FZ exhibiting higher UTS and yield strength

than the HAZ in both cases (see Table 5.4 for values.) As well, the HAZ exhibited higher strength than would be predicted from the hardness values (see Table 5.3) and microstructure (see Figure 5.13.) The 6 kW (F) welds showed that with higher welding speed (lower heat input) the UTS and yield strength of both microstructural zones decreased.

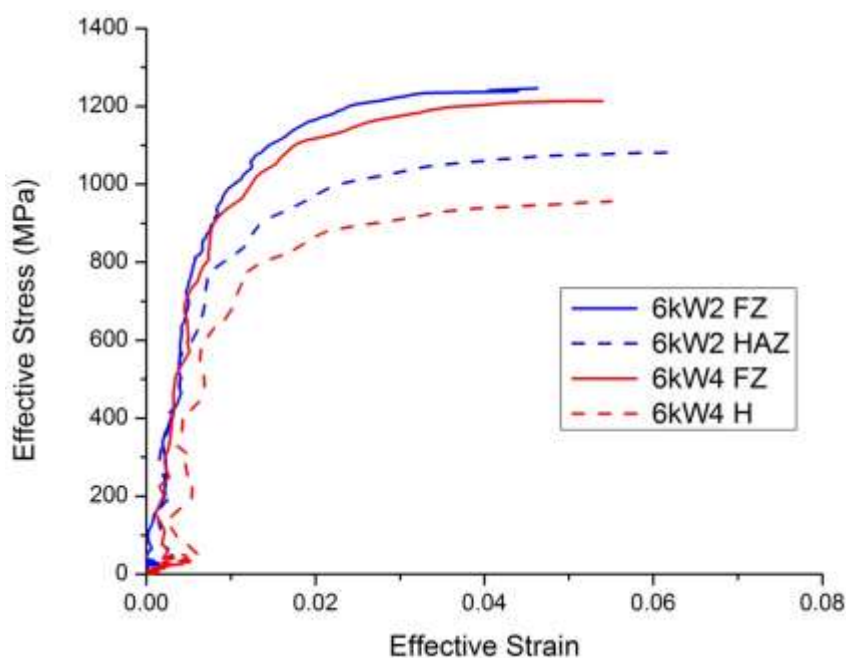


Figure 5.26: Effective stress - effective strain curves for a 6 kW (F) 2 and a 6 kW (F) 4 weld.

5.4 Results Summary

This study examined the microstructure, microhardness and mechanical properties of a variety of fibre (low heat input) and diode (high heat input) laser welds. The fibre (lower heat input) welds exhibited higher FZ hardness and pure martensitic FZ microstructure while the diode (lower heat input) welds showed

FZ microstructures consisting of both martensite and bainitic ferrite with lower hardness values being reported as compared to the fibre welds. This is consistent with the weld bead (FZ) size and the width of the HAZ which were narrower in the case of the fibre welds as compared to the diode welds due to smaller beam geometry and lower heat input. Mechanical testing showed that the fusion zones of the diode welds (high heat input) had lower UTS and yield strength than base material values, while the fibre weld fusion zones exhibited UTS and yield strengths which were significantly elevated when compared to the base material. The HAZ of all experimental welds presented a tempered martensite microstructure and a drop in hardness relative to the base material. The minimum hardness observed was dependent on the welding speed as well as the laser power, this will be further discussed in the next chapter. Mechanical testing of the HAZ showed a depression in yield strength and UTS for the diode (high heat input) welds while these properties were significantly increased in the fibre weld (low heat input) cases. Finally, across weld tensile testing showed that all diode welded samples failed within the HAZ while all fibre welded samples failed within the base material. All of the above results and trends will be discussed in the following chapter.

CHAPTER 6 Discussion

6.1 Heat Input Normalization

In order to properly compare all welds regardless of the type of laser, laser power or welding speed it is necessary to normalize the welds based on heat input. The normalization technique used was developed by Xia et al. [13] and is discussed in detail in Chapters 2.2.1 and 4.3.2. The heat input and time constants were calculated using Equations (4.1) and (4.2), respectively, and the results are shown in Table 6.1 (see APPENDIX D for detailed calculations). It is seen that the highest heat input weld was the 4 kW (D) weld and with increasing welding speeds for a given laser power and type the heat input decreased.

Table 6.1: Heat input and time constants for all welding conditions.

Speed (m/min)	0.8	1.0	1.2	2	4	2	4
Laser Power	4 kW	6 kW	6 kW				
Laser Type	D	D	D	F	F	F	F
Heat Input (J/mm ²)	84.8	62.2	59.4	36.8	12.4	15.0	11.0
Time Constant (s)	2.77	1.50	1.36	0.52	0.06	0.09	0.05

HAZ softening, defined as the difference in hardness between the BM and the minimum HAZ hardness value, is plotted versus heat input for all experimental welds in Figure 6.1. It is seen that all samples, regardless of laser type or power, fell onto a single line with an R^2 value of 0.92, indicating a good linear correlation between heat input and softening of the HAZ. It was difficult

to compare the data plotted in this manner to the published literature as most authors plot HAZ softening or hardness versus the time constant. As such, Figure 6.2 shows the minimum HAZ hardness and Figure 6.3 the HAZ softening plotted against the time constant for data from the present study as well as data from Biro et al. [5] for a similar DP780 steel. The behaviour can be described as a sigmoidal decay with respect to the time constant and if higher time constant samples were examined the true value of the lower plateau would be evident in both cases. These curves are consistent with what has been reported in the literature for similar steels [4], [13], [38]. While the hardness values reported by Biro et al [4] were consistently higher than those reported in the present study for the same time constant, the trends observed are consistent across both data sets. The difference in reported hardness values can be attributed to different hardness testing machines used. As the diamond indenter ages, the size of the indent in the same material will become smaller due to wear of the indenter resulting in the reporting of a higher hardness value. This upward bias in hardness is consistent with the values reported in Figure 6.2.

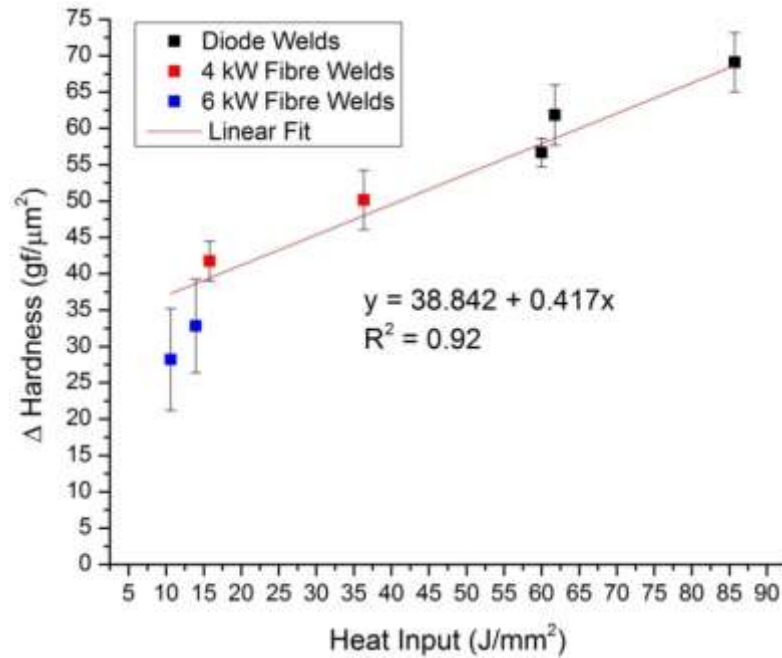


Figure 6.1: Delta hardness (difference in hardness from the BM to the minimum HAZ value) versus heat input.

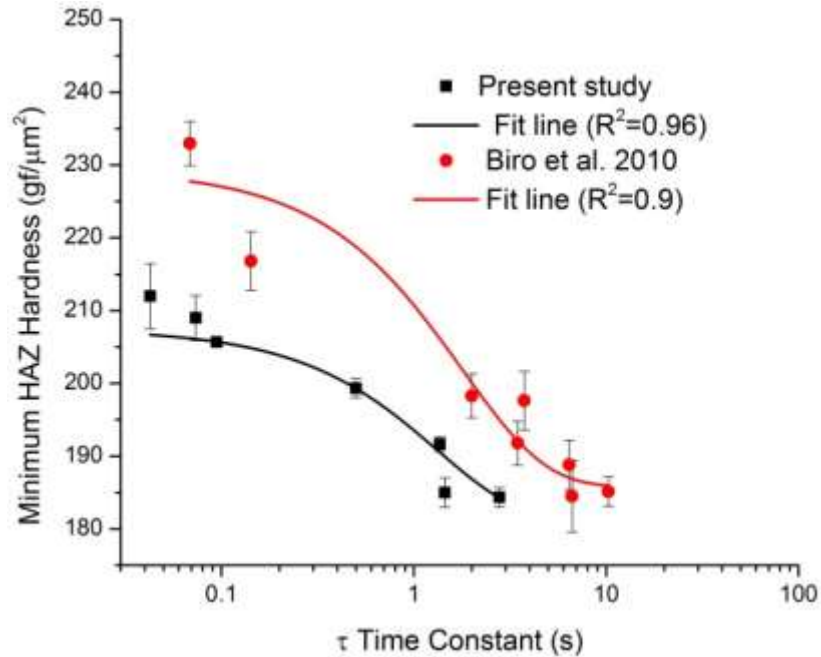


Figure 6.2: HAZ minimum hardness versus time constant for present study and data from Biro et al. [4].

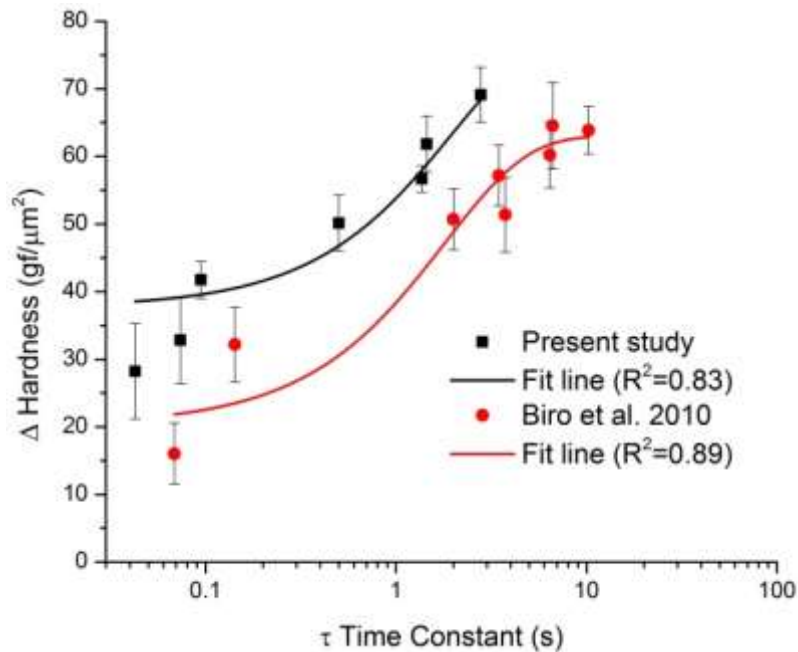


Figure 6.3: HAZ softening versus time constant for present study and data from Biro et al. [4].

6.2 Cooling Rates and the Fusion Zone

After normalizing the welding parameters using heat input in section 6.1, the yield strength and UTS of the FZ were plotted against heat input. These values for the diode welds are plotted in Figure 6.4. It is seen that the UTS was depressed compared to the BM value while the yield strength was higher than BM values in all cases.

The UTS and yield strength values for the fibre welds are plotted versus heat input in Figure 6.5. It can be seen that both the UTS and the yield strength are higher than the base material values for all experimental fibre welding conditions. It is also seen that there was no significant effect of heat input on the the yield strength and the UTS for all heat inputs tested.

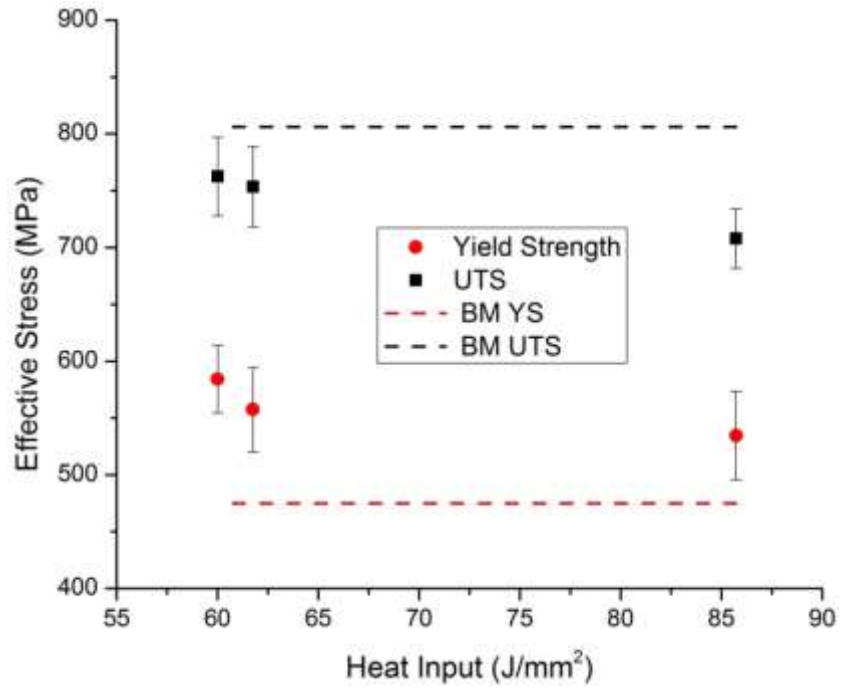


Figure 6.4: Stress versus heat input for the diode weld fusion zones.

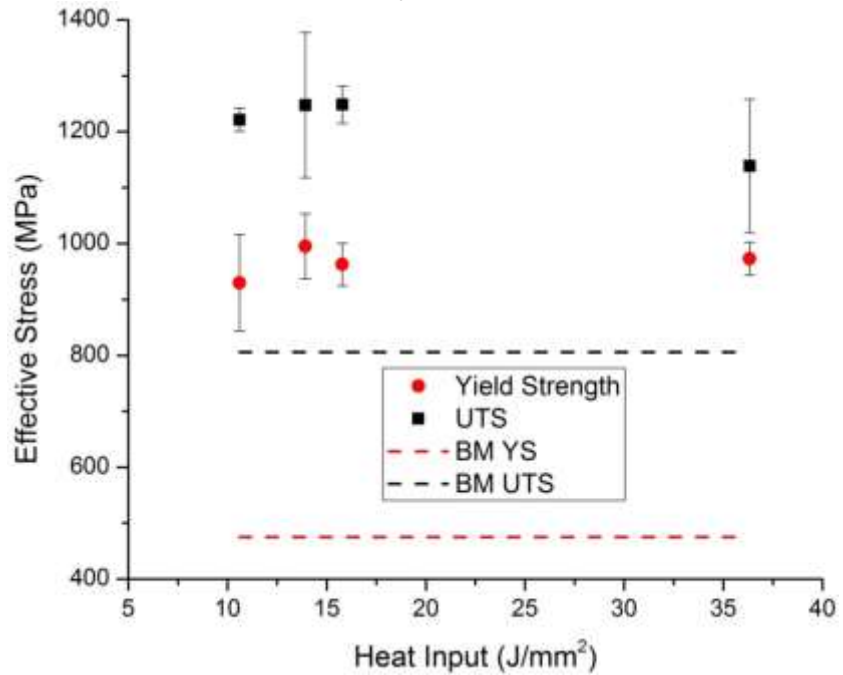


Figure 6.5: Stress versus heat input for fibre weld fusion zones.

To compare the FZ of all experimental welds, the UTS and yield strengths were plotted versus heat input as shown in Figure 6.6. It is seen that in both

cases, the stress behaviour showed a sigmoidal decay with respect to heat input with good fit in both cases (adjusted $R^2=0.99$ for both data sets). This sharp change in mechanical properties above a certain heat input can be explained by the formation (or lack thereof) of bainitic ferrite within the FZ. With increasing heat input there was a decrease in the cooling rate within the fusion zone. There would also be a larger gradient of cooling rates as the fusion zone was physically wider in the higher heat input welds. The kinetics of bainite formation were discussed in detail in section 2.4. With the increased cooling rates it was possible to miss the bainite nose on a CCT curve (see Figure 5.12), resulting in a purely martensitic microstructure as was observed in the fusion zone of all fibre welds (see Figure 5.14) which have lower heat input. The higher heat input diode welds demonstrated microstructures of mixed bainitic ferrite and martensite (see Figure 5.11) and from the microhardness profiles (see Figure 5.4) there was a variation in hardness across the fusion zone. This is consistent with the higher heat input welds having lower cooling rates within the fusion zone, resulting in a mixture of bainite and martensite, with the lowest cooling rate being along the centreline and the rates increasing towards the outer edges of the fusion zone, allowing a larger fraction of bainite to form near the centreline resulting in lower hardness values. The observed microstructures were however not consistent with the CCT curves for this steel (see Figure 5.12). This is also observed in the UTS and yield strength of the fusion zones, where the low heat input welds exhibited values which were elevated compared to the base material and past a critical heat input,

the UTS and yield strength dropped to values near or just below the BM mechanical properties (see Figure 6.6).

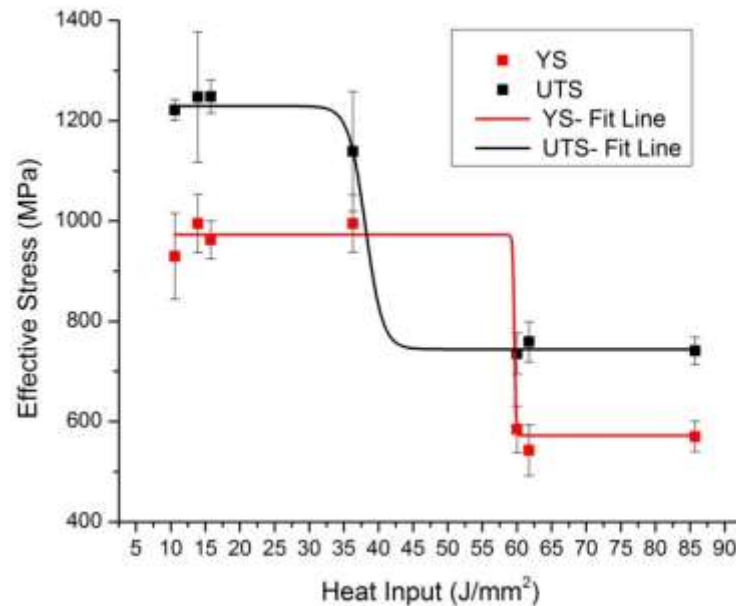


Figure 6.6: Stress versus heat input for all experimental weld fusion zones.

6.3 Thermal Activation of HAZ Martensite Tempering

The diode weld UTS and yield strengths were plotted versus heat input and are shown in Figure 6.7. It can be seen that the UTS was significantly depressed compared to the BM values. The yield strength, however was slightly depressed and, with error and especially in the lowest heat input case, the values are comparable to those of the BM.

The yield strength and UTS for all fibre welds are plotted against heat input in Figure 6.8. It can be seen that for all fibre welds, the heat-affected zone mechanical properties were higher than the base material values. While there was greater variation in the properties with heat input than was seen with the FZ

(see Figure 6.5), there was significant difference observed in the mechanical properties of the fibre welds as a function of heat input.

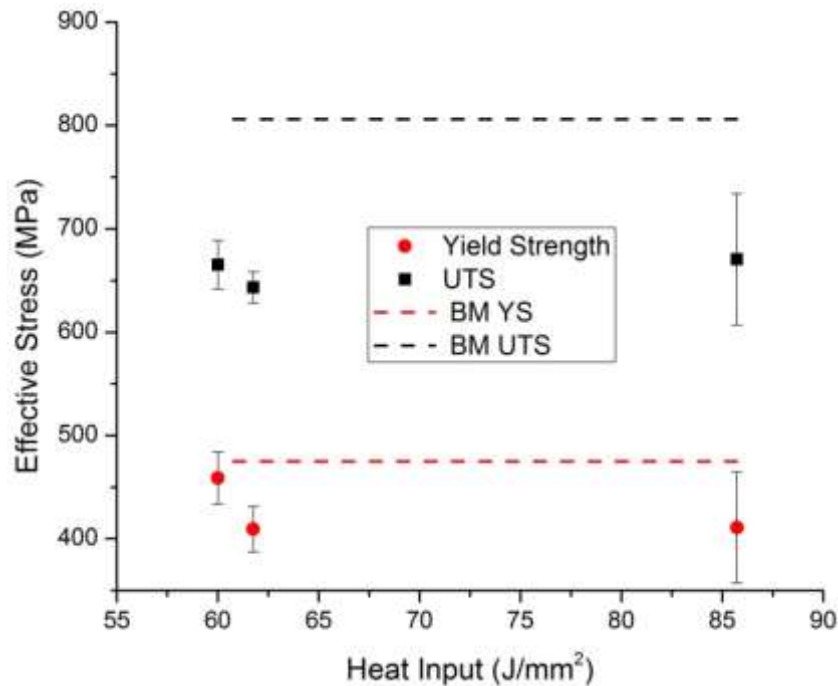


Figure 6.7: Stress versus heat input for the diode weld heat-affected zones.

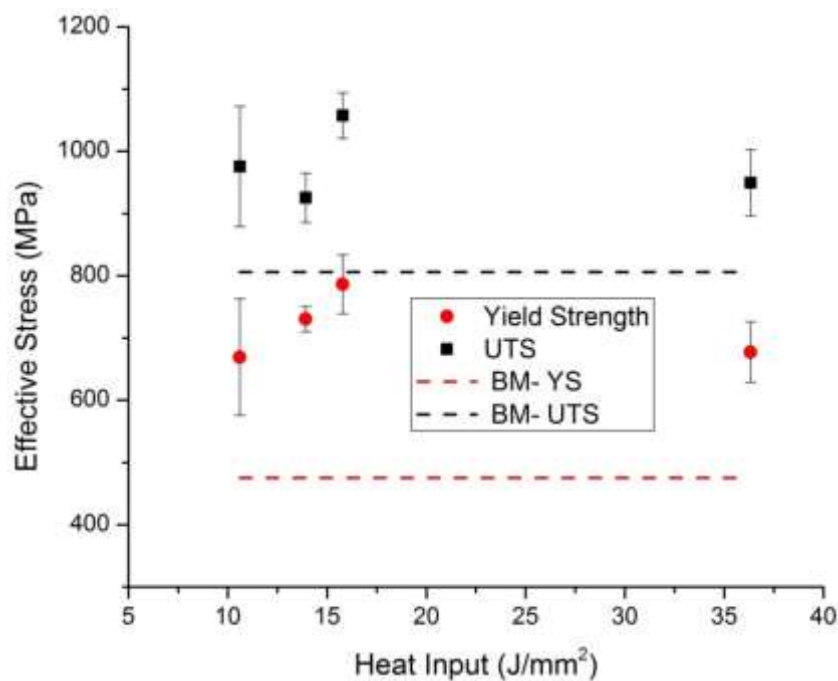


Figure 6.8: Stress versus heat input for fibre weld heat-affected zones.

To compare the mechanical properties of all experimental weld heat-affected zones, the UTS and yield strength for all welding cases were plotted with respect to heat input in Figure 6.9. It is seen that the behaviour of both mechanical properties is sigmoidal as a function of heat input, with good fit (adjusted $R^2=0.91$ and 0.98 for UTS and YS respectively). This behaviour can be attributed to the tempering of martensite within the HAZ of the weld which is the origin of the property changes within this zone. Martensite tempering was discussed in detail in section 2.3.2 and is a thermally activated process which has been shown in the literature to exhibit sigmoidal behaviour with tempering time (time constant or heat input in this case), whereby a certain amount of energy is required before the various stages of tempering can occur [1, 3, 4]. Waterschoot et al. [21] performed isothermal tempering of a DP steel and found a sigmoidal relationship between fraction of material transformed and tempering time which was fit to the JMAK equation. Similar results were seen in welded samples in the study of Biro et al. [4] where a phi parameter representing the fraction of martensite transformed was found to be related to tempering time (time constant) through the JMAK equation. Finally, Xia et al. [13] also observed sigmoidal behaviour between both the minimum hardness and HAZ softening and the time constant.

As the depression of mechanical properties is associated with the tempering of the martensite phase, this can explain the sigmoidal behaviour of the yield strength and UTS of the HAZ with respect to heat input. Higher

strengths were observed for the lower heat input welds as the martensite in the dual phase microstructure had not been fully tempered and the ferrite grain size has been (possibly) refined leading to higher strength than were seen in the BM. Once a critical heat input was reached, the martensite is able to fully temper in the HAZ resulting in a significant drop in both the UTS and yield strength. This is consistent with the behaviour seen in Figure 6.2, where the minimum hardness of the HAZ decreases with increasing time constant (heat input). While there was no significant differences observed in the optical micrographs of all experimental weld HAZ, this is due to the length scales available with optical microscopy and there was likely varying degrees of martensite tempering within the experimental weld heat-affected zones.

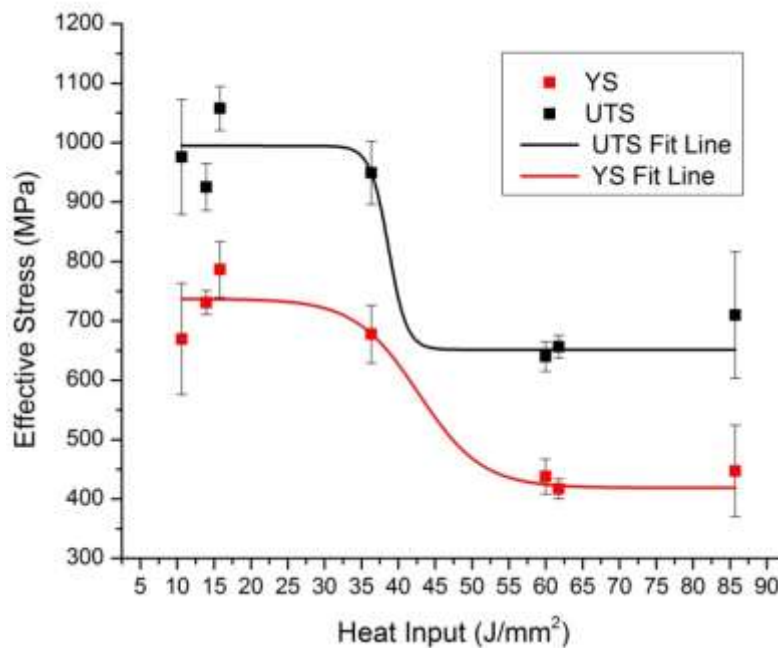


Figure 6.9: Stress versus heat input for all experimental weld heat-affected zones.

6.4 Weld Failure Localization

The across weld tensile testing results presented in section 5.3.2 showed that the fracture localization, when pulling the entire weld perpendicular to the tensile direction, was dependant on the welding conditions (see Figure 5.17 – Figure 5.19). To visualize the dependence of failure location on heat input, the best fit curve of the yield strength for all weld heat-affected zones is plotted versus heat input in Figure 6.10 and the failure locations noted. It can be seen that the 6 kW (F) 4 weld with a heat input of 10.6 J/mm² showed failure within the base material. Welds 4 kW (F) 4, 6 kW (F) 2 and 4 kW (F) 2 (heat inputs of 13.9, 15.8 and 36.3 J/mm² respectively) showed failure within the base material, near the border with the HAZ. Finally, the three diode welds, 4 kW (D) 0.8, 1.0 and 1.2 (heat inputs of 60.0, 61.8, and 85.7 J/mm² respectively) all failed in the HAZ. In all cases, the yield strength of the microstructural zone where failure occurred was lower than all other microstructural zones. While only the HAZ mechanical properties are shown, by comparing Figure 6.6 and Figure 6.9, it can be seen that for all welding conditions, the FZ yield strength was higher than that of the HAZ, thus the failure location would always be in either the BM or the HAZ and not the FZ. Based on this, one would expect that if the HAZ yield strength was higher than that of the BM failure would occur in the BM. From Figure 6.10, this would imply welds with heat inputs below approximately 45 J/mm² would fail in the base material, as was generally

observed. However, further testing would be required to find the exact transition heat input from HAZ to BM failure. In the case of the present study, welds with heat inputs below 36.3 J/mm^2 failed in the BM rather than the HAZ.

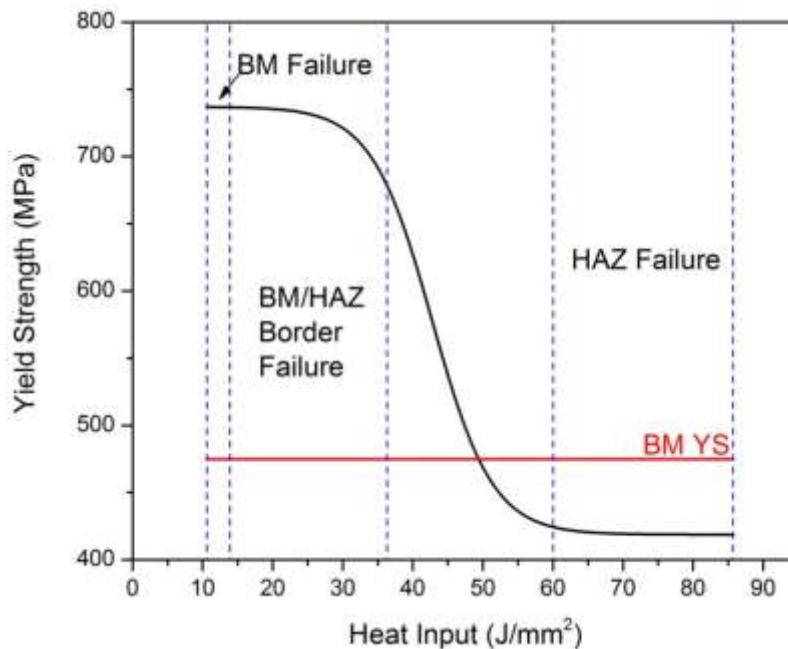


Figure 6.10: Yield strength versus heat input for all HAZ showing the failure location of across weld samples.

6.5 Summary

The heat input and time constant of all experimental welds were calculated using the methods described by Xia et al. [13] and discussed in CHAPTER 2 of this thesis. The HAZ hardness and the softening of the HAZ were plotted against both time constant and heat input and compared with the literature, with the general result that similar trends were observed in the current data as had been seen in the literature.

The mechanical properties (UTS and YS) of the FZ were plotted against the calculated heat input and a sigmoidal decay was observed with respect to heat input in both cases. This behaviour is attributed to the formation of untempered martensite within the low heat input weld fusion zones while both bainite and martensite were formed in the higher heat input weld fusion zones.

The mechanical properties (UTS and YS) of the HAZ showed a similar sigmoidal decay as the FZ properties with respect to heat input. This behaviour can be ascribed to the tempering of the martensite phase in the higher heat input welds resulting in lower mechanical properties. Conversely, the martensite in the lower heat input welds was not fully tempered which resulted in the higher mechanical properties observed in these cases versus the higher heat input welds.

Finally, the across weld testing of all experimental welds revealed that welds with a heat input below 36.3 J/mm^2 failed within the BM while welds with a heat input above 60.0 J/mm^2 failed within the HAZ when the tensile direction was perpendicular to the welding direction. Moreover, when the YS behaviour of the HAZ was plotted relative to the base material YS data, welds with the HAZ yield strength values below the BM values failed within the HAZ while, welds with HAZ yield strength values above the BM values fail within the BM. All of the above trends will be summarized in the following chapter.

CHAPTER 7 Conclusions and Future Work

7.1 Conclusions

A DP780 steel sheet laser welded using either a fibre or diode laser was examined in the present study. The microstructure, microhardness, macroscopic weld tensile performance, and individual weld zone mechanical properties were studied. From the present work the following conclusions were made:

1. Correlation between ASTM standard subsize samples and the specialized testing geometries of this study are very good and both returned comparable values for the UTS and YS in both base material and diode weld samples.
2. Welds with heat inputs greater than 60.0 J/mm^2 displayed yield strengths and UTS in both the fusion and heat-affected zones which were significantly depressed compared to the base material properties.
3. Welds with heat inputs of less than 36.3 J/mm^2 exhibited UTS and yield strengths for both the fusion and heat-affected zones which were significantly elevated compared to base material properties.
4. The yield strength and UTS of the weld fusion zones exhibited a sigmoidal decay behaviour with increasing heat input due to the presence of bainite observed with lower cooling rates in the fusion zone.

5. The UTS and yield strength of the weld heat affected zones exhibited a sigmoidal decay behaviour with increasing weld heat input due to the thermal activation of martensite tempering.
6. For welds made with a heat input greater than 60.0 J/mm^2 , tensile failure occurred in the heat-affected zone.
7. For welds made with a heat input less than 36.3 J/mm^2 , tensile failure occurred in the base material.

7.2 Future Work

Further work is required to fully understand the effects of laser welding on the mechanical properties of the individual microstructural zones of DP steels. Specifically as extensions of the present study, the following are suggested:

1. Perform a TEM study of one high and one low heat input weld to verify that the degree of tempering in each sample is what is expected.
2. Welds with heat inputs in the range of 35 J/mm^2 to 60 J/mm^2 should be made and tested to better understand the behaviour of the sigmoidal decay curves in this region.
3. Welds made in the same material but using different types of lasers should be made at overlapping heat inputs, to ensure that the sigmoidal decay behaviour of the mechanical properties observed is independent of laser type.

References

- [1] G. R. Speich, "Dual-Phase Steels," in *ASM Handbook Volume 1: Properties and Selection: Irons, Steels and High Performance Alloys*, vol. 1, 1990, pp. 424–429.
- [2] M. S. Rashid, "Dual Phase Steels," *Annu. Rev. Mater. Sci.*, vol. 11, no. 1, pp. 245–266, Aug. 1981.
- [3] R. G. Davies, "Influence of Martensite Composition and Content on the Properties of Dual Phase Steels," *Metall. Mater. Trans. A*, vol. 9A, pp. 671–679, 1978.
- [4] E. Biro, J. R. McDermid, J. D. Embury, and Y. Zhou, "Softening Kinetics in the Subcritical Heat-Affected Zone of Dual-Phase Steel Welds," *Metall. Mater. Trans. A*, vol. 41, no. 9, pp. 2348–2356, Jun. 2010.
- [5] E. Biro, S. Vignier, C. Kaczynski, J. R. McDermid, E. Lucas, J. D. Embury, and Y. N. Zhou, "Predicting Transient Softening in the Sub-Critical Heat-Affected Zone of Dual-Phase and Martensitic Steel Welds," *ISIJ Int.*, vol. 53, no. 1, pp. 110–118, 2013.
- [6] World Steel Association, "World Auto Steel," 2014. [Online]. Available: <http://www.worldautosteel.org/steel-basics/automotive-steel-definitions/>.
- [7] D. K. Matlock, J. G. Speer, E. De Moor, and P. J. Gibbs, "Recent Developments in Advanced High Strength Sheet Steels for Automotive Applications: An Overview," *Jestech*, vol. 15, no. 1, pp. 1–12, 2012.
- [8] K. N. Lankalapalli, J. F. Tu, and M. Gartner, "A model for estimating penetration depth of laser welding processes," *J. Phys. D. Appl. Phys.*, vol. 29, no. 7, pp. 1831–1841, Jul. 1996.
- [9] W. M. Steen and J. Mazumder, *Laser Material Processing*, 4th ed. New York, NY: Springer International Publishing, 2010.
- [10] B. S. Yilbas, S. Akhtar, and S. Z. Shuja, *Laser Forming and Welding Processes*. Heidelberg: Springer International Publishing, 2013.

- [11] A. De and T. Debroy, "Reliable Calculation of Heat and Fluid Flow during Conduction Mode Laser Welding through Optimization of Uncertain Parameters," *Weld. Res.*, no. July, p. 101s–112s, 2005.
- [12] C. A. Walsh, "LASER WELDING - Literature Review," *Mater. Sci. Metall. Dep. Univ. Cambridge*, 2002.
- [13] M. Xia, E. Biro, Z. Tian, and Y. N. Zhou, "Effects of Heat Input and Martensite on HAZ Softening in Laser," *ISIJ Int.*, vol. 48, no. 6, pp. 809–814, 2008.
- [14] M. F. Ashby and K. E. Easterling, "A First Report on Diagrams for Grain Growth in Welds," *Acta Mater.*, vol. 30, pp. 1969–1978, 1982.
- [15] J. C. Ion, K. E. Easterling, and M. F. Ashby, "A Second Report on Diagrams of Microstructure and Hardness for Heat-Affected Zones in Welds," *Acta Mater.*, vol. 32, no. 11, pp. 1949–1962, 1984.
- [16] G. Krauss, *Steels: Processing, Structure and Performance*. Materials Park: ASM International, 2005.
- [17] G. R. Speich and W. C. Leslie, "Tempering of Steel," *Materials Transactions*, 1972. [Online]. Available: http://download.springer.com/static/pdf/841/art%3A10.1007%2F02642436.pdf?auth66=1415307467_84f489ce9755ea86a32987f91e98f274&ext=.pdf. [Accessed: 06-Nov-2014].
- [18] R. Honeycombe and H. Bhadeshia, *Steels: Microstructure and Properties*, 2nd ed. Oxford, UK: Butterworth Heinemann, 2000.
- [19] G. R. Speich, "Tempering of Low-Carbon Martensite," *Trans. Metall. Soc. AIME*, vol. 245, pp. 2553–2564, 1969.
- [20] V. H. Baltazar Hernandez, S. S. Nayak, and Y. Zhou, "Tempering of Martensite in Dual-Phase Steels and Its Effects on Softening Behavior," *Metall. Mater. Trans. A*, vol. 42, no. 10, pp. 3115–3129, May 2011.
- [21] T. Waterschoot, K. Verbeken, and B. C. De Cooman, "Tempering Kinetics of the Martensitic Phase in DP Steel," *ISIJ Int.*, vol. 46, no. 1, pp. 138–146, 2006.
- [22] H. I. Aaronson, G. Spanos, and W. T. R. Jr, "A progress report on the definitions of bainite," vol. 47, pp. 139–144, 2002.

- [23] H. . Aaronson, G. . Purdy, D. . Malakhov, and W. . Reynolds, "Tests of the zener theory of the incomplete transformation phenomenon in Fe-C-Mo and related alloys," *Scr. Mater.*, vol. 44, no. 10, pp. 2425–2430, May 2001.
- [24] W. T. Reynolds, H. I. Aaronson, and G. Spanos, "A Summary of the Present Diffusionist Views on Bainite," *Mater. Trans.*, vol. 32, no. 8, pp. 737–746, 1991.
- [25] Z.-G. Yang and H.-S. Fang, "An overview on bainite formation in steels," *Curr. Opin. Solid State Mater. Sci.*, vol. 9, no. 6, pp. 277–286, Dec. 2005.
- [26] H. K. D. H. Bhadeshia and J. W. Christian, "Bainite in steels," *Metall. Trans. A*, vol. 21, no. 3, pp. 767–797, Mar. 1990.
- [27] H. K. D. H. Bhadeshia and D. V. Edmonds, "The mechanism of bainite formation in steels," *Acta Mater.*, vol. 28, pp. 1265–1273, 1980.
- [28] H. K. D. H. Bhadeshia, *Bainite in Steels*, Book No. 5. London: The Institute of Materials, 1992.
- [29] H. K. D. H. Bhadeshia and D. V. Edmonds, "The Bainite Transformation in a Silicon Steel," *Metall. Trans. A*, vol. 10A, no. July, pp. 895–907, 1979.
- [30] G. Spanos, H. S. Fang, and H. . Aaronson, "A Mechanism for the Formation of Lower Bainite," *Metall. Trans. A*, vol. 21A, no. June, pp. 1381–1390, 1990.
- [31] K. R. Kinsman, E. Eichen, and H. . Aaronson, "Thickening Kinetics of Proeutectoid Ferrite Plates in Fe-C Alloys," *Metall. Trans. A*, vol. 6A, no. February, pp. 303–317, 1975.
- [32] R. F. H. F. Hemann, K. R. Kinsman, and H. . Aaronson, "A Debate on the Bainite Reaction," *Metall. Trans.*, vol. 3, no. May, pp. 1077–1094, 1972.
- [33] G. . Purdy and M. Hillert, "Overview no. 38: On the nature of the bainite transformation in steels," *Acta Metall.*, vol. 32, no. 6, pp. 823–828, Jun. 1984.
- [34] M. Hillert, "Diffusion in Growth of Bainite," *Metall. Mater. Trans. A*, vol. 25A, no. September, pp. 1957–1966, 1994.
- [35] H. . Aaronson, T. Furuhashi, J. M. Rigsbee, W. T. Reynolds, and J. M. Howe, "Crystallographic and Mechanistic Aspects of Growth by Shear and

- by Diffusional Processes,” *Metall. Trans.*, vol. 21A, no. September, pp. 2369–2409, 1990.
- [36] B. Pan, K. Qian, H. Xie, and A. Asundi, “Two-dimensional digital image correlation for in-plane displacement and strain measurement: a review,” *Meas. Sci. Technol.*, vol. 20, pp. 1–17, Jun. 2009.
- [37] E. Biro, Manger-Product Characterization, ArcelorMittal Dofasco. Email. Hamilton, ON. February 1, 2013.
- [38] E. Biro, J. R. McDermid, S. Vignier, and Y. Norman Zhou, “Decoupling of the softening processes during rapid tempering of a martensitic steel,” *Mater. Sci. Eng. A*, vol. 615, pp. 395–404, Oct. 2014.
- [39] N. Farabi, D. L. Chen, J. Li, Y. Zhou, and S. J. Dong, “Microstructure and mechanical properties of laser welded DP600 steel joints,” *Mater. Sci. Eng. A*, vol. 527, no. 4–5, pp. 1215–1222, Feb. 2010.
- [40] N. Farabi, D. L. Chen, and Y. Zhou, “Microstructure and mechanical properties of laser welded dissimilar DP600/DP980 dual-phase steel joints,” *J. Alloys Compd.*, vol. 509, no. 3, pp. 982–989, Jan. 2011.
- [41] W. Xu, D. Westerbaan, S. S. Nayak, D. L. Chen, F. Goodwin, E. Biro, and Y. Zhou, “Microstructure and fatigue performance of single and multiple linear fiber laser welded DP980 dual-phase steel,” *Mater. Sci. Eng. A*, vol. 553, pp. 51–58, Sep. 2012.
- [42] D. Parkes, W. Xu, D. Westerbaan, S. S. Nayak, Y. Zhou, F. Goodwin, S. Bhole, and D. L. Chen, “Microstructure and fatigue properties of fiber laser welded dissimilar joints between high strength low alloy and dual-phase steels,” *Mater. Des.*, vol. 51, pp. 665–675, Oct. 2013.
- [43] W. Xu, D. Westerbaan, S. S. Nayak, D. L. Chen, F. Goodwin, and Y. Zhou, “Tensile and fatigue properties of fiber laser welded high strength low alloy and DP980 dual-phase steel joints,” *Mater. Des.*, vol. 43, pp. 373–383, Jan. 2013.
- [44] M. Xia, N. Sreenivasan, S. Lawson, Y. Zhou, and Z. Tian, “A Comparative Study of Formability of Diode Laser Welds in DP980 and HSLA Steels,” *J. Eng. Mater. Technol.*, vol. 129, no. 3, p. 446, 2007.

- [45] N. Sreenivasan, M. Xia, S. Lawson, and Y. Zhou, "Effect of Laser Welding on Formability of DP980 steel," *J. Eng. Mater. Technol.*, vol. 130, no. 4, p. 041004, 2008.
- [46] S. K. Panda, V. H. Baltazar Hernandez, M. L. Kuntz, and Y. Zhou, "Formability Analysis of Diode-Laser-Welded Tailored Blanks of Advanced High-Strength Steel Sheets," *Metall. Mater. Trans. A*, vol. 40, no. 8, pp. 1955–1967, Jun. 2009.
- [47] E. J. Mittemeijer, A. Van Gent, and P. J. Van der Schaaf, "Analysis of Transformation Kinetics by Nonisothermal Dilatometry," *Metall. Mater. Trans. A*, vol. 17A, no. August, pp. 1441–1445, 1986.
- [48] M. Avrami, "Kinetics of Phase Change. I General Theory," *J. Chem. Phys.*, vol. 7, no. 12, pp. 1103–1112, 1939.
- [49] M. Avrami, "Kinetics of Phase Change. II Transformation-Time Relations for Random Distribution of Nuclei," *J. Chem. Phys.*, vol. 8, no. 2, pp. 212–224, 1940.
- [50] M. Avrami, "Granulation, Phase Change, and Microstructure Kinetics of Phase Change. III," *J. Chem. Phys.*, vol. 9, no. 2, pp. 177–184, 1941.
- [51] L. Cheng, C. M. Brakman, B. M. Korevaar, and E. J. Mittemeijer, "The Tempering of Iron-Carbon Martensite; Dilatometric and Calorimetric Analysis," *Metall. Trans. A*, vol. 19A, no. October, pp. 2415–2426, 1988.
- [52] E. J. Mittemeijer, L. Cheng, P. J. van der Schaaf, C. M. Brakman, and B. M. Korevaar, "Analysis of Nonisothermal Transformation Kinetics; Tempering of Iron-Carbon and Iron-Nitrogen Martensites," *Metall. Trans. A*, vol. 19A, no. April, pp. 925–932, 1988.
- [53] M. Jung, S.-J. Lee, and Y.-K. Lee, "Microstructural and Dilatational Changes during Tempering and Tempering Kinetics in Martensitic Medium-Carbon Steel," *Metall. Mater. Trans. A*, vol. 40, no. 3, pp. 551–559, Jan. 2009.
- [54] M. Takahashi and H. K. D. H. Bhadeshia, "Model for transition from upper to lower bainite," *Mater. Sci. Technol.*, vol. 6, no. July, pp. 592–603, 1990.
- [55] J. H. Hollomon and L. D. Jaffe, "Time-temperature relations in tempering steel," *Trans AIME*, vol. 162, pp. 223–249, 1945.

- [56] D. Westerbaan, "Fiber Laser Welding of Advanced High Strength Steels by," 2013.
- [57] K. Bandyopadhyay, S. K. Panda, and P. Saha, "Prediction of formability of laser-welded dual-phase steel by finite element analysis," *Proc. Inst. Mech. Eng. Part B J. Eng. Manuf.*, vol. 228, no. 9, pp. 1048–1057, Sep. 2013.
- [58] E. Biro, S. S. Nayak, and Y. Zhou, "Changes in Mechanical Properties of Dual-Phase Steel Due to Post-Welded Microstructure and Loading Geometry," in *Trends in Welding Research, Proceedings of the 9th International Conference*, 2012, pp. 201–207.
- [59] S. K. Panda, N. Sreenivasan, M. L. Kuntz, and Y. Zhou, "Numerical Simulations and Experimental Results of Tensile Test Behavior of Laser Butt Welded DP980 Steels," *J. Eng. Mater. Technol.*, vol. 130, no. 4, p. 041003, 2008.
- [60] J. Kang, J. R. McDermid, and M. Bruhis, "Determination of the constitutive behaviour of AA6022-T4 aluminium alloy spot welds at large strains," *Mater. Sci. Eng. A*, vol. 567, pp. 95–100, Apr. 2013.
- [61] ASTM International, "Standard Test Method for Knoop and Vickers Hardness of Materials," *ASTM E384-11*, ASTM International, West Conshohocken, pp. 1–43, 2014.
- [62] ASTM International, "Standard Test Methods of Tension Testing of Metallic Materials," *ASTM E8/E8M - 13a*, West Conshohocken, 2013.
- [63] W. F. Hosford and R. M. Caddell, *Metal Forming: Mechanics and Metallurgy 3rd ed.* Cambridge, UK: Cambridge University Press, 2007.
- [64] R. H. Wagoner and J. L. Chenot, *Metal Forming Analysis*. Cambridge, UK: Cambridge University Press, 2001.

APPENDIX A Plane Strain Criteria

As mentioned in Chapter 4.4.1, according to Wagoner and Chenot [64], a sample can be considered to be in plane strain if $|\varepsilon_2/\varepsilon_1|$ is less than 0.2. $|\varepsilon_2/\varepsilon_1|$ was calculated at each time step for a given test and then an average over the entire test was calculated. It can be seen by the values in Table A.1, that all welding conditions both HAZ and FZ show $|\varepsilon_2/\varepsilon_1|$ values which are below the prescribed 0.2 indicating that all samples were in plane strain.

Table A.1: Plane strain criteria for mechanical testing samples.

Sample ID	Average $ \varepsilon_2/\varepsilon_1 $ for HAZ	Average $ \varepsilon_2/\varepsilon_1 $ for FZ
4 kW (D) 0.8	0.18	0.09
4 kW (D) 0.8	0.17	0.13
4 kW (D) 0.8	0.14	0.10
4 kW (F) 2	0.14	0.15
4 kW (F) 4	0.08	0.08
6 kW (F) 2	0.08	0.15
6 kW (F) 4	0.11	0.08

APPENDIX B Microstructure

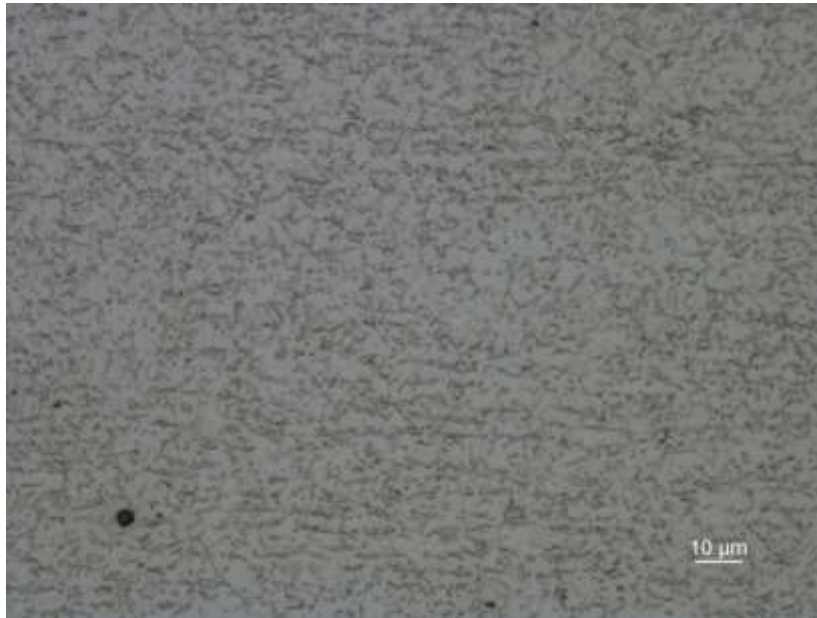


Figure B.1: 4 kW, 1.0 m/min diode weld HAZ microstructure

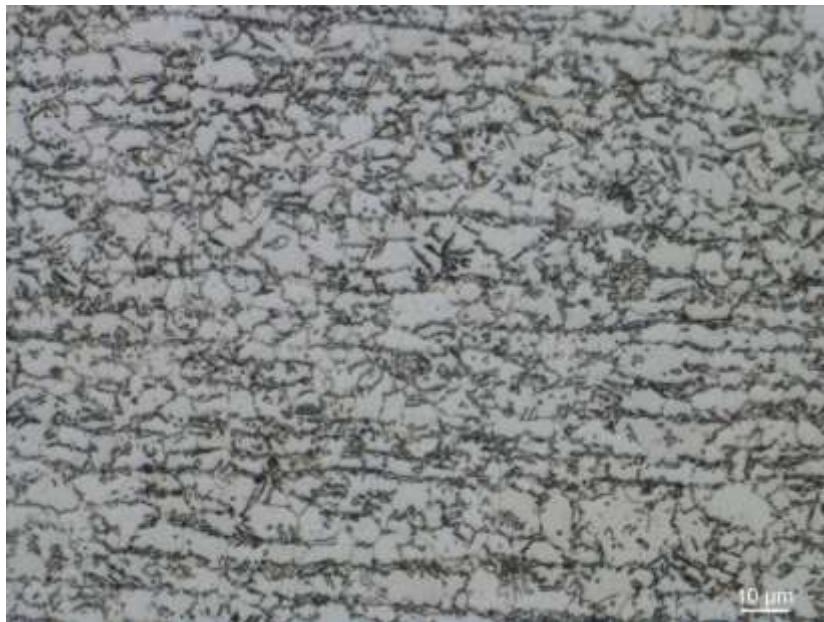


Figure B.2: 4 kW, 1.2 m/min diode weld HAZ microstructure.

APPENDIX C Strain Maps

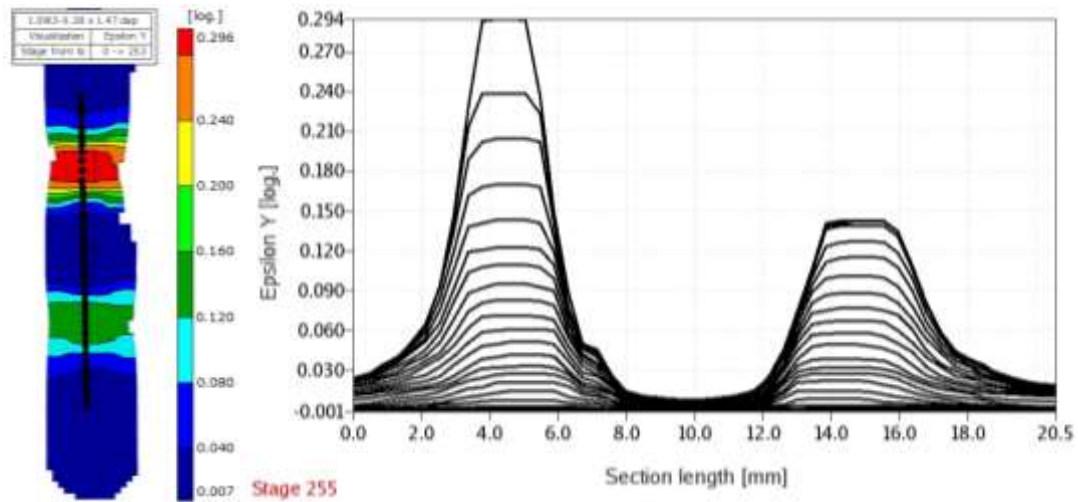


Figure C.1: Strain map and strain versus section length plot for 1.0 m/min diode weld.

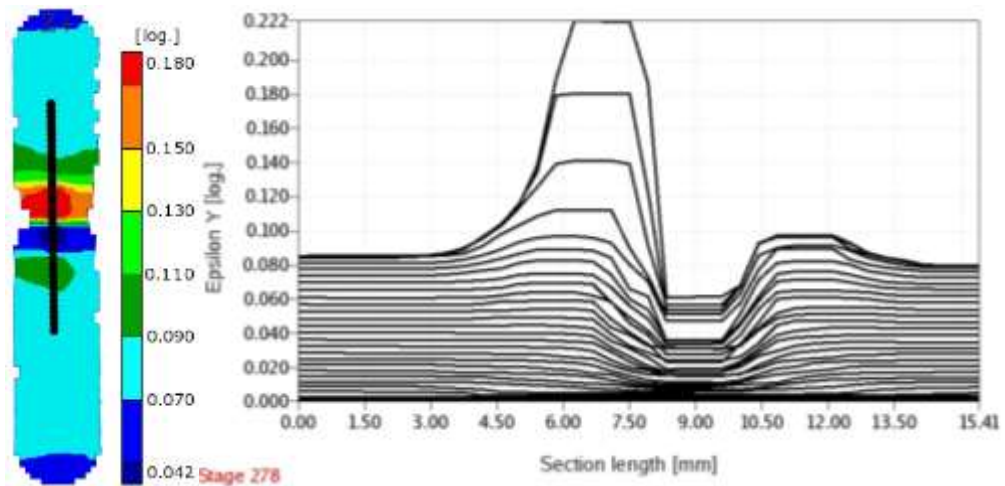


Figure C.2: Strain map and strain versus section length plot for a 4kW (F) 4 weld.

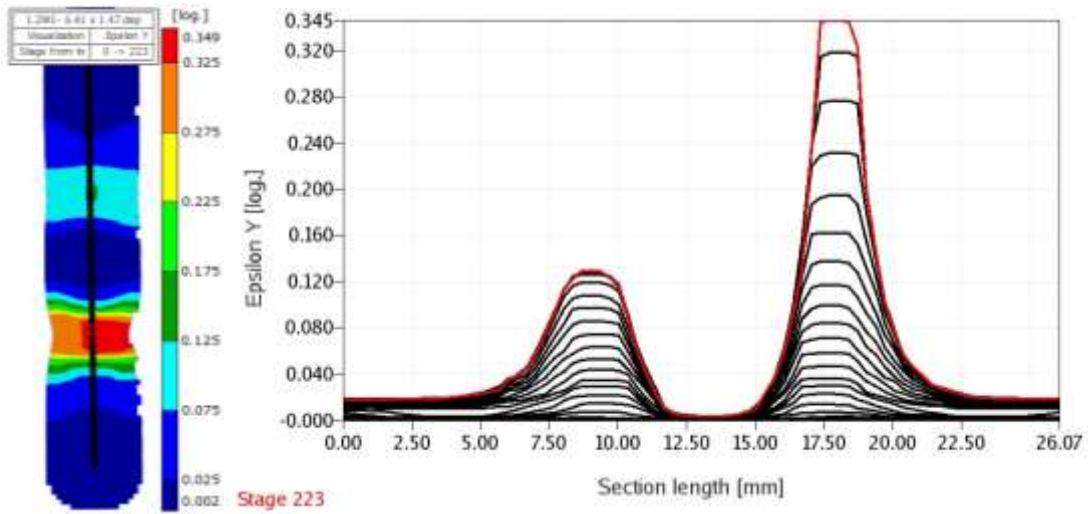


Figure C.3: Strain map and strain versus section length plot for 1.2 m/min diode weld.

APPENDIX D Heat Input Calculations

Table D.1: Materials properties used in Equation (1) and(2).

Material Property	Value
ρ (kg/m ³)	7860
c (J/kg/K)	680
T_{Ac1} (K)	9868
T_0 (K)	293
T_m (K)	1789.2
λ (W/m/K)	30

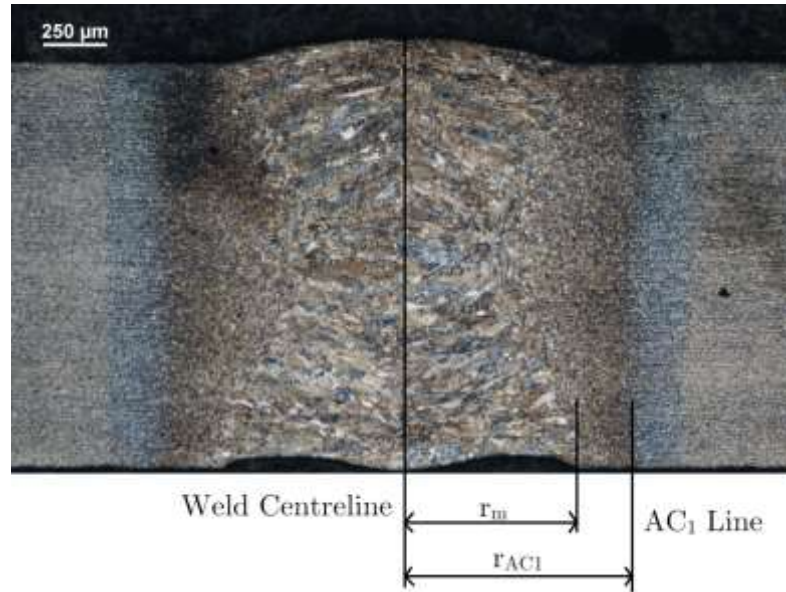


Figure D.1: Weld cross-section, showing the weld centreline, fusion zone boundary and AC1 isotherm.

$$\frac{Q_{net}}{vd} = \frac{\rho c (r_{Ac1} - r_m) (2\pi e)^{\frac{1}{2}}}{\left(\frac{1}{T_{Ac1} - T_0} - \frac{1}{T_m - T_0} \right)} \quad (1)$$

$$\tau = \frac{1}{4\pi e \lambda \rho c} \frac{[Q_{net} / (vd)]^2}{(T_{Ac1} - T_0)^2} \quad (2)$$

The values in Table D.1 were used in equations (1) and (2) along with the measured radii of isotherm positions from the weld cross-sections. These isotherm radii were measured four times and an average value was used in the heat input calculations (see Table D.2). The final calculated heat input and time constant values are given in Table 6.1.

Table D.2: Average HAZ and FZ radii measured from weld cross-sections.

Sample ID	Average r_m (mm)	Average r_{Ac1} (mm)
4 kW (D) 0.8	1.8	4.8
4 kW (D) 0.8	1.5	3.7
4 kW (D) 0.8	1.1	3.2
4 kW (F) 2	0.8	1.3
4 kW (F) 4	0.5	0.8
6 kW (F) 2	0.9	2.2
6 kW (F) 4	0.7	1.2